

Reduced Simulations of Scrape-Off-Layer Turbulence

Thomas Elliot Gruffydd Nicholas

PhD

University of York

Physics

March 2021

Abstract

This thesis looks at models of plasma transport in the Scrape-Off Layer (SOL) of magnetic fusion devices, which sets critical heat loads on the components in the divertor. The cross-field plasma transport in the SOL is due to filamentary turbulence, carrying particles and energy radially within the SOL. This thesis builds upon previous work using the STORM model, which concentrated on modelling individual filamentary structures. Here we simulate a saturated turbulent state, which is modelled using a system of drift-fluid equations, fed by localised density and energy sources. A review of the STORM model used is given, implemented in BOUT++, and a description of the upgraded analysis software written.

Comparisons are made between 3D simulations and reduced 2D simulations, which parameterize the parallel transport physics. We describe a simulation setup which aims to produce the closest possible comparison between the 2D STORM model and the 3D STORM model, run for plasma parameters representative of the MAST SOL in L-mode. We found that an interplay of issues caused by two reasonable-seeming assumptions in the model setup were the main reason for differences between the 2D and analogous 3D models. In very high collisionality conditions, the assumptions used to close 2D models are not valid, because high enough collisionality suppresses thermal conduction so that convection becomes important. We also found that a source localised above the X-point in the parallel direction for the 3D simulations causes supersonic flows beyond the X-point. Despite these differences, the 2D model successfully replicates the mean density profile and much of the higher-order statistics of the 3D models with matched sources and no parameter tuning.

After motivating the coupling of a core region to the SOL models, we adjusted our model by adding a core region inside the SOL region. We find that this causes considerable complications, as the spontaneous formation of large binormal mean flows exhibits strongly non-linear behaviour. We also examined the effect of altering perpendicular diffusion coefficients, and find that both viscosity and density diffusion matter a lot for the behaviour of these flows and for SOL profiles, even when only changed in the core.

Contents

Abstract	2
Contents	3
List of Tables	7
List of Figures	8
Acknowledgements	11
Declaration	12
1 Introduction	14
1.1 Demand for Clean Energy	14
1.2 Nuclear Fusion	14
1.2.1 Fuel choice	15
1.2.2 Relative Merits as an Energy Source	18
1.2.3 Criteria for Net Energy Gain	21
1.2.4 Different Confinement Methods	23
1.2.5 Single-particle Confinement	24
1.2.6 Tokamaks	25
1.3 Heat Exhaust	26
1.3.1 Power and Particle Balance	26
1.3.2 The Scrape-Off-Layer	27
1.3.3 The Exhaust Challenge	28
1.3.4 Implications for Reactor Design	29
1.3.5 Difficulties with divertor solutions: No Silver Bullets	31
1.4 Thesis Outline	36

2	Review of Scrape-Off-Layer Turbulence	37
2.1	Introduction	37
2.2	The Character of Radial Transport	37
2.2.1	Non-diffusivity	37
2.3	Experimental measurements	40
2.3.1	Langmuir Probes	40
2.3.2	Intermittent Fluctuations	42
2.3.3	Statistical Properties	43
2.3.4	Optical imaging diagnostics	44
2.3.5	Filaments	47
2.3.6	Practical Importance of Fluctuations	49
2.4	Theory and simulation	49
2.4.1	Transport vs turbulence codes	49
2.4.2	Complex physics	50
2.4.3	Single-filament modelling	50
2.4.4	Linear Stability of the SOL	56
2.4.5	Drift-turbulence modelling	58
2.4.6	Model complexity	58
2.5	Summary	59
3	Physical Model	61
3.1	Introduction	61
3.2	Braginskii Fluid Equations	61
3.3	Drift Reduction	67
3.3.1	Drift-ordering	68
3.3.2	Drift-fluid model	70
3.4	STORM Model	75
3.4.1	Approximations	75
3.4.2	Normalisation	81
3.4.3	Equations	82
3.5	Slab Geometry	85
3.6	Boundary Conditions	86
3.6.1	Location of domain boundaries	86
3.6.2	Sheath boundary conditions	86

3.6.3	Radial boundary conditions	87
3.7	2D STORM Model	88
3.7.1	2D STORM equations	89
3.7.2	Parallel closures	89
3.7.3	Parallel temperature regimes	92
4	Numerical Implementation	94
4.1	Introduction	94
4.2	BOUT++	94
4.2.1	Operator Representation	95
4.2.2	Physics Model	95
4.2.3	Numerical Flexibility	97
4.2.4	Possible Geometries	98
4.3	STORM	99
4.3.1	Time Solver	99
4.3.2	Laplace Solver	99
4.3.3	Staggered Grids	100
4.3.4	Evolving Logarithms	100
4.3.5	Boundary Conditions	101
4.4	Analysis and post-processing tools	101
5	Comparison of 2D and 3D SOL-only models	103
5.1	Introduction	103
5.2	Motivation	103
5.3	Setup and Domain Geometry	104
5.4	Results and discussion	107
5.4.1	Comparison between 2D and 3D	107
5.4.2	Varying divertor leg length	114
5.4.3	Sensitivity to parameters in 2D	117
5.5	Conclusions	120
6	Including a Core Region in 2D models	124
6.1	Introduction	124
6.2	Motivation of Coupled Core-SOL Modelling	124
6.3	Setup and Domain Geometry	125

6.4	Problem of Unphysical Flow Generation	127
6.5	Alterations not affecting mean flows	129
6.5.1	Boundary Conditions	129
6.5.2	Loss Terms	129
6.5.3	Relaxing the Boussinesq approximation	130
6.6	Effect of dissipation coefficients	131
6.6.1	Onset at low dissipation	132
6.6.2	Variation of profiles	133
6.6.3	“Bursting Convection” Regime	134
6.7	Possible Solutions	137
6.7.1	Stay Above Threshold	137
6.7.2	Hasegawa-Wakatani Term	138
6.8	Similarity to 2D Rayleigh-Bénard System	141
6.9	Conclusions	143
7	Conclusions and Future Work	144
7.1	Conclusions	144
7.2	Future Work	146
A	Scan in Grid Resolution	148
	References	152

List of Tables

1	Various candidate fusion reactions	16
2	Various likely advantages and disadvantages of fusion as an energy source . .	22
3	Reference normalisation values	104
4	Normalised dissipation coefficients	104

List of Figures

1	Binding energy of atomic nuclei per nucleon	15
2	Reaction cross-sections for a range of fusion reactions	17
3	Guiding-centre drift of a charged particle	25
4	Schematic diagram of a stellarator	26
5	Schematic diagram of a tokamak	27
6	Schematic of a diverted tokamak	28
7	Double null geometry vs a single null	32
8	Schematic of target field line tilting	33
9	Schematic of flux expansion	34
10	Volumetric radiation at the target	35
11	Effective cross-field diffusivities in C-Mod	39
12	Flux vs density scale length in TCV	40
13	Langmuir Probe Diagnostic on DIII-D	41
14	Fluctuating timeseries in the SOL	42
15	Universality of fluctuation statistics	43
16	Increasing intermittency with radial position	45
17	Universality of power spectra	46
18	Gas puff images of blobs in NSTX	47
19	Wide-angle fast camera imaging on MAST	48
20	Diamagnetic current in an idealised filament	51
21	Current paths within a filament	52
22	Dipolar electrostatic potential within a filament	53
23	Observed blob velocity scalings in experiments	54
24	Slab model of the scrape-off-layer	85
25	Example warped BOUT++ simulation grid	98

26	Schematic diagram of simplified SOL-only geometry	106
27	Snapshot of typical turbulence in the drift-plane.	107
28	Average radial profiles of density moments	108
29	Average radial profiles of electron temperature	109
30	Fluctuation probability distribution functions.	110
31	Power spectrum of density fluctuations	111
32	Average radial profiles of collisionality	112
33	Average radial profiles of parallel heat flux in 2D	113
34	Average radial profiles of parallel heat flux in 3D	114
35	Parallel density profiles for different leg lengths in the near SOL	115
36	Parallel density profiles for different leg lengths in the far SOL	116
37	Parallel temperature profiles for different leg lengths in the near SOL	117
38	Parallel density profiles for different leg lengths in the far SOL	118
39	Parallel profiles of mach number in the near SOL	119
40	Parallel profiles of mach number in the far SOL	120
41	Effect of parallel losses on the temperature profiles	121
42	Effect of density source on the density profiles	122
43	Effect of energy source on the temperature profiles	122
44	Effect of energy source on the density profiles	123
45	Schematic diagram of simplified coupled core-SOL geometry	126
46	Example of unphysical drop in core potential in a 2D model	127
47	Example of unphysical drop in core potential over time	128
48	Example of unphysically-large shear in core flow in a 2D model	129
49	Core potential profile for different inner radial boundary conditions	130
50	Binormal mean flow as a function of viscosity	132
51	Binormal mean flow as a function of density diffusion	133
52	Mean core-SOL density profiles as a function of core diffusion	134
53	Mean core-SOL temperature profiles as a function of core diffusion	135
54	Mean core-SOL density profiles as a function of core viscosity	136
55	Mean core-SOL temperature profiles as a function of core viscosity	137
56	Lifecycle of an intermittent burst of transport from the core	138
57	Evolution of the kinetic energy in radial vs binormal flows in the bursting regime	139
58	Binormal mean flow over time with a drift-wave term included	140

59	Snapshot of 2D core potential with drift-wave term included	141
60	Density profiles for various perpendicular resolutions	148
61	Power spectra for various perpendicular resolutions	149

Acknowledgements

Despite the authorship, a thesis is far from a solo endeavour. Professionally I would first like to thank all the members of the STORM group. In particular Sarah Newton and John Omotani have both been beyond generous with their time and advice, which I, and I think anyone else who has ever asked them a question, greatly appreciate. Fabio Riva has been a font of knowledge and computational black magic, and patiently put up with all my silly questions and errors. Fulvio Militello is an admirable scientist, whose supervision I feel has set an example of how to approach thorny scientific questions without losing track of the bigger picture. Ben Dudson is a quiet oracle, who has also indulged me in distracting side-projects which have turned out to be personally very valuable. The York Plasma Institute and the Fusion CDT are both wonderful, welcoming, and impressive institutions, and an exemplar of how to run a PhD program.

Personally I would like to thank all the other students on the CDT, at the YPI, at CCFE, and those who I met at GA, in particular any of them who I've ever shared a hot tub with. Omkar deserves special mention both for endless discussions of the SOL and also for being the world's most relaxed housemate. Thanks to Mission Burrito on St Michael's St., whose rice boxes fuelled much of my PhD. Finally I would like to thank my parents, who have unfailingly supported my interest in science since a young age, and provided basically everything else that matters.

Declaration

I declare that: this thesis is a presentation of original work; I am the sole author; this work has not previously been presented for an award at this or any other university; all sources are acknowledged as references.

Aspects of this work have previously been presented in the following publications:

- Chapter 1 contains material from the publication Nicholas et al., “Re-examining the role of nuclear fusion in a renewables-dominated energy mix”, *Energy Policy*, **149**, June 2020 (2021).[1]
- Chapter 5 is based on work in Nicholas et al., “Comparing Two- and Three-Dimensional Models of Scrape-Off-Layer Turbulent Transport”, submitted to *Plasma Physics and Controlled Fusion*, accessible on ArXiv[2].

Other aspects of this work have partly enabled or are otherwise closely related to work in the following publications:

- The software development described in section 4.4 was employed in the jointly-authored publication Decristoforo et al., “Blob interactions in 2D scrape-off layer simulations”, *Physics of Plasmas*, **27**, 122301 (2020) [3].
- The solution suggested in Chapter 6 was subsequently employed in the jointly-authored paper Decristoforo et al., “Numerical turbulence simulations of intermittent fluctuations in the scrape-off layer of magnetized plasmas”, submitted to *Physics of Plasma*, accessible on arXiv [4].

Other jointly-published work not directly related to the contents presented in this thesis:

- The jointly-authored publication Walkden et al., “3D simulations of turbulent mixing in a simplified slab-divertor geometry”, *Nuclear Materials and Energy*, **18**, (2019) [5],

- The jointly-authored publication Hoare et al., “Dynamics of scrape-off layer filaments in high β plasmas”, *Plasma Physics and Controlled Fusion*, **61**, (2019) [6].

Chapter 1

Introduction

Material in this chapter was published as part of the jointly-authored paper “*Re-examining the role of nuclear fusion in a renewables-based energy mix*”, Nicholas et. al., Energy Policy, Vol. 149, 2021[1]

1.1 Demand for Clean Energy

Historically, there is an empirical link between energy use and development, meaning that as countries in the Global South develop further, we expect global primary energy use to rise[7]. Theoretical studies have shown that humanities’ basic welfare needs could be met with a minimum global final energy use 60% lower than 1960’s levels[8], but even if that scenario were realised as a steady-state then primary energy infrastructure will have to be maintained and replaced indefinitely.

Either way, global society will require many TeraWatts of energy supply to maintain living standards, and given the clear requirement to limit greenhouse gas emissions to meet sustainable development goals[9], the primary energy supply technologies used must be low-carbon.

1.2 Nuclear Fusion

One possible source of low-carbon energy is nuclear fusion. In the IPCC’s 1.5 scenario nuclear fission power plants contributes up to around 19% of global electricity generation by 2040[9], and nuclear fusion offers multiple advantages over fission technologies (explored in section 1.2.2).

The obverse of nuclear fission is fusion, in which elements with lighter nuclei combine to create a larger atomic nucleus. A fusion reaction usually still releases energy - because it

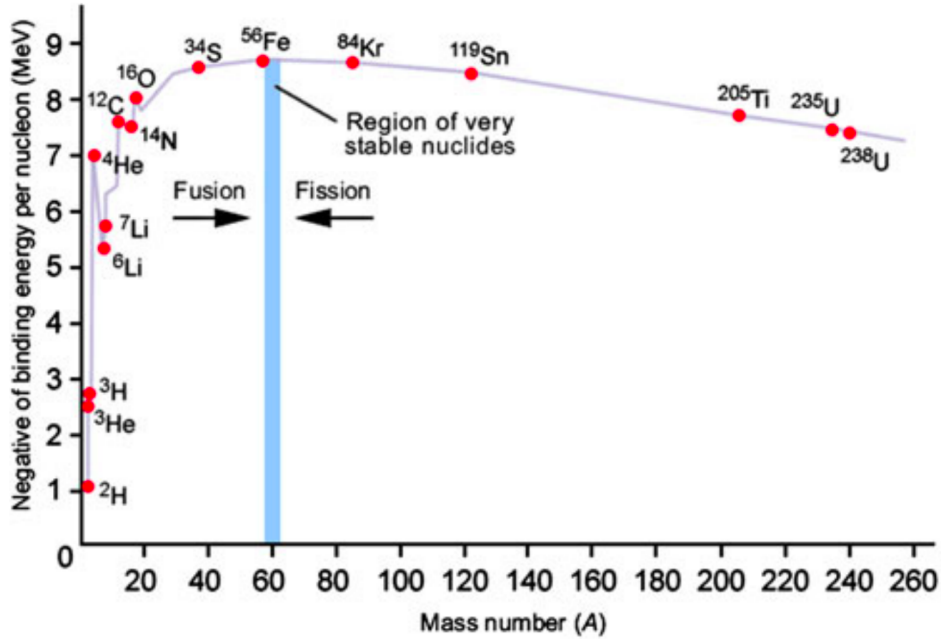


Figure 1: Binding energy of atomic nuclei per nucleon. Reactions which decrease their binding energy will release energy, so either fusion or fission reactions can be exothermic. Diagram taken from [10].

increases the binding energy per nucleon (as shown in figure 1).

1.2.1 Fuel choice

Although a multitude of nuclear reactions occur inside stars, allowing many different routes to overall energy production, candidate reactions for terrestrial fusion energy production are severely constrained. To be possibly useful as an energy source, a reaction must be:

- Exothermic: The products must have more kinetic energy than the reactants.
- Single step: As stars have the luxury of gravity providing confinement times on the order of thousands of years, they can use multi-step processes such as the CNO cycle, where intermediate states have long lifetimes. For example the $^{13}_7\text{N}$ intermediate state in the CNO-I cycle has a half-life of 9.965 minutes[11].) Terrestrial reactors must use single-step exothermic reactions, or else they would need to successfully confine the same particles for at least the decay time of the intermediates before generating any significant power.
- Two-body: Three-body collisions are extremely unlikely in anything but stellar environments, so reactions must involve only two reactants.

- Multi-nucleon producing: To have a significant chance of occurring the reaction must produce two or more products, as then energy and momentum can be conserved without producing a photon, which would require mediation by the electromagnetic force, which would mean a small cross-section.
- Nucleon-conserving: The number of protons and neutrons must be conserved, as any reaction which does not conserve them involves the weak interaction, and therefore has a small cross-section.
- Low-Z: As the nuclei's electrostatic repulsion must be overcome, then the reactants must have low atomic number Z.

This leaves only a small subset of reactions, the main candidates of which are listed in table 1.

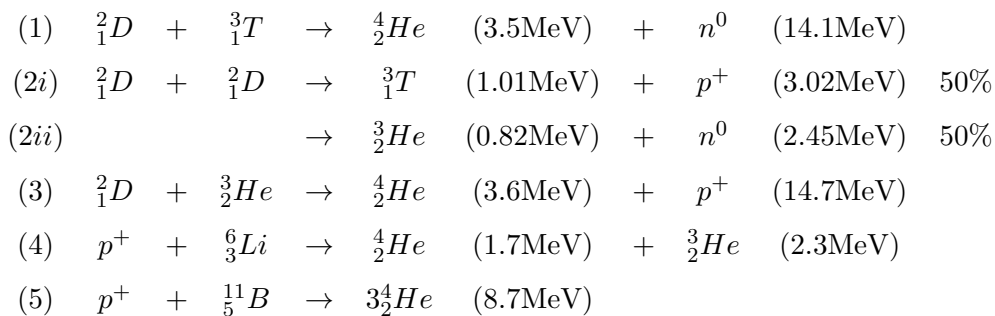


Table 1: Various candidate fusion reactions, and the binding energy released for each.[12]

Almost all the reactions form 4_2He as a product, because of its very tight nuclear binding. We can also see that $D-T$ and $D-{}^3He$ yield almost 10MeV more than any of the other reactions. However, even after satisfying these constraints, the electrostatic repulsion between nuclei is so strong that the effective reaction cross-sections are negligible for colliding particles with relative incident energies of below around 10keV (as shown in figure 2).

Furthermore stars are so massive that even a relatively low power density can add up to massive overall power, so reactions with relatively low cross-sections can be important. In contrast the losses due to the imperfect nature of magnetic confinement (or the transient nature of inertial confinement) mean that fusion reactors must have extremely high power densities, and so employ processes with large reaction cross-sections.

Given that Tritium is not a naturally-occurring isotope, and the production of high-energy neutrons requires reactor materials be resistant to neutron irradiation damage, the possibility of utilising aneutronic fuels such as $p - {}^{11}B$ is enticing. Unfortunately, Rider[13] shows that

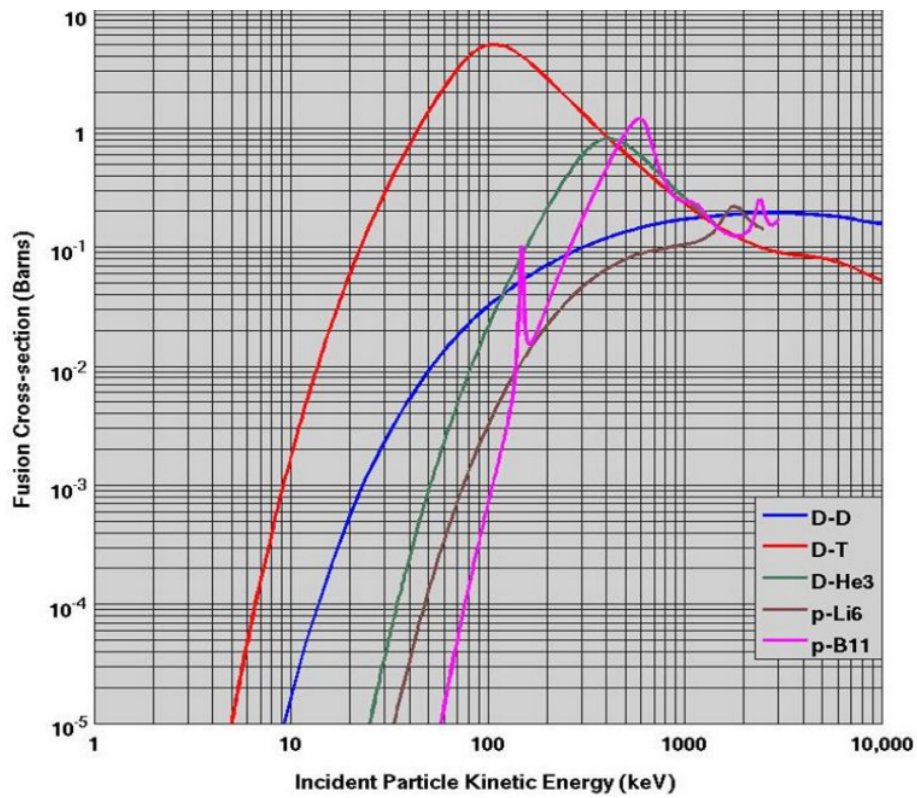


Figure 2: Reaction cross-sections for a range of fusion reactions. D-T not only has by far the largest maximum cross-section, but its maximum occurs at the lowest incident particle energy. Diagram taken from [12].

even if the required temperatures of $\approx 300\text{keV}$ could be achieved, an aneutronic plasma would be unlikely to be a net source of energy.

When charged particles are accelerated, they emit electromagnetic radiation, which carries away some of their energy. This is normally seen in the context of linear acceleration (such as in antennas), but can occur if the particle undergoes a large enough transverse acceleration too. The magnitude of acceleration required for this loss to become significant is so large that it is only normally relevant in circular particle accelerators. However, in an extremely hot plasma, the radial Coulomb force exerted during a close encounter between an electron and an ion can cause significant radiation emission, in an effect known as *bremstrahlung*, German for “braking radiation”.

For $10 - 20\text{keV}$ $D-T$ plasmas *bremstrahlung* is normally only a small source of loss, but rises rapidly to become the dominant consideration in the power balance at very high temperatures. Rider[13] finds that, in a $p\text{-}^{11}\text{B}$ plasma with its electrons and ions at rough thermal equilibrium, and $T_i \approx 300\text{keV}$, the power lost to *bremstrahlung* would be 70% larger than the fusion power generated. For $p\text{-}^6\text{Li}$ with $T_i \approx 800\text{keV}$ the power lost to *bremstrahlung* is nearly 5 times larger than the fusion power. More recent re-analysis with an updated value for the $p\text{-}^{11}\text{B}$ reaction cross-section is more favourable[14], but overall this still indicates that high-temperature aneutronic fuels likely cannot be used for net energy production.

All remaining fuel choices produce high-energy neutrons, and the $D-T$ reaction has both the largest fusion cross-section, and its maximum cross-section occurs at the lowest temperature. These high-energy neutrons present considerable challenges for reactor design, and affect the overall characteristics of any future fusion power plant.

1.2.2 Relative Merits as an Energy Source

A fusion power plant based on a D-T scheme has multiple desirable features, effectively retaining almost all of the positive characteristics of a fission power plant whilst mitigating some of the disadvantages.

Nuclear processes do not release CO_2 or other greenhouse gases, nor create particulate air pollution. Even after accounting for the emissions currently created during manufacture, decommissioning and fuel procurement, the CO_2 -equivalent emissions per kWh of existing nuclear power is orders of magnitude lower than that of fossil fuel plants[15], and preliminary estimates for fusion plants are similarly low[16]. Like other “low-carbon” technologies, eventually these emissions can be decreased to zero by decarbonizing the construction, mining, and industrial processes involved in the rest of the supply chain.

The key advantage over wind and solar generation is the ability to generate power on-demand outside of daylight hours and regardless of local wind conditions, making fusion a form of so-called *firm* power generation, which can be *dispatched* as required. Whilst intermittent renewables are projected to provide the lion’s share of low-carbon electricity, the energy modelling literature suggests that as penetration of intermittent wind and solar increase, dispatchable sources become more valuable. Whilst storage technologies help mitigate this problem, they do not eliminate it. Therefore, overall system costs can be lowered significantly by including some firm dispatchable generation[17, 18], meaning that diversified energy mixes which include non-renewable backup are almost always cheaper overall. Therefore whilst some studies argue that a 100% renewables energy system is technically possible[19, 20], in any cost-optimal scenario firm sources will play a crucial role.

Nuclear plants produce a lot of power per square kilometer relative to wind or solar, minimising the impact of land use change on biodiversity. The neutron-producing core of a fusion plant is actually much less energy dense than a fission plant’s core¹, but the spatial footprint of either is dominated by balance-of-plant and associated site infrastructure.

Deuterium is plentiful: it has a natural abundance of about 1 in 6420 hydrogen atoms in the ocean, meaning the total reserves represent global energy supply for billions of years. The other main input to a D-T fuel cycle, Lithium, is considerably more scarce. Using the approach of Fasel[21] but with updated Lithium availability estimates[22] gives currently-accessible terrestrial resources of terrestrial lithium as capable of providing 2800 years of global fusion power. This timescale is an order of magnitude larger than the 100 years estimated for using Uranium once-through in light-water fission reactors, but comparable to using known conventional uranium resources in potential generation IV fission reactors[23]. Lithium is also present in seawater, but at much lower concentrations than deuterium. It has been estimated that the energy return ratio (EROI) on Lithium extraction from seawater for D-T fusion would be barely above 1[24].

Relative to fission, fusion leaves a reduced radioactive waste burden. The fusion community originally aimed for all materials involved to meet the criterion of only being classed as low-level waste (LLW)[25], motivated by LLW legally requiring only surface disposal, not deep geologic disposal[26]. This was enshrined in the “reduced-activation criterion”, which was defined as[27]:

“The materials selection for fusion energy’s nuclear waste production, after an

¹ $\sim 1.2\text{MW}/\text{m}^3$ for EU-DEMO1 vs $\sim 300\text{MW}/\text{m}^3$ for a Sodium-Cooled Fast Reactor

initial ~ 100 years removal from the reactor, can be disposed of in low-level waste repositories.”

Whilst the fusion reaction itself does not produce radioactive by-products, the neutron output power will inevitably partly be incident on the reactor’s first wall and structural materials. For this purpose so-called low-activation steels were designed, of which EUROFER97 is the leading candidate[28], and was chosen as the neutron-facing structural material in the EU-DEMO1 design[29]. Whilst early studies predicted that these steels would meet the LLW criterion[27, 30], more recent research[31–33] instead suggests that trace impurities in the steels will cause them to exceed the activation limit and be classed as ILW². It may however be possible to avoid this classification by relaxing the criteria for ILW. Regardless, the lack of high-level waste is still an advantage relative to fission - HLW requires initial active cooling, and the ILW produced by fusion should not contain radioisotopes with half-lives > 100000 years.

Fusion does have a clear advantage over fission in terms of avoiding proliferation of nuclear weapons. Tritium is used in thermonuclear weapons but is of little use alone because fissionable material is required in the primary stage. 14.1MeV fusion neutrons can be used to generate fissionable material, but this is hard to do in a clandestine manner[34].

The other advantage of fusion over fission is the absence of meltdown risk. As a nuclear site with a radioactive inventory, a fusion power plant shares some possible accident scenarios regarding accidental leaks of radioactive material, but the worst possible cases where a meltdown leads to sustained and uncontrolled release are excluded.

Fusion power plants would still have some disadvantages compared to other sources. As described above, significant volumes[35, 36] of nuclear waste are likely unavoidable, and if these are classified as intermediate-level waste they will require geological disposal. The complexity, size, and regulatory requirements of a fusion power plant will likely mean that the monetary cost per kWh is comparable to that of existing fission plants, so it will not compete directly with cheap intermittent renewable generation. Steady-state designs would likely require a high recirculating power fraction, driving down overall plant efficiency[37]. These characteristics likely mean that any future fusion power plants would be competing instead with other firm low-carbon sources, including fission, possibly gas with carbon capture and storage, and geothermal[38].

²The implications of the production of Intermediate-Level Waste when comparing fusion’s advantages and disadvantages to other energy generation technologies have been explored in Nicholas et al. (2020)[1]

As an aside, whilst fusion and fission are normally considered as different technologies, there are arguments for building a fission-fusion hybrid reactor, which utilises fissionable material in the blanket of a fusion device[39].

Some of these various advantages and disadvantages are summarized in figure 2, which is adapted from [1], where a more comprehensive discussion can be found.

1.2.3 Criteria for Net Energy Gain

No scheme designed to confine the reacting fusion ions will perfectly confine their energy. Instead that energy will slowly escape from the region of confinement, with a characteristic timescale given by the energy confinement time τ_E , defined as

$$\tau_E = \frac{W}{P_{\text{loss}}}, \quad (1.1)$$

where W is the energy density, and P_{loss} is the power lost per unit volume. As no present-day machine yet produces significant fusion power in steady state, they have $P_{\text{loss}} = P_{\text{aux}}$, meaning that τ_E is an easily-measurable quantity.

For a steady state reaction the plasma must have a constant temperature T , and for a plasma consisting of a 50:50 mix of D-T, the thermal energy density of both ions and electrons together is

$$W = 3nk_B T. \quad (1.2)$$

The number of fusion reactions per unit time per unit volume f is given by

$$f = n_D n_T \langle \sigma v \rangle = \frac{1}{4} n^2 \langle \sigma v \rangle, \quad (1.3)$$

where σ is the fusion collision cross section from figure 2, v is the relative velocity of the colliding ions, and $\langle \rangle$ denotes averaging over all velocities in a Maxwellian velocity distribution of temperature T , and their combination $\langle \sigma v \rangle$ is the rate coefficient of the reaction.

In order for the fusion power to exceed the rate of energy loss (and therefore meet the so-called Lawson criterion) then

$$f E_{\text{ch}} \geq P_{\text{loss}}, \quad (1.4)$$

where E_{ch} is the energy of the charged products. (The uncharged products will not remain confined by the magnetic field for long enough to redeposit their energy back into the plasma. Substituting in (1.1), (1.2) and (1.3) gives

$$\frac{1}{4} n^2 \langle \sigma v \rangle E_{\text{ch}} \geq \frac{3nk_B T}{\tau_E}, \quad (1.5)$$

	Intermittent Renewables (wind + solar)	Gas + CCS	Geothermal	Fission (e.g. PWR)	Gen IV Fission (e.g. Sodium-cooled fast reactor)	Fusion	Fission-Fusion Hybrid
LCOE	cheap (excluding energy storage)	medium	medium	expensive	expensive	expensive	expensive (but < fusion)
Long-term waste	no nuclear	CO ₂ storage	no nuclear	high-level nuclear	high-level nuclear (but spent nuclear fuel < fission)	likely intermediate-level nuclear	high-level nuclear
Nuclear safety risk	no nuclear risk	no nuclear risk	no nuclear risk	melt-down risk	melt-down risk, but passively-contained	risk of nuclear accident, but not melt-down	risk of nuclear accident, but not melt-down
Weapons proliferation risk (fissile material on site)	no	no	no	yes	yes	no (but tritium produced)	yes
Resource constraints	rare-earth metals (depends on substitutability)	gas reserves	low	Uranium-235	Can use Uranium-238	Lithium, but possibly Beryllium	Can use Uranium-238
Scalability	require intermittency solutions at high penetrations	limited by CO ₂ storage locations	low, but depends on technology	high	high	high	high
Areal energy density	low	high	high on surface	high	high	high	high
Load-following	no	fast	medium	rate-limited by thermal inertia	rate-limited by thermal inertia	rate-limited by thermal inertia	rate-limited by thermal inertia
Heat production	no	T limited by technology	yes	yes	yes	yes	
Burn actinide waste?	no	no	no	yes	yes	yes	
EROI	~ 50 (wind without storage) ~ 20 (solar without storage)	~ 40	~ 7 (from [40])	~ 85	≤ ~ 170	≤ ~ 170	≤ ~ 170
Technology readiness level (TRL)	9	8	9, (6 for enhanced geothermal)	9	8/9	2/3	3/4

Table 2: Various likely advantages and disadvantages of fusion relative to other energy sources. Adapted from [1].

which can be rearranged to get

$$n\tau_E \geq L \equiv \frac{12k_B T}{E_{\text{ch}} \langle \sigma v \rangle}. \quad (1.6)$$

For D-T fuel the product $T/\langle \sigma v \rangle$ has a minimum around $T = 26\text{keV}$ (note this is different to the the peak of the collision cross-section in figure 2). Therefore, to generate net energy, a fusion reactor operating at the optimum average temperature of $\sim 26\text{keV}$ must also maintain n and τ_E at values high enough such that their product exceeds L . A fusion reactor operating at a slightly lower temperature will need to compensate such that the so-called ‘‘triple product’’ $nT\tau_E$ is large enough.

1.2.4 Different Confinement Methods

The prototypical fusion reactor is a star, such as the Sun. Whilst stellar cores have very high densities ($\sim 100\text{gcm}^{-3}$ in the Sun), they have surprisingly low power densities (only about 0.2kWm^{-3} in the Sun - about the same as a pile of compost). This is because the protium-dominated environment (and comparatively low reaction rate) only allows fusion to proceed through relatively inefficient reaction chains - primarily the proton-proton chain in the Sun. However the energy confinement time of a star is huge - the diffusion timescale for a photon to escape from the core to the surface of the Sun is $\sim 1.7 \times 10^5$ years[41]. This is a consequence of their enormous size, and obviously does not represent a viable pathway towards terrestrial fusion.

Terrestrial fusion schemes can be broadly divided into two types depending on whether they attempt to maximise n or τ_E .

Inertial confinement schemes aim to assemble or compress a target to very high densities, so high that the inevitably short confinement time before the target violently disassembles is outweighed by the high momentary density. These schemes cannot be steady-state by definition, and instead a power-producing reactor would need to compress a new target multiple times per second to produce significant power output.

In contrast, magnetic confinement schemes confine only a low density plasma (around 10^{-5} times the number density of air), but for a comparatively long time. A large pressure gradient is still necessary - otherwise the reactor would need to be physically huge in order to have any region of the plasma which reached the required pressure. The magnetic confinement problem is therefore chiefly concerned with creating and sustaining large pressure gradients using a magnetic field, with transport losses low enough that the energy confinement time satisfies the Lawson criterion, and sustaining the plasma for long enough to generate a worthwhile

amount of net energy.

1.2.5 Single-particle Confinement

No solid vessel could achieve steady-state confinement at the temperatures required for fusion, because the plasma particles would lose their heat to the wall in a fraction of a second. Instead, in Magnetic Confinement Fusion (MCF) the approach is to use the gyromotion of a charged particle in a magnetic field to localise the particle, and confine it to a particular region of space.

A uniform magnetic field can be produced by a cylindrical solenoidal array of magnets. The uniform field would achieve confinement in the radial direction, but as the particles are free to travel parallel to the field lines then they will stream out of both ends of the solenoid. These losses can be mitigated by joining the ends by bending the cylinder into a torus, but the resulting inhomogeneity of the magnetic field complicates the physics.

A torus is the only shape which can meet this criteria - the hairy ball theorem for example implies that a vector field of magnetic field lines topologically-spherical surface will always have locations in which the field is normal to that surface, which would allow particles to escape.

The motion of charged particles is only circular in a completely uniform magnetic field and in the absence of collisions. Deviations from uniformity in time or space, or the presence of other body forces such as due to an electric field, will alter the motion (see [42]). If the variation or additional force is small compared to the effect of the uniform background field then we can represent these effects as higher-order corrections, which take the form of constant-velocity “guiding-centre drifts” on top of the gyromotion and the motion parallel to the field lines. For example, a spatial variation in the strength of the B -field creates a drift perpendicular to both B and the variation in B (∇B). This is because a gyrating particle will experience a stronger field on side of its orbit than the other, so it will have a different gyration (Larmor) radius, and the asymmetry causes a net drift as in figure 3. Bending the solenoid to connect the ends causes both a radial variation in field strength, and a bending of the field lines, both of which produce vertical drifts through the grad- B and curvature drift effects respectively. This continuous vertical drift will prevent the plasma being confined in a magnetic field which points purely in the toroidal direction. This happens because the grad- B and curvature drifts act oppositely on the oppositely-charged ions and electrons. The two species are therefore vertically displaced from one another by these drifts, a displacement which produces (and is limited by) the production of a vertical electric field.

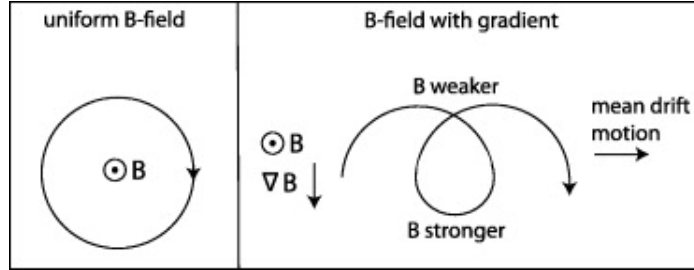


Figure 3: Diagram of the guiding-centre drift of a charged particle in a spatially-varying magnetic field.

The vertical electric field causes a new guiding-centre drift, the $E \times B$ drift, which moves both ions and electrons radially outwards, causing them to rapidly escape the confining magnetic field (we will do the ordering that shows exactly how rapidly in chapter 3).

The solution is to introduce a poloidal magnetic field, so that overall the field lines twist around the core, a “rotational transform”. As movement parallel to the field line is unimpeded, particles rapidly traverse the entire device. The rotational transform therefore causes each particle to spend equal amounts of time in the upper and lower halves of the device as they move around toroidally. The grad-B and curvature drifts are then vertically away from the core in one half, and vertically towards the core in the other, so overall no vertical electric field develops, and the particles remain confined.

1.2.6 Tokamaks

Having deduced one possible field configuration which will confine multiple charged particles, the field still must be generated by some combination of currents. While a plasma can support currents which create fields which act on itself, using the virial theorem Shafranov showed that “*any bounded equilibrium plasma configuration can only exist in the presence of fixed current-carrying conductors*”[43]. This means that some external magnets are always required to achieve steady-state confinement.

For confinement within a toroidal device we need both toroidal and poloidal magnetic fields, but we can still choose whether all or merely some of these fields are generated by fixed external magnet coils.

A configuration in which the fields are entirely generated by a set of fixed magnets is called a stellarator. In this case to achieve the rotational transform the magnetic placement must vary along the toroidal direction, leading to complex magnetic design engineering, as can be seen in figure 4.

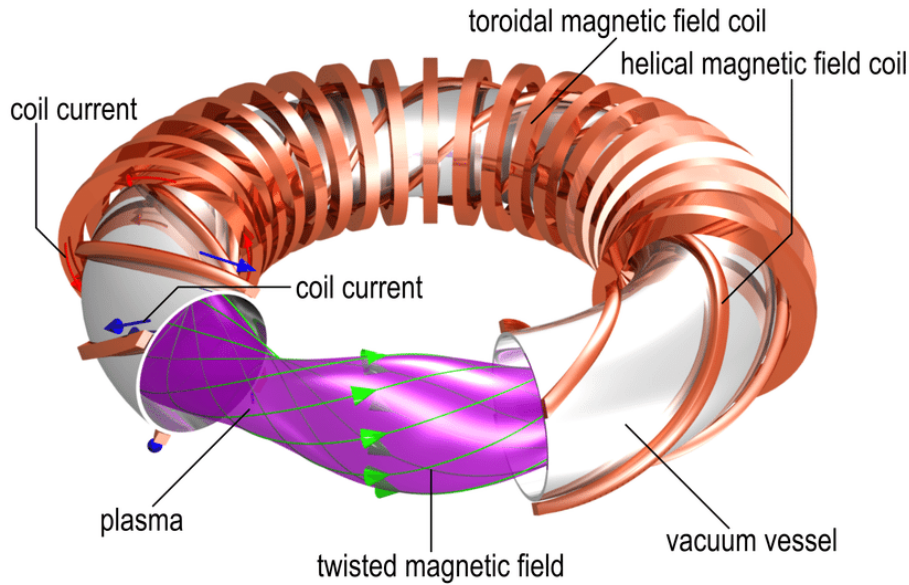


Figure 4: Schematic diagram of a stellarator, showing the various magnetic coils and fields which produce the confinement. Modern stellarator designs instead use one set of complex, twisted coils to create both the toroidal and helical field. In either case no current is required to be driven within the plasma. Figure from [44].

Alternatively, a hot plasma can support a large toroidal current, which generates a considerable poloidal field. If a steady current is driven through the torus (for example through using the plasma as the secondary coil of a transformer) then the rotational transform can be achieved with an axisymmetric magnetic field. This flexible configuration is known as a tokamak, a schematic diagram of which is shown in figure 5.

Whilst stellarators have the advantage of not required a current to be driven, Tokamaks however offer more flexibility: by varying the radial profile of the current the shape of the magnetic surfaces can be altered significantly. Tokamaks are also easier to engineer - repeating planar coils simplify design and maintenance.

1.3 Heat Exhaust

1.3.1 Power and Particle Balance

For significant amounts of fusion power to be produced, we need significant collision rates within the plasma. As we saw in section 1.2.3, this necessitates high pressure in the core, and thus large pressure gradients from the core to the edge. However, these pressure gradients

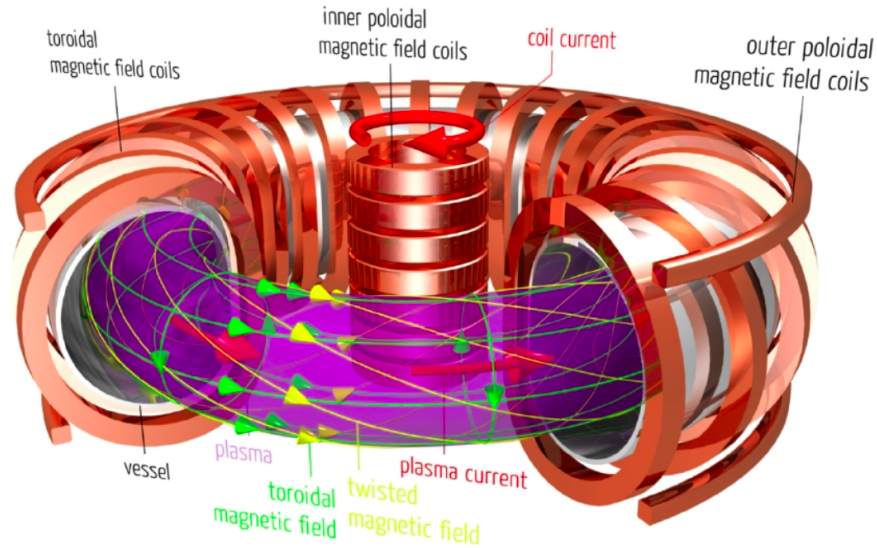


Figure 5: Schematic diagram of a tokamak, showing the various magnetic coils, magnetic fields and plasma currents which produce the confinement. Figure from [44].

create turbulence, which causes the confinement to be imperfect, as each small-scale turbulent fluctuation can cause a particle to step radially outward onto a neighbouring toroidal magnetic flux surface. Transfer of particles and heat across magnetic flux surfaces is called cross-field transport.

20% of energy from the D-T reaction is in the charged Helium ash, which must be removed from the plasma as a waste product. Furthermore, for steady-state operation then the tokamak must be regularly refuelled with a D-T mixture. The particle balance is in fact mostly dominated by neutral recycling though: plasma particles recombine into neutrals in the divertor or at the wall, freely move back towards the core, where they are ionised and slowly step outwards again. The result is a constant flow of charged particles being exhausted radially.

1.3.2 The Scrape-Off-Layer

The surface formed by the set of outermost magnetic field lines which still stay within a bounded volume (the region of confinement) is called the Last Closed Flux Surface (LCFS) or separatrix. Once particles leave the confined core by stepping across the LCFS, they follow field lines until they reach a solid surface such as the wall. Their parallel motion is rapid so there is a thin layer of plasma outside the LCFS called the Scrape-Off-Layer (SOL).

This thin layer will impinge on a narrow region of wall surface so we specifically designate that surface as the target plates. Their energy is released onto this surface, which if unmitigated will exceed the engineering limits of the surface material. Particles also sputter from the target

surfaces, which is detrimental to the core plasma performance. To minimise the amount of surface-born impurity atoms reaching the core, the target plates are physically separated by using a divertor configuration (figure 6), where a magnetic null-point (X-point) divides the core region from the target region.

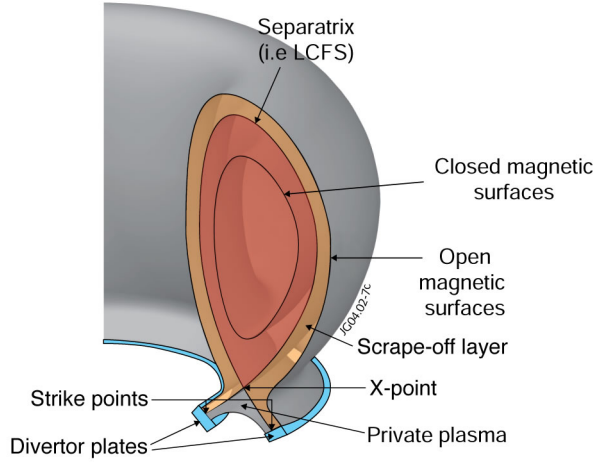


Figure 6: Diagram of a tokamak with a divertor configuration. The plasma leaks out of the core through the separatrix into the scrape-off-layer, where it flows down to the divertor plates. (Courtesy EFDA/JET www.euro-fusion.org/jet/)

1.3.3 The Exhaust Challenge

Managing the exhausted heat poses a critical challenge for any commercial power plant design. We can illustrate the magnitude of this challenge using a simple power balance argument by Militello[45]. For a reactor in steady state, with equal power flowing into and out of the plasma, we have energy conservation

$$P_{\text{aux}} + P_{\text{fus}} = P_{\text{out}}, \quad (1.7)$$

where P_{fus} is the power generated in the plasma by fusion reactions, P_{aux} is the power input to the plasma from auxiliary heating systems (such as neutral beam injectors), and P_{out} is the power coming out of the machine in all forms. The fusion power includes both alphas and neutrons, so $P_{\text{fus}} = P_{\alpha} + P_n$. The output power P_{out} includes the power that will be dissipated on the material structures surrounding the plasma, $P_{\text{out}}^{\text{bad}}$, and the power carried by the neutrons to the breeding blankets, $P_{\text{out}}^{\text{good}}$, some of which will eventually be converted into electricity. If we assume that the neutrons only deposit a small fraction of their energy in the first wall then $P_n \approx P_{\text{out}}^{\text{good}}$.

But all good neutron power comes with bad plasma heat. If we split $P_{\text{out}}^{\text{bad}}$, define the energy multiplication factor $Q = P_{\text{fus}}/P_{\text{aux}}$, and use the fact that for D-T 20% of the fusion power goes into the α particles and 80% into the neutrons, we have

$$\begin{aligned} P_{\text{out}}^{\text{bad}} &\approx P_{\text{aux}} + P_{\alpha} \\ &= \frac{P_{\text{fus}}}{Q} + 0.2P_{\text{fus}} \\ &= \left(\frac{1.25}{Q} + 0.25 \right) P_{\text{out}}^{\text{good}}. \end{aligned} \tag{1.8}$$

So bad heating is directly proportional to good output power in the limit $Q \rightarrow \infty$, and the problem is worse for finite Q .

Of course, physical structures can only take so much punishment before they melt. For the vessel wall (which needs to be relatively thin to allow enough neutrons to pass through it into the breeder blanket) this limit is around $(P/S_{\text{max}}) = 1\text{MW}/\text{m}^2$.

For a commercial reactor (and really any technology), smaller is generally better. Smaller designs in general have lower material costs, are easier to manufacture, and are more amenable to being mass-produced. By lowering the capital costs, reducing the technology lifecycle development time, and facilitating economies of scale, design size therefore has an outsized effect on the feasibility of the technology as a financial investment[46]. We therefore ask “given this exhaust constraint, what is the smallest fusion reactor we could possibly build”? Even if we imagine that $P_{\text{out}}^{\text{bad}}$ is spread evenly over the inner wall, we find a significant constraint on the smallest possible major radius of the reactor R . Assuming a perfectly toroidal vacuum vessel with an inverse aspect ratio ϵ , the surface area of the inner wall is $S = 4\pi^2\epsilon R^2$. Distributing the power evenly over this area S gives

$$R \geq \sqrt{\frac{(1.25Q^{-1} + 0.25)P_{\text{out}}^{\text{good}}}{4\pi^2\epsilon(P/S_{\text{max}})}}. \tag{1.9}$$

We can put this into context by imagining an ignited ($Q \rightarrow \infty$) reactor that produces 500MW of neutron power - a reasonable amount for a compact power plant. With a conventional aspect ratio of $\epsilon = 1/3$, this corresponding to a minimum major radius of 4m.

1.3.4 Implications for Reactor Design

Freidberg[47] describes a differently-motivated but effectively similar constraint on reactor size: the neutron flux per square metre onto the first wall cannot exceed around 4MWm^{-2} . The higher number is because only a certain fraction of the neutron energy is absorbed (the rest passes through into the breeder blanket), and the nature of the flux is different, but

a reactor with $Q = \infty$ produces 4MW of neutron power for every 1MW of alpha power, so Friedberg’s wall loading constraint turns out to be effectively functionally-equivalent to Militello’s (totally-spread out) exhaust power constraint. Friedberg also explains that a reactor which has $< 4\text{MW}^{-2}$ incident on the wall is economically sub-optimal: it is larger than it needs to be for the same power output.

If we instead constrain the reactor size using Friedberg’s neutron wall-loading constraint, we can re-interpret Militello’s power flux calculation in an illuminating way. Taking the same exhaust power, and instead of imagining it evenly spread over all the first wall (which can handle $\sim 1\text{MW}^{-2}$), we instead imagine concentrating it all onto divertor surfaces which can handle $\sim 10\text{MW}^{-2}$. Immediately then the total divertor wetted area must be at least 10% of the area of the first wall, otherwise we have exceeded 10MW^{-2} somewhere. Whilst an ideal plasma would radiate a significant fraction of power from the edge, in practice a significant fraction of the power is still transported along the field lines, so this new interpretation is arguably more representative of how divertors actually operate. However, that 10% is a *large* area to try and spread the heat over. If we had an ITER-width SOL ($\lambda_q=1\text{mm}$ upstream[48]) in our minimally-sized $P_n = 500\text{MW}$ reactor ($R = 4\text{m}$, $\epsilon = 1/3$), the wetted area (so with no attempt to spread the plasma exhaust load out through through any method) would be roughly

$$2\pi R\lambda_q = 25\text{mm}^2. \tag{1.10}$$

But in order to stay below an average of 10MW^{-2} we would need to spread the heat evenly out over

$$0.1 \times 4\pi^2\epsilon R^2 = 21\text{m}^2, \tag{1.11}$$

an area almost 3 orders of magnitude larger!

A 4m-wide ITER may sound like an extreme example, but for a power plant it’s not: the much-lauded ARC design[49] has a considerably higher power density ($P_{\text{out}} = 708\text{MW}$, $R = 3.3\text{m}$). Further, if you take the Eich scaling[48] of $\lambda_q \propto B_{\text{tor}}^{-0.8}R^0$ to be broadly correct, and maintain the same neutron power flux at the wall, then the exhaust situation only gets worse for larger reactors (which produce more power), and for higher-field reactors (which shrink the SOL width). If instead you relax the wall loading constraint, then as Friedberg shows, the result is a larger design for the same power: easier to build, but inevitably less economically-attractive.

These arguments are not at all rigorous, but they do illustrate three important points:

1. Any cost-optimal fusion power plant will need to operate near the limit of what its

material surfaces can handle almost everywhere inside the plasma chamber,

2. The plasma exhaust power will need to be evenly spread out over a very wide area by the divertor, much wider than the current estimations of the natural width of the scrape-off-layer at the mid-plane,
3. Even after sufficient spreading is achieved then the divertor surfaces specifically will be continuously operating near their 10MW^{-2} material limit.

It should therefore be no surprise that the heat exhaust challenge has famously been referred to as “probably the main challenge towards the realisation of magnetic confinement fusion” [50].

1.3.5 Difficulties with divertor solutions: No Silver Bullets

Surely there must be some way we can engineer ourselves out of this problem? While there are many different design ideas that can help, unfortunately none of these offer a single solution alone, and most come with compromises in other parts of the reactor design. We will now briefly review the main possibilities and show why although they are all potentially useful, the limitations of each imply that there is no single easy solution to the heat exhaust challenge.

Double divertor

Some tokamaks, such as MAST, are designed to operate in a double-null configuration, meaning there are (at least) two null-points in the magnetic field, one above and one below the core plasma (see figure 7). Each of these X-points has its own divertor, usually symmetric about the horizontal plane. This creates two separatrices in general, but with the magnetic field aligned to sufficient precision (or rapidly cycling between disconnected upper null and disconnected lower null configurations), 50% of the exhaust power can be directed to the upper divertor and 50% to the lower. This would immediately halve the heat flux onto all divertor surfaces compared to the single-null case. However while factor of two reduction in heat flux is helpful, clearly it won't span the nearly 3 orders of magnitude we need on its own.

A double-null also brings significant drawbacks for a reactor design. Firstly it occupies twice the solid angle around the plasma, absorbing a significant fraction of the neutrons which ideally would be entering breeding blanket modules instead. While a Tritium Breeding Ratio

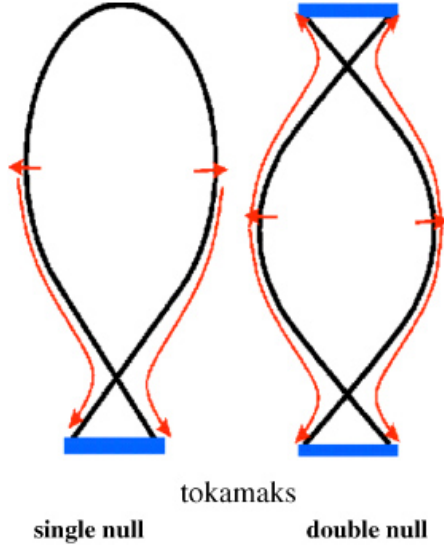


Figure 7: Double null geometry vs a single null. Diagram from [51].

> 1 is still technically achievable[52], this makes another major design constraint significantly tighter.

Secondly divertors are likely to be very expensive components, which require regular replacement. Assuming that two divertors have to be replaced just as often as one, this would significantly increase the maintenance costs of a commercial power plant.

Finally the control of the magnetic field necessary to maintain a connected double-null is very fine. If the two separatrices move out of alignment by mere millimetres, the advantage of the double null is lost and the divertor will be quickly burnt.

Tilted target plates

Calculating the heat flux per unit area by multiplying the width of the Scrape-Off Layer by the circumference of the plasma assumes that the target plates are normal to the magnetic field lines.

If instead the target plates are tilted such that the angle between the field lines and the material surface is θ , then the flux per unit area would be decreased by a factor of $\sin \theta$.

However the grazing angle θ cannot be arbitrarily small - in reality the target consists of multiple tiles, each of which has a leading edge which instead becomes subject to the heat flux at small θ . These considerations lead to ITER using $\theta = 2^\circ$, capping the benefit to heat flux mitigation at a factor of around 30 lower.

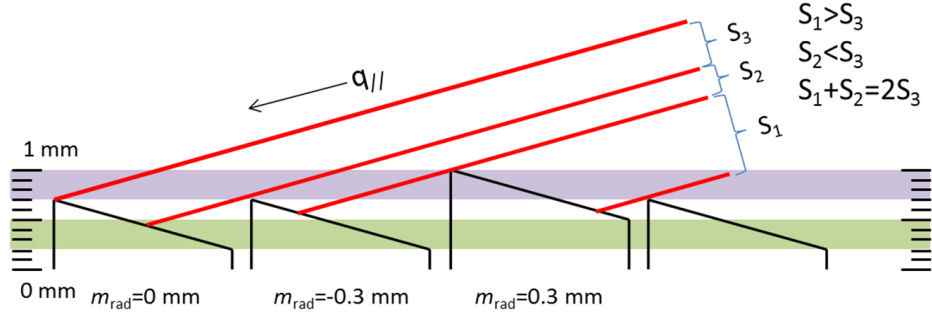


Figure 8: Magnetic field lines tilted with respect to the divertor target plates, to reduce the heat flux q_{\parallel} onto the material surfaces. The surfaces are made up of multiple tiles, which must have slanted surfaces so as not to present exposed leading edges. In reality the field lines are also tilted poloidally, so have a large component into the page on this diagram. Diagram from [53].

Flux expansion

As the charged particles largely follow the magnetic field lines all the way to the targets, spreading these field lines apart will also spread the heat load on the targets.

This is known as poloidal flux expansion[54], and is one aim of the design of advanced divertors[55], especially the Super-X divertor configuration planned for use on MAST-Upgrade[56]. (The projected benefits of the MAST-U Super-X have been investigated through a series of SOLPS simulations[57, 58].)

Whilst poloidal flux expansion is obtained by reducing B_{poloidal}/B at the target, additionally “total” flux expansion can be obtained by moving the strike point radially further outwards (see figure 9).

Again however these benefits are limited: poloidal spreading is limited by the area of the divertor chamber, and radial expansion by the radial position of the toroidal field coils. Poloidal flux expansion is also a trade-off with target field line angle: if the minimum angle is fixed to 2° , then that can be achieved by tilting plates or poloidal flux expansion, the plates cannot be tilted to 2° and then the poloidal flux expanded further.

Additionally, as the divertor chamber must be fully enclosed by the toroidal field coils, expanding the flux either toroidally or poloidally requires increasing the distance of the toroidal field coils from the centre of the plasma. This inhibits magnetic control of the core plasma, increases the total stored energy in the field, and reduces the B-field on-axis - all of which reduce the feasibility of the core plasma scenario for a power-producing tokamak. Flux expansion therefore represents a design trade-off.

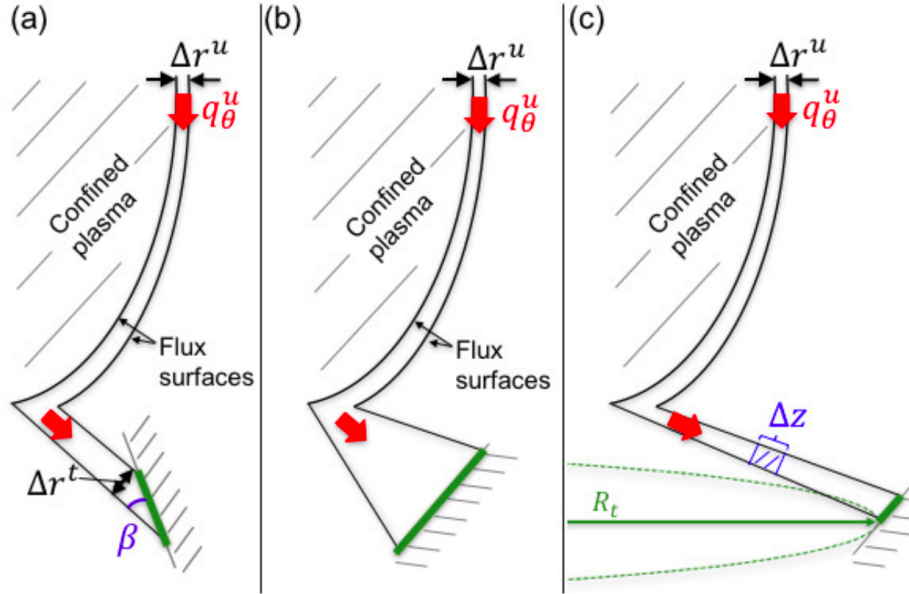


Figure 9: Schematic diagram of methods of heat flux reduction by geometric means. (a) shows poloidal tilting of the target plates, (b) poloidal flux expansion, and (c) toroidal flux expansion by increasing the target strikepoint major radius R_t . Diagram from [59].

Stronger material

There are several constraints which limit the choice of materials to use for the target plates. The first is tritium retention - a fusion reactor needs to conserve its tritium carefully in order to maintain a Tritium Breeding Ratio above 1 (higher again to contribute to the startup of new fusion reactors). The amount of tritium that can be on site at any one time is also limited by nuclear safety regulations, which includes tritium embedded into materials. This rules out using plasma-facing components which will easily chemically bond to hydrogen, which importantly excludes the carbon walls that have been used on many experimental devices.

The second is neutron activation. Whether or not the low-level waste criterion is met depends on the exact choice of neutron-facing materials. Some materials which would have higher melting points than pure Tungsten (such as Molybdenum) cannot be used without relaxing the LLW criterion, as they would activate to a degree which easily exceed the activation limits set out by nuclear regulatory authorities internationally, and produce significant volumes of intermediate-level waste. This is a valid option however, and Molybdenum has other desirable material properties compared to Tungsten in addition to its higher melting point.

These two constraints are some of the largest - taken together this means that the only way

to open up new possibilities for using materials which can handle a higher heat flux than Tungsten is to relax nuclear regulations. A practical material choice also has to have low enough cost, be manufacturable, have a high melting point, high thermal conductivity, and high sputtering threshold.

Detachment

If the thermal flux flowing along the field lines to the target were converted into isotropic heat flux, it could be deposited over a much wider surface area. This can be partially achieved through “detachment”, where a buffer of neutralized gas is formed in front of the target plates. The upstream power is then transferred into both the neutral gas and impurities through collisional processes, especially through the excitation of impurity species. When these species subsequently re-radiate, they isotropically spread the heat flux over a much wider area (as shown in figure 10).

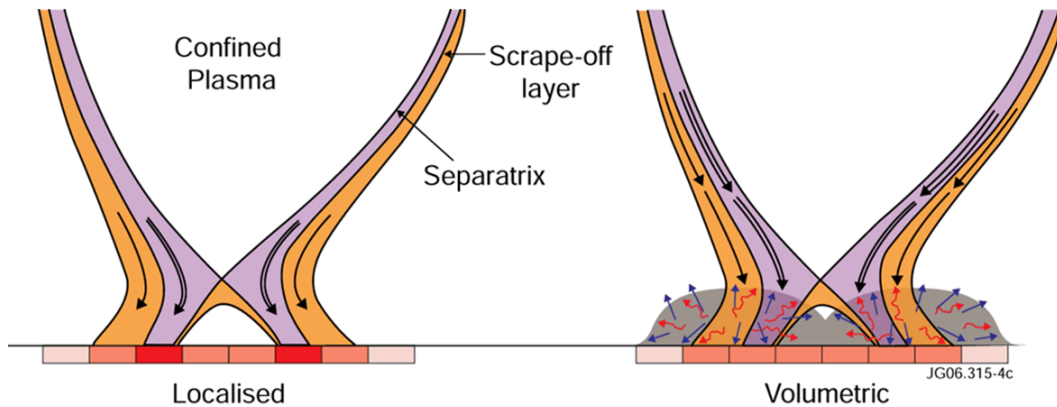


Figure 10: Schematic diagram of peak heat flux reduction through volumetric radiation of energy near the target plates. Diagram from [60].

In the ideal limit 100% of the upstream power would be radiated. This is known as “ultimate detachment”, defined[61] as when the particle ion flux at the target reaches zero, which implies that the conductive ion energy flux equals zero, and all the power must have been instead lost through radiation (or transferred to neutrals).

If all power were converted to radiation then the width of the SOL would no longer set the heat flux density at the target. However, not only is 100% radiation very difficult to achieve, but even in that ideal regime the SOL width is still important. The width of the SOL affects how easy it is to access the density and temperature regimes at the targets that are required to achieve detachment, as well as the total volume from which the fixed power must be radiated. The SOL width also affects the upstream separatrix density for a given

SOL power, which sets a boundary condition on the core plasma profiles.

Finally, radiation through impurities in the divertor also introduces the danger of those impurities migrating back up to pollute the core plasma, and can cause radiative instabilities. The original motivation for diverted tokamak designs was in fact to keep these impurities physically-separated from the core.

Conclusion

Tilting, flux expansion and detachment will all need to be employed simultaneously to limit heat flux to acceptable levels.

Even then, the divertor heat flux is likely to be a limiting factor in the design of tokamak power plants, so it is crucial to be able to understand and predict the processes which set the width of the Scrape-Off Layer.

1.4 Thesis Outline

In this chapter we have introduced fusion energy, discussed its advantages and disadvantages, and introduced the challenges of divertor heat management.

In chapter 2 we first review literature on the turbulent transport processes setting SOL width, how the SOL is experimentally-diagnosed, and common approaches to computationally modelling the SOL.

Next we describe in detail in chapter 3 the physical model used in the rest of this thesis, with a derivation of the equations solved, boundary conditions, and various assumptions. We also describe how reduced two-dimensional models of the SOL can be obtained from more complex three-dimensional models.

Then in chapter 4 the computational methods used are described, including a description of the general architecture of the BOUT++ framework and the STORM module.

Chapter 5 systematically compares the results of 2D and 3D simulations of the SOL, and the effect of varying parameters in 2D and 3D.

Chapter 6 adds a core region to the 2D models, and explores resulting challenges. In particular we describe the spontaneous formation of strong binormal mean flows.

Chapter 2

Review of Scrape-Off-Layer Turbulence

2.1 Introduction

This chapter will give an overview of the important processes governing SOL turbulence. The first half reviews the key experimental measurements of the SOL, and in particular how both 1D probe time series and 2D imaging techniques point towards an intermittent process dominating the SOL turbulence, made up of individual filamentary-like plasma structures. The second half reviews attempts to model this turbulence, in order of increasing complexity rather than chronological order, starting with a description of the physics of isolated filaments and working up to full simulations of SOL turbulence.

2.2 The Character of Radial Transport

2.2.1 Non-diffusivity

In the core plasma the basic picture of confinement is that radial gradients drive transport which can be treated as effectively diffusive. In a diffusive case the transport follows Fick's law

$$\Gamma_{\perp} = -D_{\text{eff}} \frac{\partial n}{\partial r}, \quad (2.1)$$

where Γ_{\perp} is the radial particle flux (perpendicular to the magnetic field), n is the local particle number density, r is the radial position coordinate, and D_{eff} is the effective particle diffusivity coefficient in the perpendicular plane (assumed to be a constant here). Within this paradigm the challenge is to identify the small-scale mechanisms which cause that diffusivity, in order

to predict how it will scale with plasma parameters.

This paradigm was also assumed for SOL transport: a 1999 review of different theories of SOL transport generally assumed that a similar flux-gradient relationship held in the SOL [62].

In a diffusive picture the Bohm scaling[63] was considered to be the largest imaginable rate of diffusive transport in the core, with classical diffusion being the smallest. However experimental measurements of SOL transport did not fit with this picture - for example SOL density profiles in ASDEX could only be reproduced in simulations either by assuming a large radial drift or an effective particle diffusion coefficient D_{eff} much larger than the Bohm value [64].

Density profiles in the SOL generally decay exponentially from the separatrix, which was originally interpreted as being due to the dominance of strong parallel flows in removing particles, combined with a D_{eff} that was approximately constant in space. However, Umansky et. al.[65] and LaBombard et al.[66, 67] measured profiles and fluxes in Alcator C-mod, and noticed the persistence of large transport when profiles were flat. In a purely-diffusive paradigm (such as that described by (2.1)) this would imply that effective diffusivities increase with radial distance from the separatrix, a counterintuitive result shown in figure 11. This radial variation was also seen in the JET, DIII-D and TCV tokamaks [68–70], and also when estimated from turbulence codes such as ESEL [71].

For DIII-D no diffusion coefficient could be found which fit the experimental edge profiles when using UEDGE transport simulations[72]. In order to fit the profiles an effective anomalous velocity V_{eff} which varied both radially and poloidally was needed.

$$\Gamma = -\hat{D}_{\text{eff}} \frac{\partial n}{\partial r} + n \hat{V}_{\text{eff}} \quad (2.2)$$

However, Garcia et. al.[70] and Naulin[71] attacked the idea of parametrizing SOL radial transport in terms of effective diffusion and velocity coefficients entirely. They argued that if the SOL transport could be modelled as advective-diffusive, then the normalised particle flux would follow an linear relationship with inverse density scale length as

$$\frac{\Gamma}{n} = \hat{V}_{\text{eff}} - \frac{\hat{D}_{\text{eff}}}{n} \frac{\partial n}{\partial r} = \hat{V}_{\text{eff}} + \frac{\hat{D}_{\text{eff}}}{\lambda_n}, \quad (2.3)$$

where \hat{V}_{eff} is an effective radial advective velocity and \hat{D}_{eff} an effective radial diffusion, both parameters to be determined.

But figure 12 shows that for a range of TCV plasmas, not only is there not a linear relationship, but there is not any clear functional relationship at all. Linearity would correspond

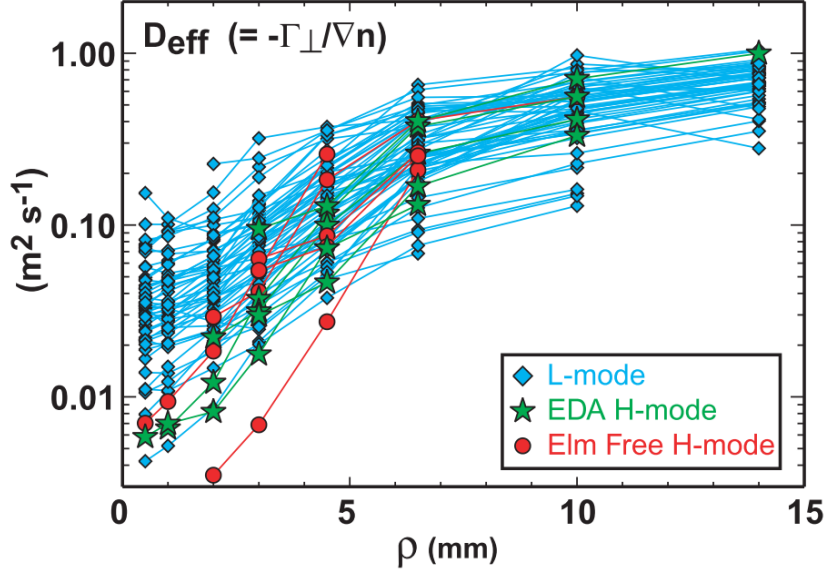


Figure 11: Effective cross-field particle diffusivity profiles for a range of Alcator C-mod plasmas. They show that if radial particle transport in the SOL is assumed to be a diffusion-like process, then the local diffusivity coefficients would have to increase radially into the SOL in order to produce the exponentially-decaying density profiles observed. Figure from [66]

to transport coefficients that are radially-constant, but even if the transport coefficients had a radial dependence (as a result of radially-varying averaged plasma quantities) one would expect this plot to display some functional relationship. The fact it doesn't indicates that the physics of SOL transport cannot be consistently parameterized by an effective advective-diffusive model, and more complex physics is important, likely requiring first-principles understanding to parametrize. (This also indicates that fitting a Fokker-Planck diffusion law as described in [73] is also unlikely to work well.)

More recent attempts to parametrize SOL turbulence have applied a $k - \epsilon$ model, inspired by the Reynolds-Averaged Navier-Stokes approach often used in neutral fluid turbulence. These models treat the turbulent kinetic energy as the quantity to be diffused, but still require setting coefficients through a closure obtained from an empirical global scaling law, so are not truly first-principles models[74].

It turns out that the small-scale properties of SOL turbulence are significantly different to that of the core, and are illuminated by specific experimental data.

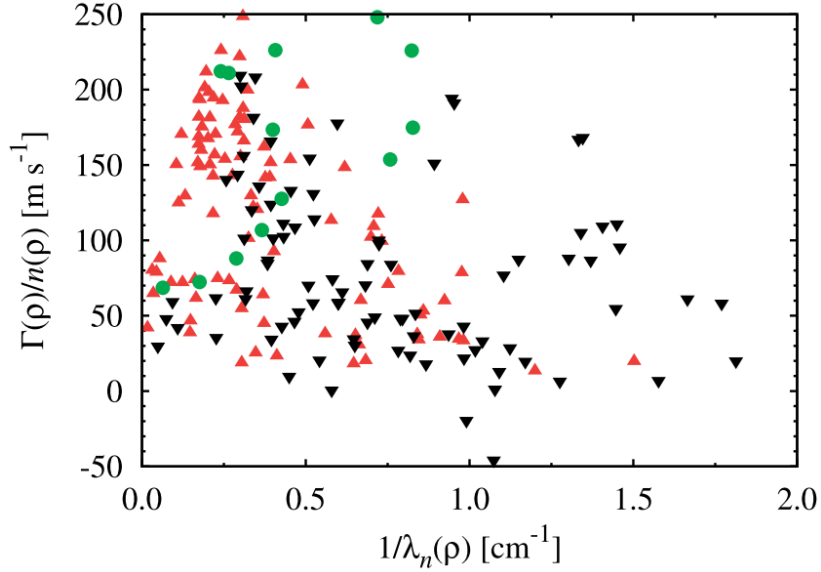


Figure 12: The relationship between radial particle flux and density gradient scale length for a range of TCV plasmas. The lack of any clear correlation shows that there is no simple description of SOL transport involving effective radial diffusivities that are a simple function of radial position. This indicates that the underlying transport processes are much more complex, and not well described by a gradient-flux relationship. Figure from [70]

2.3 Experimental measurements

Although multiple different diagnostic instruments can be applied to the SOL, two in particular are responsible for important insights into the nature of SOL turbulence. We will now see how timeseries from Langmuir probes showed the inherent intermittent properties of the SOL, and fast cameras revealed its filamentary structures.

2.3.1 Langmuir Probes

A Langmuir probe consists of a conducting element inserted into the plasma, which draws a measurable current. Since their development by Irving Langmuir in the 1920s, they have been a workhorse diagnostic tool for laboratory plasmas[75, 76].

As the probes must physically penetrate the plasma, they can only tolerate short dwell times before they are damaged by the neutron and charged particle fluxes. They are therefore limited to diagnosing the boundary region of tokamak plasmas, and must quickly plunge in and out, as for example the reciprocating probes on MAST do[77].

Whilst it is the drawn current which is measured directly, the probe can be biased to a particular voltage before insertion into the plasma. The voltage of the probe affects the flux

of electrons to its surface, and by sweeping through a range of values, information about the plasma density, temperature, potential, and distribution functions can be deduced [78, 79]. If the biasing potential is sufficiently negative, then all electrons (and negatively charged ions) will be repelled from the probe. In that case the drawn current will be solely due to ion flow - the so-called ion saturation current. It can be shown that

$$I_{\text{sat}} \propto n_e \sqrt{T_e + T_i}, \quad (2.4)$$

where n_e is the electron number density, T_e is the electron temperature and T_i is the ion temperature. This proportionality means that fluctuations in signals of I_{sat} are good proxies for fluctuations in density and/or temperature, as can be seen for example in the time traces shown in figure 14.

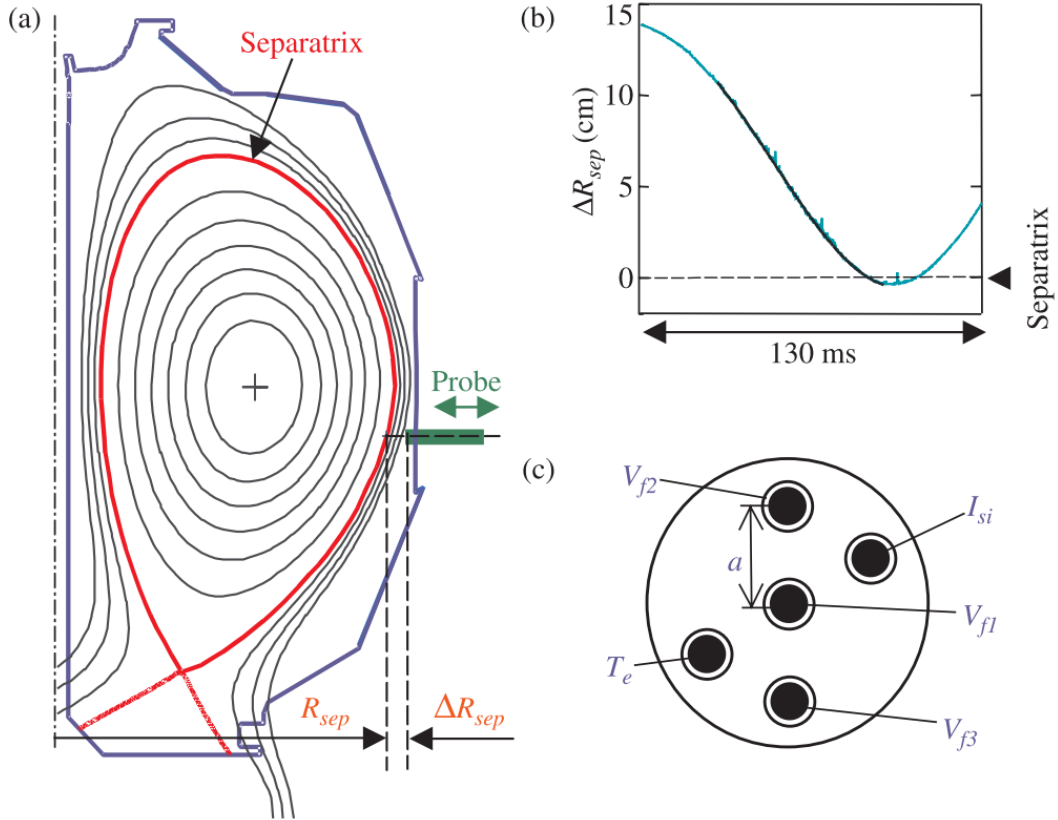


Figure 13: Schematic of the mid-plane Langmuir Probe Diagnostic on DIII-D: (a) shows the poloidal location of the reciprocating probe, and the line it traces when plunging into the plasma, to a depth just past the separatrix; (b) shows a typical position over time trace for the probe on the inner part of its plunge; (c) shows the probe head layout, with multiple tips allowing for measurement of spatially-dependent quantities such as the electric field. Figure from [80].

Langmuir probe heads often have multiple tips, such as the mid-plane probe on DIII-D shown in figure 13. By taking different measurements at slightly separated spatial locations, quantities involving speeds or gradients can be deduced, for example the average electric field between two tips[80].

As the probe changes spatial position as it plunges into the plasma, measurements along a radial line can be taken, allowing probes to be used to construct a picture of the density and temperature along a radial profile of the plasma.

Whilst the probe head only dwells in the plasma for a fraction of a second, that is much longer than typical turbulence correlation times ($\sim \mu s$), allowing the tips to collect long timeseries of fluctuation data. By binning this data in time, a reciprocating probe can be used to gather radial profiles of the fluctuation statistics.

2.3.2 Intermittent Fluctuations

The Langmuir probe time signals from various tokamaks in figure 14 show fluctuations over time which are highly intermittent. The fluctuation levels in the SOL are very large compared to the mean value - for example in the Caltech tokamak fluctuations of 10-90% of the mean are observed routinely[81]. This is much higher than in the core, which has fluctuation levels of only around 1% [82].

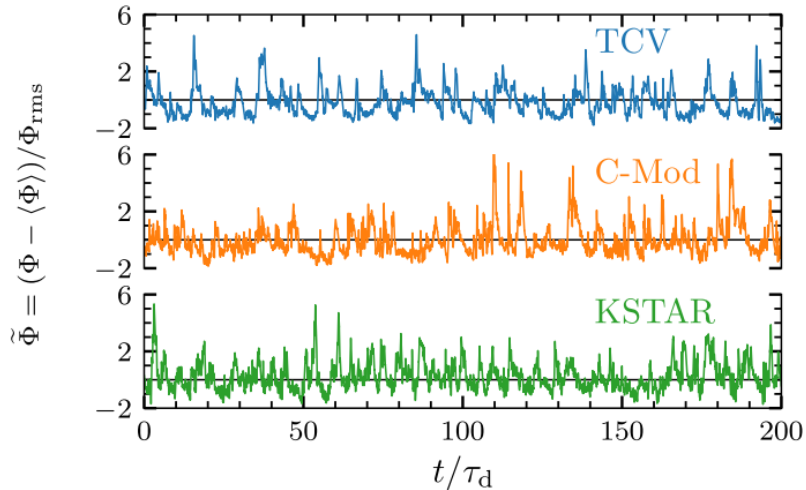


Figure 14: Examples of fluctuations in timeseries measured using Langmuir probes in different tokamaks. Intermittent large events, several times larger than the standard deviation, can be seen. The mean values of each timeseries are indicated by the solid lines. The time is normalised to the characteristic duration time of the large-amplitude bursts τ_{au_d} . Figure from [83].

The signal is also clearly asymmetric: disproportionately large positive bursts are common, but negative bursts are not. Whilst rare, these individual large events are important - Antar et. al. [84] found that the fluctuations comprising the top 20% of the value of the signal account for about 50% of the radial transport near the last closed flux surface.

This type of intermittency is a universally-observed feature of scrape-off layer plasmas. Antar et. al.[84] superimposed normalised fluctuation signals from Tore Supra, Alcator C-mod, MAST, and PISCES (figure 15), and found that they all condense onto a single probability distribution function (PDF). This set of machines included diverted machines (C-Mod), limited machines (Tore Supra), spherical machines (MAST) and linear machines (PISCES) - on linear machines plasma rotation creates a centrifugal force which plays a similar role to the curvature drift in tokamaks[85]. The set displaying universal behaviour was later extended to include the W7-A and and TJ-II stellarators[86].

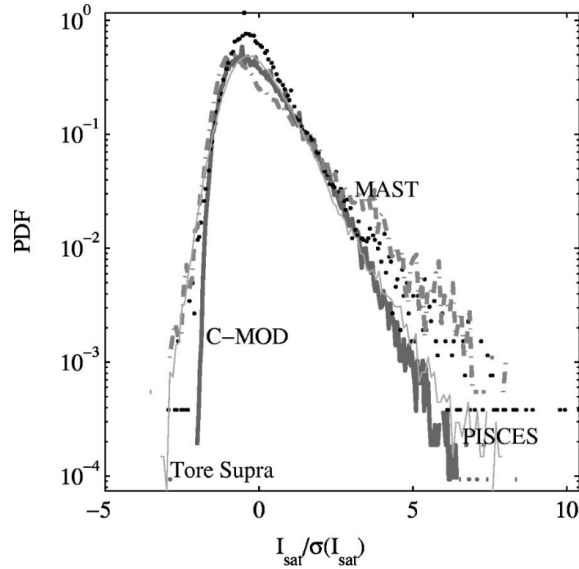


Figure 15: Figure from [84], showing universality of ion saturation fluctuation probability density functions across a range of machines.

2.3.3 Statistical Properties

The prevalence of positive fluctuations over negatives ones means that the Probability Distribution Function (PDF) of the signal from a 1D timeseries is positively-skewed. Another common feature is that this positive skew generally increases further out into the SOL. Figure 16 shows that in the core and edge, the PDFs of the fluctuations are close to Gaussian, with

a low skewness S , defined by

$$S = \frac{1}{N} \sum_{i=1}^N \frac{(X_i - \bar{X})^3}{\sigma_X^3}, \quad (2.5)$$

where X is a variable with a timeseries consisting of N points, with a mean \bar{X} and a standard deviation σ_X . In the far SOL however the skewness increases considerably, and the PDFs display a long tail representing the rare but consistent large positive fluctuations in the signal. The likelihood of these rare events is further enhanced by the high kurtosis of the signal, K , defined as

$$K = \frac{1}{N} \sum_{i=1}^N \frac{(X_i - \bar{X})^4}{\sigma_X^4}, \quad (2.6)$$

for which values greater than 3 imply that the distribution has tails that asymptotically approach zero more slowly than a Gaussian, and therefore produces outliers more often than the normal distribution does. As the normal distribution has a kurtosis of exactly 3, it is common practice to instead use the excess kurtosis, defined as $K - 3$. The kurtosis is also sometimes referred to as the flatness, because a symmetric increase in the weight of both tails can be roughly imagined as having partially “flattened” the distribution.

The temporal power spectra of the fluctuations also show remarkable universality. Across multiple devices [84, 89, 90] the frequency power spectra collapse onto the same curve, for example as in figure 17. This correspondence requires a rescaling of the frequency axis. In figure 17 the scaling parameter is an arbitrary λ , but the scaling constant can also be identified with a characteristic duration time τ_d , interpreted as a typical duration of one of the large-amplitude bursts in the signal[91]. In general the power spectra are observed to be flat at lower frequencies and then fall off with a power law at higher frequencies.

The statistics of these signals are consistent with a superposition of independent, uncorrelated pulses arriving according to a Poisson process, producing a PDF of waiting times between events described by a Gamma distribution[83, 92–94]. This statistical model is known as “shot noise” in the context of noise in vacuum tubes[95].

2.3.4 Optical imaging diagnostics

Whilst the statistics of 0D timeseries suggest that the SOL turbulence contains intermittently-emitted structures, 2D imaging diagnostics are required to actually observe the form of these objects.

The SOL emits light primarily through line emission generated by interactions between the charged plasma and neutral atoms. If the density of the neutral atoms in the chamber is n_0 , then the intensity of line emission from collisional excitation of neutral atoms, I_{opt} , is a

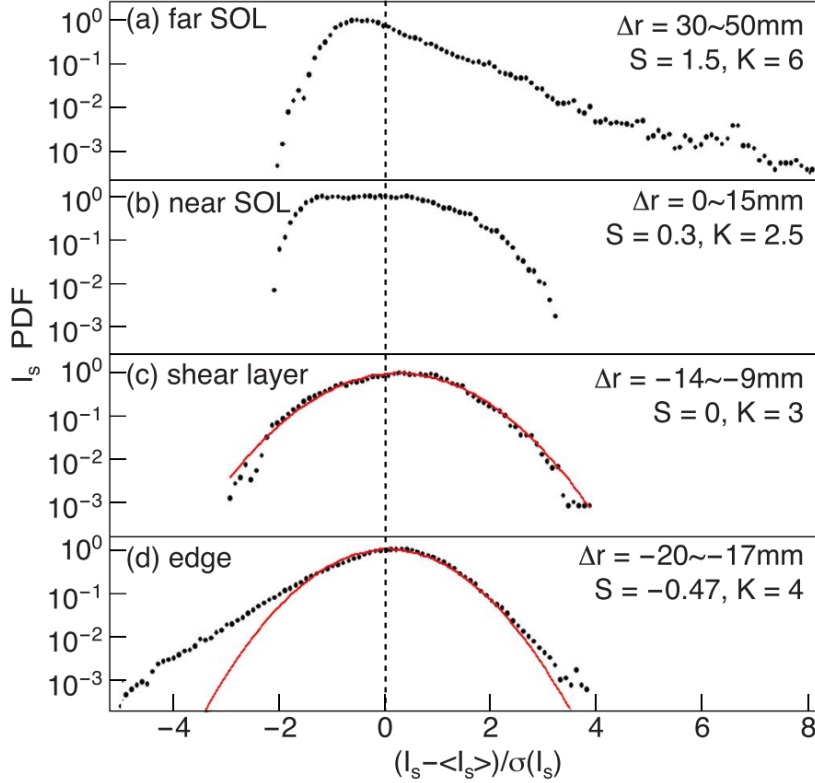


Figure 16: Probability distribution functions (PDFs) of fluctuations in ion saturation current signals plotted at various radial positions in the edge plasma of JET. As we move out from the core to the far SOL (so following (d) to (a) and increasing the distance from the separatrix Δr), the signals become more intermittent, with increasing skewness S and kurtosis K . At each location, the skewness S and kurtosis K broadly follow an expected parabolic relationship between one another (see eq. (2.12) in [83]). The shear layer is a region of strong perpendicular flow shear just inside the separatrix, where filaments are thought to be born[87]. Figure from [88].

function of plasma density and electron temperature[96]

$$I_{\text{opt}} = n_0 f(n, T_e). \quad (2.7)$$

Optical measurements of the SOL usually look at line emission from the D_α transition (656.28 nm), from the Balmer series of Deuterium. Whilst the precise form of $f(n, T_e)$ can only be determined from a collisional-radiative model, for densities and temperatures relevant to the SOL it depends linearly on n_e and less strongly on T_e , similarly to I_{sat} [97].

As D is almost completely ionised above $\sim 100\text{eV}$ [98], then n_0 is negligible far inside the the core. This has the convenient effect of only producing light from the structures in the edge and the SOL, without images being washed out from light from the much larger core plasma

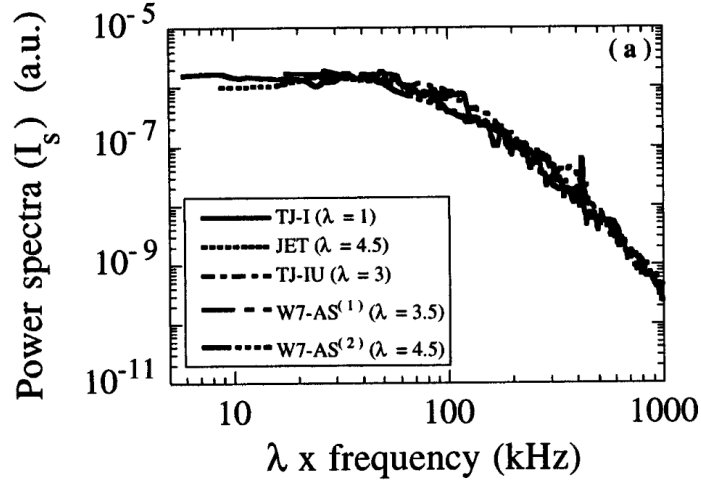


Figure 17: Temporal power spectra of fluctuation time series from various machines. The frequency axis is rescaled, after which the spectra from various machines collapse onto a single curve. Figure from [89].

behind.

Gas puff imaging

The local neutral density can be increased by gas puffing, in which D (or He or N_2) is injected near the outer mid-plane in order to locally enhance line emission. Gas Puff Imaging (GPI) setups have been used on NSTX[99], Alcator C-Mod[100], and ASDEX-U[101], and give a 2D image of a localised region of the SOL. Figure 18 shows some gas puff images on NSTX, in which localised “blob” structures can be seen, propagating both poloidally and radially outwards. Measurements combining Langmuir probes with GPI in the same flux tube have been performed, which observe correlations confirming that the same structures are the cause of the intermittent bursts in the probe time series and the imaged blobs[102].

Wide-angle fast camera imaging

While gas puff imaging only focuses on a small region of the plasma, wide-angle visible imaging can view almost the entire plasma at once. It also relies only passively on the neutrals already present in the machine, instead of actively injecting more neutral gas at a specific location. This requires that the background neutral density be high enough that the light intensity is detectable, and also that there is sufficient space between the wall and the edge to obtain a wide angle view of the plasma. MAST has both of these features and so has been regularly used for wide-angle fast camera imaging studies[104], but the technique has also been used

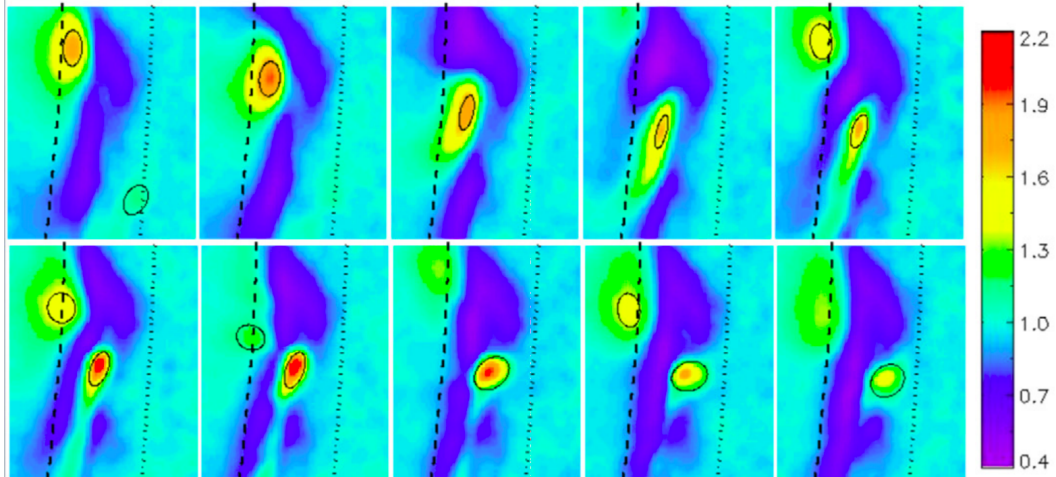


Figure 18: Gas puff images of blobs in NSTX. The images show the D_α emission over a 24×30 cm region, with a frame rate of 100 kHz. Individual blobs are labeled with black ellipses, the separatrix with a dashed line, and the limiter shadow with a dotted line. The movement of individual blobs in the perpendicular drift plane can be seen between frames. Figure from [103].

on TCV [105], COMPASS [106], ASDEX [107], TORPEX [108] and TFTR [98].

Fast cameras were first used in 1982 on ASDEX[110], but since then have improved greatly, and can now get resolutions and frame rates high enough to resolve and track the motion of individual filaments.

By obtaining the magnetic geometry from another source, it is possible to use this constraint to perform a tomographic inversion on the emission intensity data, and “unfold” the fast camera filament data into blobs shown in the perpendicular plane [106, 111]. This technique then allows the measurement of radial and poloidal velocities of individual filaments. (It does however rely on the assumption that the magnetic field structure is constant, so whilst suitable for L-mode filaments it is less applicable to ELM filaments for example, which carry a much more significant current.)

2.3.5 Filaments

While the fit of the 1D statistical observations to a Poisson process suggested the intermittent passage of radially-localised structures, it was not until the development of 2D diagnostics such as probe arrays[112] and high-speed cine-films[110] that the spatial structure of these objects could be observed. The passage of filaments can also be observed with other diagnostics, for example Gundestrup probes, which measure plasma flow velocity[113], and beam-emission

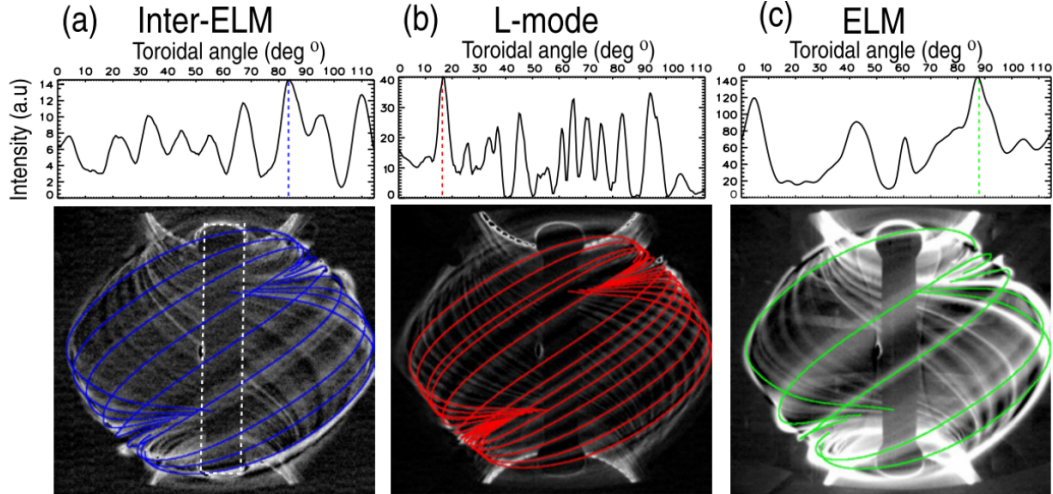


Figure 19: Wide-angle fast camera imaging on MAST. D_{α} light emission is shown for snapshots during (a) an inter-ELM period, (b) L-mode, (c) during an ELM. Elongated filamentary structures can be seen, representing localised “blobs” of density aligned along the field lines. The top row shows the intensity as a function of the toroidal angle across the centre column, and the coloured lines are used to label the filament of peak intensity. Figure from [109].

spectroscopy (BES[114].)

These intermittent structures are observed to be localised in the perpendicular drift plane, aligned along the length of the magnetic field, and elongated (so $k_{\parallel} \ll k_{\perp}$). Whilst the absolute physical sizes of the structures scale with dimensionless physical parameters, the objects typically have a perpendicular width of $\sim 1\text{cm}$, speeds of $\sim 0.5\text{km}^{-1}$, and temperatures of $\sim 10\text{eV}$ [93, 115, 116]. For example in MAST the structures have typical perpendicular sizes of $0.1 - 2\text{cm}$, density variations of $0.1 - 4$ times the background, radial velocities of $0.5 - 2\text{kms}^{-1}$ and lifetimes of $40 - 60\mu\text{s}$ [117, 118]. They are known as filaments, though they have also been referred to as blobs (for their appearance in a 2D plane perpendicular to the field lines), intermittent plasma objects (IPOs), solitary vortices, and avaloids.

As the filaments move outwards they carry particles and heat more rapidly than diffusion would alone. The fast transport along the field lines then drains the particles and heat, depositing them into the divertor target plates. The result is that, averaged over many filament lifetimes, the radial profiles of heat and particle deposition are determined in large part by the behaviour of these objects, and the statistics of the SOL fluctuations by their frequency and size.

Using techniques like fast camera imaging it is now possible to track individual filaments over their lifetime [106, 111], allowing analysis of their individual trajectories from birth to death.

2.3.6 Practical Importance of Fluctuations

Besides being an interesting physical phenomenon, it is worth enumerating the various ways in which SOL fluctuations are important for plasma scenario development and reactor design limits in general.

The sputtering at the target depends on the statistics of the fluctuations - not just on the mean values of the plasma quantities. That is because there is typically a threshold energy for sputtering to be caused by an incoming particle[119], and fluctuations can cause this value to be exceeded for significant fractions of time, even if the mean value of the time series is below the threshold[83].

The broadening of the density profiles into a shoulder has been linked to the onset of detachment in ASDEX [120] and JT-60U [121].

Filamentary transport has also been linked to the density discharge limit[122, 123], a key but poorly-understood empirical stability boundary [124], which is a major constraint on possible reactor design[47].

The filamentary structure of the SOL also has implications for radio-frequency plasma heating schemes. The wavelength of the incoming RF waves($\sim 3.6\text{cm}$ in vacuum) is similar enough to the size of and spacing between the filaments that they are strongly diffracted as they pass through the SOL, reducing the precision of the heating[125–127].

2.4 Theory and simulation

2.4.1 Transport vs turbulence codes

Within computational edge modelling there are two main types of simulation codes used: transport codes and turbulence codes.

Transport codes approximate some part of the turbulent diffusion (of particles, momentum and heat) through the plasma, often using empirically-calibrated coefficients to broadly represent these processes. These codes are useful for characterising different experimental scenarios, and modelling the impact of other physics (such as neutral particles, discussed in 2.4.2).

Turbulence codes instead resolve some of the spatial and temporal scales important for turbulent processes, ideally aiming to predict turbulent transport from first-principles, without experimental calibration. These codes are more useful for theoretical investigations into the mechanisms of the underlying turbulence in a given regime, and for making predictions about

the plasma's behaviour outside of regimes for which we have experimental data.

We have already covered in section 2.2.1 how the former type of time-averaged effective transport code (such as SOLPS[128]) cannot capture the intermittent turbulent radial plasma transport. Instead we often employ fluid and gyrofluid models which can evolve smaller, slower fluctuations on a MHD-stable background.

2.4.2 Complex physics

Simulating all of the different physical effects which are known to matter in the SOL is extremely challenging.

Whilst turbulence codes do simulate a wider range of the necessary temporal and spatial scales, these codes are still missing a lot of potentially important physics. The collisional and $k \gg \rho_s$ assumptions used in fluid codes hold for filaments in a cold SOL divertor, but do not hold in the pedestal, meaning that kinetic effects (which require much more expensive codes[129]) can become important for integrated modelling. Additionally in high-temperature transient events kinetic effects can cause non-local transport[130]. Another major piece of physics which is often not included in SOL modelling is the effects of neutral atoms and molecules. SOLPS includes them through the coupling to the kinetic neutral model EIRENE[128], but SOLPS is a transport code, not a turbulence code. The only turbulence code EIRENE been coupled to so far is TOKAM3X[131], but so far it has only been used to examine the effect of turbulence on the transport of neutral particles[132], rather than vice versa. Simulations with simplistic fluid models of neutrals have been performed[133], especially in 1D studies of detachment[134].

2.4.3 Single-filament modelling

A considerable amount of theoretical work has focused on modelling the properties and propagation of individual filamentary structures. Here we give the most important ideas and results, but a very thorough overview can be found in [135].

Physical model of filament motion

The radial motion of the filaments can be explained using a simplified analytical model in terms of currents in the SOL. The following arguments are originally due to Krashenikov[136], but we follow the method of Omotani[137].

We model the SOL as a magnetized fluid, and a filament as a pressure perturbation in this fluid, uniform along the magnetic field lines. (The underlying fluid equations are described

in much more detail in chapter 3.) Radial pressure gradients across the filament cause the electron fluid to acquire a diamagnetic drift velocity[42]

$$\mathbf{v}_{\text{dia}} = -\frac{\mathbf{b} \times \nabla p_e}{en_e B}, \quad (2.8)$$

and an associated diamagnetic current $\mathbf{j}_{\text{dia}} = -en_e \mathbf{v}_{\text{dia}}$. (Here \mathbf{b} is the normalised magnetic field vector, defined as $\mathbf{b} = \mathbf{B}/B$.) The shape of this initial pressure perturbation is maintained by the the Lorentz force $\mathbf{j}_{\text{dia}} \times \mathbf{B}$ balancing the pressure gradient force $-\nabla p$. However, the radial variation in the strength of the \mathbf{B} -field in a tokamak means that the diamagnetic current generated on the high-field side of the filament is different to that on the low-field side. This asymmetry, which is depicted in figure 20, creates an overall effective diamagnetic

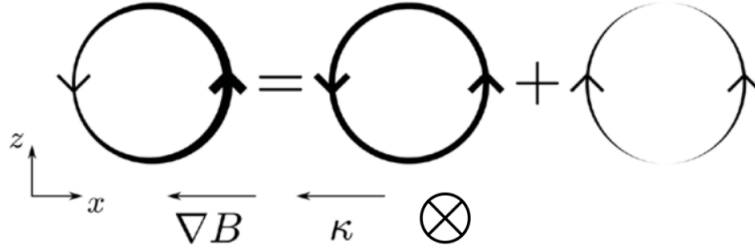


Figure 20: The diamagnetic current around a filament can be split into a divergence-free part (centre) and the unbalanced part (right). Here the magnetic field is directed out of the page. Figure from [137].

current source vertically around the cross-section of the filament.

The plasma fluid is assumed to be quasineutral, so the diamagnetic current must be closed through some other current path. Charged particles can move rapidly along the direction of the magnetic field, so parallel currents along the lengths of the filament can flow. These parallel currents flow until they reach the target plates, at which point they close through the Debye sheath, whose resistivity limits the size of the parallel current.

As well as parallel currents then perpendicular polarization currents can flow along the binormal direction in the drift-plane. These currents stem from polarization drifts, which are associated with the inertia of a massive charged particle subject to an acceleration by a time-varying electric field. The dependence on mass means this drift is different for ions and electrons, and so these currents polarize the plasma, creating a dipolar electric field across the filament (pictured in figure 22).

While the polarization current is flowing (so the \mathbf{E} -field is growing), then there is a $\mathbf{J}_{\text{pol}} \times \mathbf{B}$ force in the radial direction, which accelerates the filament outwards towards the wall. Once

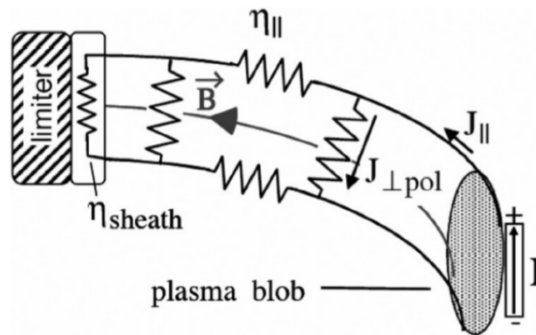


Figure 21: Diagram of the current paths within a filament. The diamagnetic current generated by the localised pressure gradient acts as a current source, which then must be closed either by parallel current through the target or polarization current across the face of the filament. Figure from [138].

the polarization current has set up a significant electric field, the filament as a whole is also subject to a significant $\mathbf{E} \times \mathbf{B}$ drift in the radial direction.

The proportion of current which is closed through the parallel or perpendicular path is determined by the effective sheath resistivity and the bulk plasma resistivity. If the majority of the diamagnetic current is closed by flowing down to the sheath then the filament is said to be in the “sheath-limited” regime, whereas if the majority of current is closed by polarization current the filament is said to be in the “inertial” regime.

As the diamagnetic currents are driven by pressure gradients, then regions of higher density (i.e. filaments) are preferentially driven outwards through the polarization current mechanism.

Dynamics of isolated filaments

Filaments are highly non-linear phenomena which can display a range of behaviours depending on their initial properties. The scaling of the velocity of individual filaments with parameters such as their spatial extent and amplitude of the density perturbation have been investigated both computationally and analytically. It was found that in the absence of sheath dissipation (so in the *inertial limit*, where polarization current balances diamagnetic current) the velocity scaled with the square root of the size of the filament in the drift-plane[139] (δ_{\perp} - conventionally defined as the full-width at half-maximum of a Gaussian fit to the pressure perturbation of the filament).

Analytical velocity scaling laws as a function of perpendicular filament size have been de-

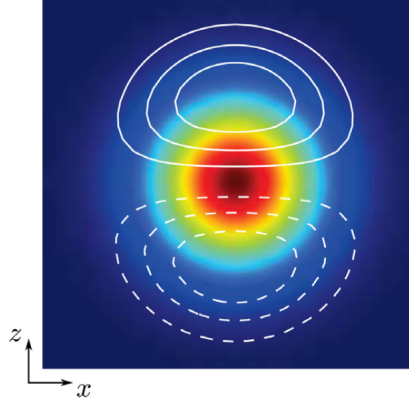


Figure 22: Plot of the dipolar electrostatic potential and the density within the drift-plane of a cylindrical filament. The white contours are equipotentials and the colours denote fluid density. Figure from [137].

rived[140, 141]. These analytical relations depict a filament through a two-dimensional model, and use quasineutrality to arrive at a vorticity equation (see sections 3.3.2 and 3.7) of the form

$$\frac{m_i}{B} \left(\frac{\partial}{\partial t} + \mathbf{v}_E \cdot \nabla \right) \frac{\nabla_{\perp}^2 \varphi}{B} = \frac{ec_s}{L_{\parallel}} \frac{e\varphi}{T_e} - \frac{eg}{n\Omega_i} \frac{\partial n_e}{\partial y}, \quad (2.9)$$

where m_i is ion mass, B is magnetic field strength, φ is electrostatic potential, c_s is plasma sound speed, L_{\parallel} is connection length to the target from the mid-plane, n is particle number density, Ω_i is ion gyrofrequency, and y denotes the binormal direction (perpendicular to both the radial direction and the direction parallel to the magnetic field). If a monopole pressure perturbation (and accompanying dipole potential perturbation) is assumed, the magnitude of the quantities in (2.9) can be estimated[140], including introducing the filament velocity v_{\perp} by estimating that fluctuations in potential $\bar{\varphi} \sim Bv_{\perp}\delta_{\perp}$. Balancing the terms in equation (2.9) in a steady state then leads to the velocity scaling expressions in different regimes as

$$v_{\perp}(\delta_{\perp}) \propto \begin{cases} c_s \sqrt{\delta_{\perp}} & \text{if } \delta_{\perp} \ll \delta_* \\ c_s \frac{1}{\delta_{\perp}^2} & \text{if } \delta_{\perp} \gg \delta_*, \end{cases} \quad (2.10)$$

where δ_* is a critical size given by

$$\delta_* = \rho_s \left(\frac{gl_{\parallel}^2}{2\rho_s c_s^2} \right)^{1/5},$$

where $g = 2c_s^2/R$ is an effective gravitational acceleration which captures the curvature drive (see section 3.4.1). These laws correspond respectively to the *inertial regime*, where diamagnetic current is closed predominantly through the polarization current, and to the

sheath-limited regime, where the current is closed through parallel currents to the sheath. It was shown that these predictions agreed with computational fluid simulations[142], and that the maximum filament velocity occurs for an intermediate filament size[143].

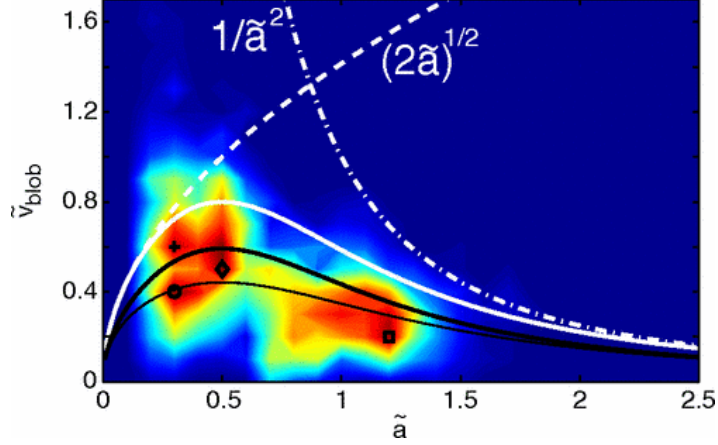


Figure 23: Normalised blob radial velocity \tilde{v}_{blob} plotted against normalised size \tilde{a} , both for experimental data obtained from TORPEX and analytical predictions. The dashed and dot-dashed white lines show the analytic scaling predicted for the inertial and sheath-limited regimes respectively. The solid lines are analytical predictions for no background density (white), order unity background (thick black), and neutral damping (thin black). Figure from [140].

Although the computational simulations agree well with the analytical theory, it has proved much harder to match these laws to experiment. [116] measured blob velocity in Alcator C-Mod, but found the data is not over a wide enough range to compare against scaling laws. The problem is that the laws only apply asymptotically in the limit of small or large δ_{\perp} , but small filaments are difficult to observe, and large filaments tend to be unstable, and at least in simulations they break up quickly into smaller blobs[144]. (In general filaments also cannot be arbitrarily large, else they would be larger than the SOL itself.) Some of the instabilities identified as important to filament lifetime were Kelvin-Helmholtz and drift-waves[144].

Theiler[140] obtained experimental data from TORPEX which appears to agree well with the predictions. In order to obtain data points for a wide range of normalized filament widths $\tilde{a} = \delta_{\perp}/a^*$, where

$$a^* = \left(\frac{4L^2}{\rho_s R} \right)^{1/5} \rho_s,$$

However in this study the gas used in the experiment was varied, so that \tilde{a} varied through its dependence on ρ_s and therefore m_i . This means that the variation in velocities seen could be due to a range of other effects caused by differing ion masses, such as differing resistivities,

rather than just being due to variation in filament size.

Myra[145] used NSTX data for a more transparent comparison, interpreting the analytical theory merely as providing upper and lower bounds on the possible velocities, and showing that this interpretation was borne out by the data.

In [144] systematic scans in initial amplitude, perpendicular size, and parallel extent were performed. The perpendicular size δ_{\perp} was found to have a strong effect not just on the filament radial velocity, but on the stability of the filament as a coherent structure. Smaller filaments were observed to undergo mushrooming motions, while larger filaments ejected thin finger-like structures which then themselves mushroomed.

The analytical scaling laws were extended to include filaments of elliptical cross-section[137], where they were previously only valid for filaments with a circular cross-section in the drift plane. The theoretical scaling with amplitude and ellipticity was also elucidated.

Including 3D dynamics allows for drift-wave instabilities, and if these grow on a similar timescale to the filament dynamics then the filaments perpendicular density gradient will be depleted, reducing the radial motion[141].

The drift-wave instability is also known as the “Universal” instability, because it can occur even in a uniform slab, only requiring a density gradient and not requiring any magnetic curvature. Drift-waves can have complex frequencies, so travel as well as grow. The mode only grows if there is some form of dissipation (e.g. resistivity), in which case there is a phase delay between potential and density fluctuations[146].

3D dynamics also allow the form of the parallel density to alter to match the potential (through Boltzmann’s relation), where the asymmetric potential then causes a “Boltzmann spinning” of the filament in the drift-plane[147].

Phenomena in the divertor region is not usually considered in these models, and so motivated by the expectation of lower electron temperatures, high neutral densities and possible detachment, the effect of enhancing the parallel resistivity in the last section of the parallel domain was investigated[148]. As expected, it was found that enhanced resistivity suppressed parallel currents, which increased polarization currents, which increased filament radial velocities. The motivation for this was a possible connection to “shoulder formation”, in which the exponential radial average profiles are broadened in the near-SOL[149].

The electron temperature dynamics (captured in equation (3.67)) are often omitted in computational studies, and a scan of various initial temperature perturbations with fixed pressure (and so correspondingly varying density) was performed[150]. It was found that for filaments with $\delta T/T_0 \gg \delta n/n_0$ then there is an increase in propagation in the bi-normal direction and

a decrease in propagation in the radial direction.

The effect of neutrals on the propagation of individual filaments has also been investigated, showing additional dependencies on background density through the plasma viscosity [151], as well as providing an earlier theorized driver for the radial motion of blobs[152].

Filament interactions and birth

A full description of the SOL must also clearly account for more than one filament at a time, which motivated simulations of multiple filaments interacting. Militello[153] investigated the assumption that filaments could be treated as independent theoretically, by performing 2D and 3D simulations in which the initial separation of two Gaussian filaments was varied, and the difference in radial propagation compared with the case that only one filament were present quantified. It was found that there is only a significant interaction if the filaments are initialised very close to one another, and from experimentally measured filament production rates it was deduced that filaments can be generally treated as independent entities once they have travelled out of the edge region and into the SOL.

The instabilities responsible for turbulence are generally caused by significant pressure gradients, so to actually simulate turbulence a background pressure gradient is imposed by using boundary conditions and spatially-varying source terms. Filaments are then born in this region of steep gradients, and propagate outwards into the flatter far SOL.

A range of linear instabilities are said to be capable of producing filaments, including the interchange, drift-wave, conducting-wall, resistive-ballooning or the cooperative elliptic instability[115, 154].

D’Ippolitto[115] describes filament formation as a process of long “streamers” being formed from instabilities, which are then cut off by velocity shear in the fluid. In this model a shearless fluid would produce long streamers, moderate shear would create filaments like those in L-mode, and strong shear would break up the filaments quickly and suppress transport, as in H-mode.

Manz[154] performed gyrofluid studies of the formation of plasma blobs, in which the location of filament birth was linked to the position of maximum radial electric field.

2.4.4 Linear Stability of the SOL

The onset of fully-developed turbulence is a multi-stage process. Conventionally the medium must display at least one form of linear instability, i.e. the linearised equations of motion have

eigenmodes whose amplitude grow exponentially with time.¹ Turbulence requires multiple simultaneously growing modes. In the linear regime, each mode evolves independently of the others; however once the amplitudes of the modes become large enough that they are no longer in the linear regime, the (previously-negligible) non-linear terms in the equations couple the different modes to one another. The non-linear interaction of two or more modes creates a new mode of a different frequency (a “three-wave coupling”). This process repeats, and a whole “cascade” of modes at different scales and frequencies is produced. Plasma turbulence is conventionally understood in terms of which linear instabilities contribute most strongly to its production (dictated by the growth rates of the different possible instabilities) and by the non-linearities which couple the modes together.²

Surprisingly little work has been done on the linear stability of the SOL. Work in the early 2000’s has most recently been updated by the work of Wilczynski[157]. Simplified models of the SOL can be treated like Rayleigh-Benard convection, using an analogy to two-dimensional thermal convection in neutral fluids[158, 159]. These treatments tended to assume that the plasma edge could be modelled using the conventional Rayleigh-Benard equations, but more recent work shows that this neglects a number of features which change the details of the linear stability properties. Instead Wilczynski treats a boundary value problem rather than a local problem, finding results similar to a thermal convection problem but with additional effects, such as additional advective terms and damping terms[160].

The presence of the separatrix creates a two-region problem analogous to neutral fluid two-layer convection. It has been suggested that Neoclassical theory implies that the core and the SOL have different values of various diffusion coefficients[161], including particle diffusion and viscosity (a complication we shall return to in chapter 6). Wilczynski[162] approaches this complexity by first treating the analogous neutral fluid problem of two-layer miscible convection[163], where they find that the ratio of the viscosities in the two layers, the ratio of the thermal diffusivities (analogous to particle diffusivities in the isothermal plasma problem), and the ratio of the depths of the two layers all affect the global structure of the most unstable mode. The fully linear stability analysis was then performed for the core-SOL system [164], finding that the ratios of particle diffusivity and ion viscosity are similarly important.

¹There is some work on so-called sub-critical turbulence, where turbulence is sustained through transiently growing modes without any modes being formally linearly unstable[155]

²This approach of balancing linear growth rates against damping to estimate steady-state amplitudes is called quasi-linear theory[156], and is much more commonly applicable to the core than to the SOL because the fluctuations are of much lower amplitude relative to the mean profiles. The lower amplitude means that the linearized equations used to calculate the approximation to the growth rates are more appropriate.

2.4.5 Drift-turbulence modelling

Full turbulence models of the SOL do not seed individual filaments, instead creating turbulence through gradients. The gradients are either fixed (in early models), or are themselves produced by driving the simulation with incoming fluxes or sources.

They also do not treat only the linear regime: whilst they may linearize certain terms for simplicity, they must at least solve a vorticity equation with a non-linear $\mathbf{E} \times \mathbf{B}$ advection term in order to reproduce the motion of blob-like structures.

LaBombard[123] provided a range of experimental evidence (in the form of scalings of various quantities with plasma parameters) for electromagnetic fluid drift turbulence being dominant in the edge of Alcator C-Mod. Scott[165, 166] used fluid simulations to show that in the regimes relevant to the plasma edge then either drift-Alfvén turbulence or electrostatic turbulence are likely to be dominant.

Turbulence simulations successfully generate blob-like structures, which can then be tracked and analysed in the same way that filamentary structures can be in experiments. Blob detection has been performed in 2D simulations with STORM[3] and in 3D simulations with GBS[167], in both cases showing broad agreement with the theoretical blob velocity scaling laws.

2.4.6 Model complexity

The host of possible approximations, geometric simplifications, and separate physical processes have led various research groups to try and increase model complexity gradually, rather than attempt to simulate as many processes as possible. Immediately capturing the menagerie of physics in the SOL using a single model has been tried, using a gyrokinetic particle-in-cell code[168, 169], but the extreme computational expense and inability to decouple plasma insights from the influence of the (poorly-understood) wall boundary conditions have so far limited the usefulness of this approach.

An early example of geometric simplification was Ribeiro[170] using gyrofluid simulations to show that turbulence on open and closed magnetic field lines (i.e. sheath boundary conditions or periodic boundary conditions in the parallel direction) differs significantly. Inside the LCFS drift-wave dynamics dominate, whereas outside the LCFS the interchange instability (magnetic buoyancy) is dominant. Ribeiro also investigated the effect of varying the poloidal position of the limiter[171], and found that in all cases there was a fairly sharp transition between drift-wave ion temperature gradient turbulence in the edge and interchange turbu-

lence in the SOL, but that the poloidal position of the limiter affected the interaction of the turbulence with the background.

Studies using the GBS code[172] have steadily increased in complexity over time. An early use for the code was in linear devices [173], and also for modelling the toroidal geometry of TORPEX (which has no rotational transform[174]. GBS was later used for modelling the C-mod SOL in inner-wall limited discharges[175], as well as some modelling incorporating a core as well as the SOL[172].

Other codes started simpler, beginning with 2D models which approximate the parallel physics (as described in chapter 3). The TOKAM3X code[176] evolved from the much earlier TOKAM2D code[177], but became capable of 3D global turbulence simulations with X-point geometry[178].

The STORM code followed a similar path, being inspired by earlier work using the 2D code ESEL[179]. STORM (both STORM2D and STORM3D) were originally developed for isolated filament simulations. The 2D closures usually involve either the *sheath dissipation closure*, which neglects parallel gradients (i.e. assumes uniformity along the field line up to the target), or the *vorticity advection closure*, which neglects parallel currents into the target. These two 2D closures were compared against full 3D simulations for the case of isolated isothermal filaments by Easy[144], and it was found that the sheath dissipation closure more accurately replicated the 3D dynamics.

The isothermal assumption was relaxed by Walkden, adding an electron temperature equation to STORM and analysing the differences against isolated filaments[150]. Hoare similarly added electromagnetic effects and quantified their influence on filaments[6]. STORM graduated to saturated turbulence simulations during the study of this thesis, but was first published as divertor box simulations by Walkden[5]. Riva[133] ran full 3D MAST-U geometry simulations with STORM, skipping past rectangular slab models.

2.5 Summary

Several key and consistent results have emerged from edge and SOL turbulence modelling. In particular, the basic character of the turbulence as interchange-driven but then predominantly sustained through electrostatic drift-waves[180], the presence of a flow shear layer near the edge, in which filaments are produced[87], and some of the mechanisms for setting the gradients and heat flux widths in the SOL[181].

There are also many serious challenges in modelling the SOL. The very universality of the

turbulence properties makes testing models very difficult, because obtaining agreement with experiment is a necessary but not sufficient condition for correctly explaining results. The complexity of the models, and number of nonlinearly interacting effects, also means that it is hard to use any disagreements which are found to guide improvements in the model. There is a wide range of regimes to be understood (e.g. L-mode, H-mode, attached, detached, kinetic, fluid, different divertor geometries, different wall materials), relevant for different machines, many of which can change the simulation requirements considerably. Including the extra physics necessary to resolve important processes (in particular resolving turbulent transport, kinetic parallel transport, and kinetic neutrals) pushes the computational cost high enough that only a few simulations can be feasibly performed[169]. The ultimate aim of studying the SOL is to be able to predict heat loads and plasma performance for a future fusion reactor, but as in other areas of fusion science, there is a difficult problem of predicting behaviour in regimes for which we have little or no experimental evidence. The SOL is not an isolated system, it is coupled on both sides to complex systems (the edge/pedestal/core and the plasma-surface interactions), each of which require their own study and modelling, yet can affect the SOL behaviour considerably

Some particular unresolved issues of relevance to this thesis include how much can the SOL geometry be simplified before it is unable to reproduce key experimental features, how can the SOL be most simply coupled to the core, and to what extent is the parallel (non-turbulent) transport separable from the radial turbulent transport in modelling?

Chapter 3

Physical Model

3.1 Introduction

In this chapter we motivate and derive the simplified model used in the rest of this thesis. The Braginskii equations are used as a starting point, with their features and regime of validity described. We then apply the drift ordering to derive a set of drift-reduced fluid equations. The STORM model is described as a further approximation of this drift-reduced system, and the actual system of equations solved by the STORM code (see chapter 4) is given, presented in the Bohm-normalised form which will be used later on. The full derivation of this particular system of non-isothermal equations has not been described in the open literature before, but is adapted from the treatment in the (as-yet unpublished) book by Militello[45]. Boundary conditions for the sheath at the target plates are described, as well as the slab-like flux tube geometry in which they are applied. Finally the approximate closures describing the parallel physics used in the 2D version of the STORM model are derived.

3.2 Braginskii Fluid Equations

The standard plasma fluid transport equations derived by Braginskii[182] are

$$\frac{\partial n_\alpha}{\partial t} + \nabla \cdot (n_\alpha \mathbf{u}_\alpha) = S^{(n)} \quad (3.1)$$

$$m_\alpha n_\alpha \frac{d\mathbf{u}_\alpha}{dt} = -\nabla p_\alpha - \nabla \cdot \mathbf{\Pi}_\alpha + e_\alpha n_\alpha (\mathbf{E} + \mathbf{u}_\alpha \times \mathbf{B}) + \mathbf{R}_\alpha + \mathbf{S}_\alpha^{(n)} \quad (3.2)$$

$$\frac{3}{2} n_\alpha \frac{dT_\alpha}{dt} + p_\alpha \nabla \cdot \mathbf{u}_\alpha = -\nabla \cdot \mathbf{q}_\alpha - \mathbf{\Pi}_\alpha : \nabla \mathbf{u}_\alpha + Q_\alpha + W_\alpha \quad (3.3)$$

where α labels the species of charged particles, either ions or electrons, n is number density, \mathbf{u} velocity, m particle mass, e particle charge, p pressure, T temperature, $\mathbf{\Pi}$ the viscous stress tensor, $:$ the tensor inner product, Q frictional interspecies heating, and $S^{(n)}$, $\mathbf{S}^{(n)}$, and W are local density, momentum and energy sources respectively. The total derivative includes advection by the velocity of that particular species

$$\frac{d_\alpha}{dt} \equiv \frac{\partial}{\partial t} + \mathbf{u}_\alpha \cdot \nabla. \quad (3.4)$$

These equations are derived by taking successive velocity moments of the kinetic Boltzmann equation [182], but as the equation for each moment depends on the previous order moment, at some point the hierarchy must be closed. Braginskii chose to stop at the 4th moment, the heat flux \mathbf{q} , and derived the “transport coefficients” for the electron and ion heat flux for example in the limit $\omega_e \tau_{c,e} \gg 1$. (Here ω_e is the electron gyrofrequency and $\tau_{c,e}$ is the mean electron-electron collision timescale - see equations (3.27) - (3.32).) Braginskii found these transport coefficients to be

$$\mathbf{q}_e = -\kappa_{\parallel,e} \nabla_{\parallel} T_e - \kappa_{\perp,e} \nabla_{\perp} T_e - \kappa_{\times,e} \mathbf{b} \times \nabla_{\perp} T_e \quad (3.5)$$

$$- 0.71 n_e \nabla_{\parallel} T_e (\mathbf{u}_{\parallel,i} - \mathbf{u}_{\parallel,e}) - \frac{3}{2} \frac{n_e T_e}{\nu_{ei} \Omega_e} \mathbf{b} \times (\mathbf{u}_i - \mathbf{u}_e)$$

$$\mathbf{q}_i = -\kappa_{\parallel,i} \nabla_{\parallel} T_i - \kappa_{\perp,i} \nabla_{\perp} T_i - \kappa_{\times,i} \mathbf{b} \times \nabla_{\perp} T_i, \quad (3.6)$$

where κ are various thermal conductivity coefficients, whose values were derived by Braginskii¹.

Similar closure relations are derived for the momentum transfer from electron-ion friction, giving

$$\mathbf{R}_e = -\mathbf{R}_i = \mathbf{R}_u + \mathbf{R}_T, \quad (3.10)$$

¹The thermal conductivity coefficients are given by

$$\kappa_{\parallel,\alpha} = \frac{d_{\parallel,\alpha} \mu_{\parallel,\alpha}}{c_{\parallel,\alpha} m_\alpha} \quad (3.7)$$

$$\kappa_{\perp,\alpha} = \frac{d_{\perp,\alpha} \mu_{\perp,\alpha}}{c_{\perp,\alpha} m_\alpha} \quad (3.8)$$

$$\kappa_{\times,\alpha} = \frac{d_{\times,\alpha} \mu_{\times,\alpha}}{c_{\times,\alpha} m_\alpha}, \quad (3.9)$$

where $d_{\parallel,e} = 3.2$, $d_{\parallel,i} = 3.9$, $d_{\perp,e} = 4.7$, $d_{\perp,i} = 2$, $d_{\times,e} = d_{\times,i} = 2.5$, and see footnote 2 for the definitions of the dynamic viscosity coefficients μ , equations (3.19) - (3.21), and their corresponding coefficients c .

Some key features of these relations are that electron motion dominates parallel heat transport, since $\kappa_{\parallel,e}/\kappa_{\parallel,i} \sim \sqrt{m_i/m_e}$, but ion motion dominates perpendicular heat transport, since $\kappa_{\perp,e}/\kappa_{\perp,i} \sim \sqrt{m_e/m_i}$. We can also see that (via the viscosity expressions (3.19) - (3.21)) the perpendicular heat transport is much smaller than the parallel heat transport, but this is to be expected if the tokamak is to do its job of confining the heat of the plasma.

where

$$\mathbf{R}_u = en \left(\frac{\mathbf{J}_{\parallel}}{\sigma_{\parallel}} + \frac{\mathbf{J}_{\perp}}{\sigma_{\perp}} \right), \quad (3.11)$$

$$\mathbf{R}_T = -0.71n_e \nabla_{\parallel} T_e - \frac{3}{2} \frac{n_e}{\nu_{ei} \Omega_e} \mathbf{b} \times \nabla_{\perp} T_e, \quad (3.12)$$

Here σ_{\perp} and σ_{\parallel} are the perpendicular and parallel components of the plasma conductivity σ (defined through $\mathbf{J} = \sigma \mathbf{E}$, and technically a tensor in general, though Braginskii ignores off-diagonal terms here)

$$\sigma_{\perp} = \frac{n_e e^2 \nu_{ei}}{m_e} \quad \sigma_{\parallel} = 1.96 \frac{n_e e^2 \nu_{ei}}{m_e}. \quad (3.13)$$

The viscous stress tensor $\mathbf{\Pi}_{\alpha}$ has a complicated form² but we will neglect many of the details later anyway.

² The viscous stress tensor $\mathbf{\Pi}_{\alpha}$ derived by Braginskii[182] has a full form which can be described as three parts

$$\mathbf{\Pi}_{\alpha} = \mathbf{\Pi}_{\alpha,\parallel} + \mathbf{\Pi}_{\alpha,\perp} + \mathbf{\Pi}_{\alpha,\times}, \quad (3.14)$$

where \parallel , \perp , and \times represent different the parallel, perpendicular, and binormal components relative to the magnetic field. The full expressions are given by

$$\mathbf{\Pi}_{\parallel,\alpha} = -\mu_{\parallel,\alpha} \begin{bmatrix} \frac{1}{2}(W_{xx} + W_{yy}) & 0 & 0 \\ 0 & \frac{1}{2}(W_{xx} + W_{yy}) & 0 \\ 0 & 0 & W_{zz} \end{bmatrix}, \quad (3.15)$$

$$\mathbf{\Pi}_{\perp,\alpha} = -\mu_{\perp,\alpha} \begin{bmatrix} \frac{1}{2}(W_{xx} - W_{yy}) & W_{xy} & 4W_{xz} \\ W_{xy} & \frac{1}{2}(W_{yy} - W_{xx}) & 4W_{yz} \\ 4W_{xz} & 4W_{yz} & 0 \end{bmatrix}, \quad (3.16)$$

$$\mathbf{\Pi}_{\times,\alpha} = -\mu_{\times,\alpha} \begin{bmatrix} W_{xy} & -\frac{1}{2}(W_{xx} - W_{yy}) & 2W_{yz} \\ -\frac{1}{2}(W_{xx} - W_{yy}) & -W_{xy} & -2W_{xz} \\ 2W_{yz} & -2W_{xz} & 0 \end{bmatrix}, \quad (3.17)$$

where W_{ij} are the components of the rate of strain tensor

$$\mathcal{W} = \nabla \mathbf{v} + (\nabla \mathbf{v})^T - \frac{2}{3} (\nabla \cdot \mathbf{v}) \mathcal{I}, \quad (3.18)$$

and the μ_{α} 's are the dynamic viscosity coefficients, given by

$$\mu_{\parallel,\alpha} = c_{\parallel,\alpha} m_{\alpha} n_{\alpha} \rho_{\alpha} \nu_{th,\alpha} (\tau_{c,\alpha} \Omega_{\alpha}), \quad (3.19)$$

$$\mu_{\perp,\alpha} = c_{\perp,\alpha} m_{\alpha} n_{\alpha} \rho_{\alpha} \nu_{th,\alpha} (\tau_{c,\alpha} \Omega_{\alpha})^{-1}, \quad (3.20)$$

$$\mu_{\times,\alpha} = c_{\times,\alpha} m_{\alpha} n_{\alpha} \rho_{\alpha} \nu_{th,\alpha}, \quad (3.21)$$

where $c_{\parallel,e} = 0.73$, $c_{\parallel,i} = 0.96$, $c_{\perp,e} = 0.51$, $c_{\perp,i} = 0.3$, $c_{\times,e} = -0.5$, $c_{\times,i} = 0.5$.

Finally closure relations for heating from electron-ion collisions are derived as

$$Q_i = 3 \frac{m_e n_e (T_e - T_i)}{m_i \nu_{ei}} \quad (3.22)$$

$$Q_e = -Q_i + \frac{\mathbf{J} \cdot \mathbf{R}_e}{n_e e}. \quad (3.23)$$

In these expressions ν_{ei} is the electron-ion collision rate, which will be given later in (3.24). The various κ are directionally-dependent coefficients with values given in [182].

Whilst these equations have many strong similarities to versions of the conventional Navier-Stokes equations used to describe fluid equations, both their microscopic motivation and their resulting behaviour are significantly different. While particles in neutral fluids on average travel a mean free distance between near-instantaneous collisions occurring at well-defined times, particles in a plasma are technically always interacting through long-range Coulomb forces. However, a scale-splitting is still possible through a treatment of close-range Coulomb collisions and the longer-range Debye shielding. This leads to a set of fluid equations with similar properties, but which are only valid under a wider set of assumptions about length and time scales of interest, and rates of collisional interactions. As we will discuss, in a strongly-magnetized regime the electromagnetic force terms dominate the motion of the fluid in the plane perpendicular to the magnetic field, whilst along the magnetic field the plasma behaves instead like a charged fluid. This broadly splits the dynamics into those parallel to the magnetic field and those perpendicular to it. The electric field term leads to the cycloidal drift motions described in chapter 1, whose directions are primarily governed by fluctuations in the electrostatic potential.

The use of the Braginskii equations here already implies certain assumptions about the system being modelled. In particular it assumes a specific ordering - that is the length and time scales of the fluctuations of interest (as well as some other relevant quantities in the plasma) fall within a certain range.

Hydrogenic species assumption

Whilst the general Braginskii equations (3.1) - (3.3) are valid for multiple interacting species, the closure relations (3.5) - (3.13) were derived for a hydrogenic plasma (which is a so-called “simple plasma” because it only has one ion species, and that species has a positive charge Z), consisting only of an equal mix of fully ionised hydrogen atoms and their corresponding electrons.³ We have not specified m_i - therefore these equations can still represent a protium,

³There are more complex closures for multi-species plasmas, such as Zhdanov[183, 184], but these are well outside the scope of this thesis.

deuterium, or tritium plasma (though not the multiple ion species of a D-T mixture).

As electrons are ~ 1800 times lighter than protons, then in any hydrogenic plasma we can safely assume that the electron-to-ion mass ratio m_e/m_i is very small, which is later used to neglect some terms in the equations.

The hydrogenic assumption also allows for a first-principles calculation of the collision frequencies, giving

$$\nu_{ei} = \frac{n_e Z_i^2 e^4 \ln \Lambda}{3\epsilon_0^2 m_e^{1/2} (2\pi T_e)^{3/2}} \quad (3.24)$$

$$\nu_{ii} = \frac{n_e Z_i^2 e^4 \ln \Lambda}{3\epsilon_0^2 m_i^{1/2} (\pi T_i)^{3/2}}, \quad (3.25)$$

where $\nu_{\alpha\beta}$ the average rate of collisions between particles of species α and β . Here the *Coulomb logarithm* is approximately [185]

$$\ln \Lambda \approx 18.0 - \ln \left[\left(\frac{n_e}{10^{19}} \right)^{1/2} \left(\frac{T_e}{10^3 e} \right)^{-3/2} \right]. \quad (3.26)$$

Λ is the *plasma parameter*, a measure of to what degree plasma particles interact primarily through long-distance collective electrostatic effects (such as through a smoothly-varying \mathbf{E} -field) rather than through short-range binary collisions. The Braginskii model assumes that $\Lambda \gg 1$ (a “weakly-coupled” plasma), a requirement that is comfortably satisfied in fusion plasmas in general, as they are relatively sparse and hot.

Strongly magnetized plasma assumption

Specific to magnetized plasmas is the influence of a strong magnetic field. In the absence of collisions, the charged particles gyrate around the field lines with frequency $\Omega_\alpha = eB/m_\alpha$ and radius $\rho_\alpha = v_{\text{th},\alpha}/\Omega_\alpha$, where the thermal velocity is given by $v_{\text{th},\alpha} = \sqrt{T_\alpha/m_\alpha}$. When the magnetic field strength is high enough that particles complete many gyro-orbits between collisions on average, we say that the plasma is *strongly magnetized*. The Braginskii model is valid only in the strongly magnetized limit, which introduces a set of length and time scale requirements:

$$\begin{aligned} \nu_{ei} &\ll \Omega_e, & \nu_{ii} &\ll \Omega_i, \\ l_\perp &\gg \rho_e, & l_\perp &\gg \rho_i, \end{aligned} \quad (3.27)$$

where l_\parallel and l_\perp the smallest length scales of interest. ($l_\perp \gg \rho_e$ is always redundant though because $\rho_e \ll \rho_i$.) These inequalities mean that we can only use the Braginskii equations to model systems larger than the Larmor radius, and that the collisionality cannot be too high, else the particles would be kicked off their gyro-orbits too rapidly.

We will need to quantify the degree of magnetization so that we can use it to order terms later, through the magnetization parameter δ

$$\delta \equiv \frac{\rho}{l_{\perp}}. \quad (3.28)$$

We can also equivalently express magnetization in terms of timescales:

$$\delta = \frac{\omega_t}{\Omega}, \quad (3.29)$$

which we arrived at by defining the transit frequency ω_t as

$$\omega_t \equiv \frac{v_{th}}{l_{\perp}}, \quad (3.30)$$

the rate at which particles moving at thermal speeds traverse the system. The thermal speed, gyroradius, and magnetization parameter do all differ between species, because of their different masses.

The difference in mass between ions and electrons means that $v_{th,i}$, ρ_e , and δ_e are all a factor $\sqrt{m_e/m_i}$ smaller than their oppositely-charged counterparts. In a fully magnetized plasma both species are magnetized, and as $\delta_e \ll \delta_i$, we therefore require $\delta_i \ll 1$.

Collisional ordering assumption

The moment hierarchy procedure which leads to the fluid equations assumes that the distribution of particle velocities is close to Maxwellian.⁴ This makes the model unsuitable for phenomena involving a significant deviation from a Maxwellian, such as in the presence of strong heating of one part of the distribution function (for example from neutral beam injection). For the system to be well-approximated by a Maxwellian the timescale of relaxation back towards a Maxwellian must be faster than the characteristic time scale of the problem, and the distance over which a Maxwellian is established on average be smaller than the characteristic time scale of the problem, i.e. the system must be relatively *collisional*:

$$\begin{aligned} \omega_c \ll \nu_{ei}, \quad \omega_c \ll \nu_{ii}, \\ l_{\parallel} \gg \lambda_e, \quad l_{\perp} \gg \rho_i, \end{aligned} \quad (3.31)$$

⁴It doesn't technically assume that it is exactly a Maxwellian - instead the velocity distribution is assumed to be close enough that it can be well approximated by a Maxwellian plus a perturbed part, where the perturbed part is small enough that it can be expressed linearly in terms of the state variables n , \mathbf{u} , and T and their derivatives. This is what allows for the closure relations to express the quantities $\mathbf{\Pi}$, \mathbf{q} , \mathbf{R} , Q in terms of derivatives of n , \mathbf{u} and T - these fluxes in configuration space are low-order representations of the deviation of the local velocity distribution away from a true Maxwellian. The details of this are given in [182].

where ω_c is the characteristic frequency of the fastest fluctuations of interest in the system, and λ_α the mean free path of species α between collisions. The mean free path is defined in terms of the thermal velocity as $\lambda_\alpha = v_{\text{th},\alpha}/\nu_{\alpha\beta}$.

The requirement that $l_\parallel \gg \lambda_e$ is not always satisfied in the SOL: high-power machines are projected to be rather collisionless (as they have hotter particles in the SOL for a similar size machine), and will require kinetic codes (such as [129]) to correctly model parallel electron heat transport. This is only a problem for the upstream SOL and pedestal however - the cold, dense divertor region will always have high collisionality.

The magnetized ordering in (3.27) and the collisional ordering in (3.31) combine to bound the collisionality from both above and below: if the collisionality is too high then particles will not stay on their gyro-orbits for long, but if collisions are too slow then the distribution function will not equilibrate to a Maxwellian before the system's fluid variables evolve further. These constraints are combined in (3.34).

In practice for this thesis the primary constraints of the Braginskii model are on the smallest length and time scales it can resolve (l_\perp , l_\parallel , and τ). We now have all the expressions required to calculate these: for a typical MAST-relevant deuterium SOL plasma with $n_e = 0.5 \times 10^{13} \text{m}^{-3}$, $T_e = 15 \text{eV}$, $T_i = 30 \text{eV}$, $B = 0.24 \text{T}$, $m_i = 2m_p$, we have

$$l_\perp \gg \rho_i \sim 3 \text{mm}, \quad (3.32)$$

$$l_\parallel \gg \lambda_e \sim 0.5 \text{m}, \quad (3.33)$$

$$\tau \gg \tau_c \gg \Omega_i^{-1} \sim 0.1 \mu\text{s}. \quad (3.34)$$

3.3 Drift Reduction

The Braginskii model is still very general, and we need to take a more specific ordering in order to make the problem tractable. The ordering suitable for SOL transport problems is the ‘‘drift-ordering’’, a description of which we will now give by following the argument of [157].

Technically overall we will be invoking three different small ordering parameters to approximate terms: the plasma beta

$$\beta \equiv \frac{8\pi(p_i + p_e)}{B^2} \ll 1, \quad (3.35)$$

the magnetization parameter δ (the same as in (3.28))

$$\delta \equiv \frac{\rho}{l_\perp} \ll 1, \quad (3.36)$$

and the collision parameter

$$\Delta \equiv \frac{\lambda_{\parallel}}{l_{\parallel}} \ll 1, \quad (3.37)$$

where λ_{\parallel} is the mean free path between collisions in the parallel direction. (For more details see the original source of this derivation by Simakov and Catto [186].)

3.3.1 Drift-ordering

Ordering by gyrofrequency

Take the Braginskii momentum equation (3.2), suppressing species notation:

$$mn \left(\frac{\partial}{\partial t} + \mathbf{u} \cdot \nabla \right) \mathbf{u} = -\nabla p - \nabla \cdot \mathbf{\Pi} + en(\mathbf{E} + \mathbf{u} \times \mathbf{B}) + \mathbf{R}. \quad (3.38)$$

As an equation for the evolution of momentum, each term has units of momentum multiplied by some kind of associated frequency. Acceleration happens at the characteristic frequency of the process we chose to study, $\frac{d}{dt} \sim \omega_c$. Pressure forces can only act as fast as the particles transmitting them, so the pressure gradient term and the viscous stress terms have frequencies of the time it takes for a particle to transit over a length scale of interest, $\omega_t = v_{\text{th}}/l_{\perp}$. When normalised the magnetic force term scales with the gyrofrequency Ω , and the frictional term is due to collisions which occur with a frequency ν . The frequency of the electric field term depends only on how quickly that electric field fluctuates, but so far we have no way of knowing how fast or slow that is relative to the other terms.

If we take the cross product of (3.38) with the unit vector in the direction of the magnetic field, \mathbf{b} , we obtain an expression for the perpendicular part of the fluid velocity

$$\mathbf{u}_{\perp} = \mathbf{u}_E + \frac{1}{mn\Omega} \mathbf{b} \times \left(mn \frac{d\mathbf{u}}{dt} + \nabla p + \nabla \cdot \mathbf{\Pi} - \mathbf{R} \right), \quad (3.39)$$

where $\mathbf{u}_E = (\mathbf{E} \times \mathbf{B})/B^2$ is the $\mathbf{E} \times \mathbf{B}$, or electric, drift velocity. Equation (3.39) shows that \mathbf{u}_E is special - it is the only drift velocity not pre-multiplied by the inverse gyrofrequency $1/\Omega$. This matters for ordering the terms: we are in the strongly-magnetized limit, so have assumed that the gyrofrequency is much larger than the other frequencies in the system (eq. (3.27)). With Ω large, $1/\Omega$ acts like the small magnetization parameter δ , so $\mathbf{u}_{\perp} = \mathbf{u}_E + \delta(\dots) = \mathbf{u}_E + \mathcal{O}(\delta)$. This means as a drift-generating force the \mathbf{E} -field is special, its size is not dictacted by δ , so we get to decide how big it is depending on the problem we want to study.

MHD vs drift-reduced orderings

There are two main choices of ordering for magnetised plasma dynamics: magnetohydrodynamic (MHD) and drift ordering. They both make the same assumptions about magnetisation described above, but differ in the relative strength of the transverse electric field that is assumed.

In MHD the \mathbf{E} -field is assumed large, so that the perpendicular $\mathbf{E} \times \mathbf{B}$ flow speed is comparable to the thermal speed, i.e. the electric field can move plasma across the magnetic field lines at a speed

$$\mathbf{u}_E \sim \frac{E_\perp}{B} \sim v_t. \quad (3.40)$$

MHD is therefore intended to model the fastest, most violent motions a quasi-neutral magnetised plasma is capable of, which is important because stability on short timescales is a prerequisite to any consideration of slower-scale transport.

The drift ordering, on the other hand, assumes that the transverse electric fields are smaller, such that transverse electric forces are comparable to pressure forces (and potentially also to the other forces like resistive force). Specifically

$$\mathbf{u}_E \sim \frac{E_\perp}{B} \sim \delta v_t, \quad (3.41)$$

so the drift ordering has perpendicular $\mathbf{E} \times \mathbf{B}$ velocities a factor δ smaller than thermal speeds. This reflects gyrodrift velocities (see figure 3 in chapter 1) that are slow enough to not majorly distort the circular gyromotion, as in the magnetized limit of $\delta \gg 1$ the particles rapidly complete many gyro-orbits before the gyrocentre has drifted very far.

Restricting the size of all perpendicular \mathbf{E} -fields also restricts the allowed speed of fluctuations, through Faraday's law:

$$\begin{aligned} \nabla \times \mathbf{E} &= -\frac{\partial \mathbf{B}}{\partial t} \\ \frac{E}{l_\perp} &\sim \frac{dB}{dt} \\ \frac{d}{dt} &\sim \frac{1}{l_\perp} \frac{E}{B} \sim \frac{1}{l_\perp} \delta v_{th} \sim \delta \omega_t \sim \delta^2 \Omega. \end{aligned} \quad (3.42)$$

The effect of fluctuations on the magnetic field is also limited ($\mathbf{E}_\perp = -\nabla\phi[1 + \mathcal{O}(\delta)]$ [187]), meaning that fluid motions do not disturb B_\parallel , though they do still affect B_\perp . Whilst the system is not (yet) entirely electrostatic, this has largely removed the feedback of changes in B on the other fluid variables, so we can imagine that fluctuations now occur on an effectively-constant background field that is MHD-stable.⁵

⁵There is a sense in which worrying about an ordering that is orders of magnitude slower than MHD is a

We now seek to apply this ordering to the Braginskii equations (3.1) - (3.13). Expanding (3.39) (and re-introducing species labels) shows each of the different drift velocities that make up total velocity in the perpendicular plane.

$$\mathbf{u}_{\alpha,\perp} = \underbrace{\frac{\mathbf{E} \times \mathbf{B}}{B^2}}_{\mathbf{u}_E} - \underbrace{\frac{\nabla p_\alpha \times \mathbf{B}}{e_\alpha n_\alpha B^2}}_{\mathbf{u}_{\text{dia}}} - \underbrace{\frac{m_\alpha \frac{\partial \mathbf{u}_\alpha}{\partial t} \times \mathbf{B}}{e_\alpha B^2}}_{\mathbf{u}_{\text{pol}}} - \underbrace{\frac{\nabla \cdot \mathbf{\Pi}_\alpha \times \mathbf{B}}{e_\alpha n_\alpha B^2}}_{\mathbf{u}_{\text{vis}}} + \underbrace{\frac{\mathbf{R}_\alpha \times \mathbf{B}}{e_\alpha n_\alpha B^2}}_{\mathbf{u}_{\text{fri}}} \quad (3.43)$$

From left to right we have: the $\mathbf{E} \times \mathbf{B}$ drift \mathbf{u}_E , the diamagnetic drift \mathbf{u}_{dia} , the polarization drift \mathbf{u}_{pol} , the viscous drift \mathbf{u}_{vis} , and the collisional resistive drift \mathbf{u}_{fri} (due to friction between the species). We can use this expansion to derive an actual set of drift-reduced model equations.

3.3.2 Drift-fluid model

The construction of a drift-reduced fluid model is done by substituting the drift expansion (3.43) into the Braginskii equations, and simplifying further according to the drift ordering.

Dominant drift terms

We established in equation (3.41) that the $\mathbf{E} \times \mathbf{B}$ drift is $\mathcal{O}(\delta)$ compared to the thermal velocity. As in other fluids the ion thermal velocity $v_{th,i}$ and plasma sound speed c_s are similar - the latter is given by

$$c_s = \sqrt{\frac{T_e + T_i}{m_i}}, \quad (3.44)$$

which with $T_e \sim T_i$ (and m_e negligible) means $c_s = v_{th,i}$. The electron thermal velocity $v_{th,e}$ however is much larger than both. We therefore have

$$\mathbf{u}_E \sim \delta c_s. \quad (3.45)$$

With cold ions instead then $c_s \sim (1/\sqrt{2})v_{th,e}$, which is still a small factor compared to the δ ordering. The factors of 2 in these expressions are dependent on the exact definition of thermal velocity anyway however. The diamagnetic drift is also $\mathcal{O}(\delta)$:

$$\mathbf{u}_{\text{dia}} = -\frac{\nabla p_\alpha \times \mathbf{B}}{e_\alpha n_\alpha B^2} \sim \frac{\frac{1}{l_\perp} n T B}{e n B^2} \sim \frac{1}{l_\perp \Omega} \frac{T}{m} \sim \left(\frac{1}{l_\perp \Omega} \sqrt{\frac{T}{m}} \right) \left(\sqrt{\frac{T}{m}} \right) \sim \delta c_s. \quad (3.46)$$

The polarization drifts are ordered smaller - using (3.42) we have both ion and electron polarization drift $\mathcal{O}(\delta)$ compared to the sound speed:

$$\mathbf{u}_{\text{pol},i} = -\frac{m_i}{e_i B^2} \frac{\partial \mathbf{u}_\alpha}{\partial t} \times \mathbf{B} \sim \frac{m_i}{e_i B} (\delta^2 \Omega) (\delta c_s) \sim \delta^3 c_s, \quad (3.47)$$

mark of progress in plasma confinement physics. We assume a steady, unchanging MHD background, and are interested in modelling the slower transport on top of that, because we have (mostly, not entirely!) solved the problems of maintaining the necessary MHD stability in tokamaks.

$$\mathbf{u}_{\text{pol},e} \sim \frac{m_e}{m_i} \delta^3 c_s, \quad (3.48)$$

though the electron polarization drift is smaller by the mass ratio, so we immediately drop it. The leading part of the viscous stress tensor can be approximated by the velocity shear multiplied by a prefactor that depends on the component. Braginskii calculated these, and for the perpendicular component found a dependence of

$$\mathbf{\Pi}_\alpha \sim \left(\frac{p_\alpha}{\Omega_\alpha} \right) \nabla \mathbf{v}_{th,\alpha}, \quad (3.49)$$

which we can use to show that, similarly to the polarization terms, the viscous terms are also $\mathcal{O}(\delta^3)$

$$\mathbf{u}_{\text{vis},i} = -\frac{\nabla \cdot \mathbf{\Pi} \times \mathbf{B}}{e_i n B^2} \sim \frac{1}{e_i n_i B} \frac{1}{l_\perp} \frac{(nT)}{\Omega} \frac{(\delta c_s)}{l_\perp} \sim \left(\frac{1}{l_\perp \Omega} \sqrt{\frac{T}{m_i}} \right)^2 \delta c_s \sim \delta^3 c_s, \quad (3.50)$$

with the electron drift again smaller by the mass ratio:

$$\mathbf{u}_{\text{vis},e} \sim \frac{m_e}{m_i} \delta^3 c_s. \quad (3.51)$$

Taking the perpendicular component of \mathbf{R}_u from eq. (3.11), we can order the frictional resistive drift by assuming $\mathbf{J}_\perp \sim en\delta c_s$:

$$\mathbf{u}_{\text{fri}} = \frac{\mathbf{R}_\alpha \times \mathbf{B}}{e_\alpha n_\alpha B^2} \sim \frac{1}{enB} en \frac{(ne\delta c_s)}{\sigma_\perp} \sim \frac{\nu_{ei}}{\Omega} \delta c_s. \quad (3.52)$$

Strong magnetization implies that $\nu_{ei}/\Omega_i \sim \delta$, so the frictional drift is $\mathcal{O}(\delta^2)$.

Our ordering in terms of the small parameter δ has shown that the $\mathbf{E} \times \mathbf{B}$ and diamagnetic terms are at least a factor δ larger than the other perpendicular drifts. It is therefore useful to define the leading order component of the perpendicular drift velocity for a particular species as

$$\mathbf{u}_{\perp,0,\alpha} \equiv \mathbf{u}_E + \mathbf{u}_{\text{dia},\alpha}, \quad (3.53)$$

and the leading order component of the total velocity as

$$\mathbf{u}_{0,\alpha} \equiv \mathbf{u}_{\perp,0} + \mathbf{u}_{\parallel,\alpha}. \quad (3.54)$$

Construction by substitution

Now that we have determined the dominant components of the perpendicular drifts, we can construct a general set of drift-reduced equations, taking advantage of the δ ordering. To do this we substitute the drift-reduced velocity (3.43) into the Braginskii equations (3.1) - (3.3).

We start by substituting only the leading order drifts $\mathbf{u}_{\perp,0}$ into the electron density equation:

$$\frac{\partial n_e}{\partial t} + \frac{\partial}{\partial \mathbf{x}} \cdot [n_e(\mathbf{u}_E + \mathbf{u}_{\text{dia},\alpha} + \mathbf{u}_{\parallel,e})] = S_n, \quad (3.55)$$

where we are doubly-justified in dropping the other drift terms because they are small in both δ and the mass ratio. The plasma is quasi-neutral, so $n_e = n_i = n$ for singly-charged hydrogen species. Using a series of vector calculus identities (given more explicitly in the steps (3.74) - (3.76) given later), we now split the spatial derivative terms so that the advection terms are on the left hand side, and terms due to magnetic curvature on the right hand side.

$$\frac{\partial n}{\partial t} + [\mathbf{u}_E + \mathbf{u}_{\parallel,e}] \cdot \frac{\partial n}{\partial \mathbf{x}} = -n\mathbf{B} \cdot \frac{\partial}{\partial \mathbf{x}} \left(\frac{u_{\parallel,e}}{B} \right) + \left(\frac{1}{e} \frac{\partial p_e}{\partial \mathbf{x}} - n \frac{\partial \phi}{\partial \mathbf{x}} \right) \cdot \nabla \times \left(\frac{\mathbf{b}}{B} \right) + S_n \quad (3.56)$$

Notice that the diamagnetic effects do not give rise to particle advection, a consequence of the microscopic nature of the diamagnetic drift as not actually a drift of guiding centres, only as the result of counting particle motions through an area in the fluid representation. This leads to a subtle cancellation (the ‘‘diamagnetic cancellation’’) inside divergence terms. However in regions of non-uniform field, this cancellation can leave a non-divergence-free component leftover however, which is what becomes the curvature operator

$$\nabla \times \left(\frac{\mathbf{b}}{B} \right) \cdot \cdot \quad (3.57)$$

The resulting part in the curvature operator is important for driving the system, but small. We also completely retain the full parallel fluid velocity, with no approximations or limitations on its magnitude. In most treatments of core transport the parallel velocity is assumed small, but as we will see when treating wall boundary conditions (section 3.6) we must allow for the parallel velocities to become of order $\sim c_s$.

With two fluids, we might expect to formulate an ion density equation next. But if $n_e = n_i$, we already have an evolution equation for n_i too. However the small deviations allowed by quasi-neutrality (combined with charge conservation) means we do need a second equation in order to describe the ion physics, effectively replacing the ion density equation with

$$\frac{\partial}{\partial \mathbf{x}} \cdot \mathbf{J} = 0, \quad (3.58)$$

where $\mathbf{J} = en_e(\mathbf{u}_i - \mathbf{u}_e)$. However because the ion and electron density equations are identical to first order, we need to retain terms higher order in δ so that the charge conservation equation is not just trivially zero:

$$\frac{\partial}{\partial \mathbf{x}} \cdot (\mathbf{J}_{\text{dia}} + \mathbf{J}_{\text{pol}} + \mathbf{J}_{\text{vis}} + \mathbf{J}_{\parallel}) = 0. \quad (3.59)$$

There is no current from electron-ion collisions because $R_i = -R_e$ - a consequence of Newton's 3rd law. Despite being even lower order in δ the polarization drift term is crucial to include because the balance of the $\mathbf{E} \times \mathbf{B}$ and diamagnetic terms means they almost cancel when under the divergence operator, and the remainder is smaller in δ , comparable to the polarization drift term. It also contains a time derivative of the perpendicular velocity - without it we would not have an evolution equation for the velocity. We make the approximation here of only including the leading order drift terms in the expression for the ion polarization velocity (and dropping the electron term entirely). This avoids the problem of the polarization drift term depending on the polarization drift, and so on ad infinitum.

Writing the polarization and viscous drifts in terms of the leading order velocities \mathbf{u}_0 gives

$$\mathbf{u}_{\text{pol},i} + \mathbf{u}_{\text{vis}} = \mathbf{b} \times \frac{1}{enB} \left[m_i n_i \left(\frac{\partial}{\partial t} + \mathbf{u}_0 \cdot \frac{\partial}{\partial \mathbf{x}} \right) \mathbf{u}_0 + \frac{\partial}{\partial \mathbf{x}} \cdot \mathbf{\Pi}_0 \right], \quad (3.60)$$

where $\mathbf{\Pi}_0$ is the viscous stress tensor evaluated using the leading order drift velocities \mathbf{u}_0 and

$$\mathbf{u}_{\perp,0} = \mathbf{b} \times \frac{1}{B} \left(\frac{\partial \phi}{\partial \mathbf{x}} + \frac{1}{en} \frac{\partial p_i}{\partial \mathbf{x}} \right). \quad (3.61)$$

Substituting this into the charge conservation equation gives a general expression for the drift-reduced charge conservation or quasi-neutrality equation as

$$\begin{aligned} - \frac{\partial}{\partial \mathbf{x}} \cdot \left\{ \mathbf{b} \times \frac{1}{B} \left[m_i n_i \left(\frac{\partial}{\partial t} + \mathbf{u}_0 \cdot \frac{\partial}{\partial \mathbf{x}} \right) \mathbf{u}_0 + \frac{\partial}{\partial \mathbf{x}} \cdot \mathbf{\Pi}_0 \right] \right\} \\ = \mathbf{B} \cdot \frac{\partial}{\partial \mathbf{x}} \left(\frac{J_{\parallel}}{B} \right) + \frac{\partial(p_i + p_e)}{\partial \mathbf{x}} \cdot \nabla \times \left(\frac{\mathbf{b}}{B} \right). \end{aligned} \quad (3.62)$$

Having separated out an evolution equation for the perpendicular motion, we also need evolution equations for the parallel electron and ion momentum. To obtain an electron parallel momentum equation we take the Braginskii momentum equation for a species α (3.2), set $\alpha = e$, and take a scalar product with the unit vector in the direction of the magnetic field \mathbf{b} .

$$\begin{aligned} m_e \left[\frac{\partial u_{\parallel,e}}{\partial t} + \mathbf{u}_{0,e} \cdot \frac{\partial u_{\parallel,e}}{\partial \mathbf{x}} - \left(\frac{\partial \mathbf{b}}{\partial t} + \mathbf{u}_{0,e} \cdot \frac{\partial \mathbf{b}}{\partial \mathbf{x}} \right) \cdot \mathbf{u}_{0,e} \right] \\ = e \left(\frac{\partial \tilde{A}_{\parallel}}{\partial t} + \nabla_{\parallel} \phi \right) - \frac{\nabla_{\parallel} p_e}{n} + \frac{e J_{\parallel}}{\sigma_{\parallel}} \\ - 0.71 \mathbf{b} \cdot \nabla T_e + \frac{R_{\parallel,0} - m_e u_{\parallel,e} S^{(n)}}{n} \end{aligned} \quad (3.63)$$

We have also dropped all but the leading component of the velocity \mathbf{u}_0 , and used the Braginskii expression for $\mathbf{R}_{\parallel,e}$. $\mathbf{\Pi}_e$ disappears as it is small in the mass ratio, and we included

\tilde{A}_{\parallel} , the fluctuating parallel component of the magnetic vector potential (which corresponds to fluctuations only in B_{\perp} , as promised earlier.

If we assume inertial, electromagnetic, and frictional forces are weak, then equation (3.63) reduces to simply a balance between parallel electrostatic fields and the the parallel gradient of the pressure. Further assuming that n varies little along the field line, we conclude that the so-called ‘‘adiabatic condition’’ $e\phi \sim T$ is normally satisfied, so we expect potential and temperature fluctuations to closely follow one another.

The ion parallel momentum equation is obtained the same way, with $\alpha = i$ and applying $\mathbf{b} \cdot$.

$$\begin{aligned} m_i \left[\frac{\partial u_{\parallel,i}}{\partial t} + \mathbf{u}_{0,i} \cdot \frac{\partial u_{\parallel,i}}{\partial \mathbf{x}} - \left(\frac{\partial \mathbf{b}}{\partial t} + \mathbf{u}_{0,i} \cdot \frac{\partial \mathbf{b}}{\partial \mathbf{x}} \right) \cdot \mathbf{u}_{0,i} \right] \\ = -e \left(\frac{\partial \tilde{A}_{\parallel}}{\partial t} + \nabla_{\parallel} \phi \right) - \frac{\nabla_{\parallel} p_i}{n} - \mathbf{b} \cdot \frac{\partial}{\partial \mathbf{x}} \cdot \mathbf{\Pi}_i + \frac{R_{\parallel,0} - m_i u_{\parallel,i} S^{(n)}}{n} \end{aligned} \quad (3.64)$$

The Braginskii equation for temperature (3.3) can be replaced by an equivalent one for pressure

$$\frac{3}{2} \left[\frac{\partial p_{\alpha}}{\partial t} + \mathbf{u}_{\alpha} \cdot \nabla p_{\alpha} \right] = -\frac{5}{2} p_{\alpha} \frac{\partial}{\partial \mathbf{x}} \cdot \mathbf{u}_{\alpha} - \mathbf{\Pi}_{\alpha} : \nabla \mathbf{u}_{\alpha} - \frac{\partial}{\partial \mathbf{x}} \cdot \mathbf{q}_{\alpha} + Q_{\alpha}, \quad (3.65)$$

which we can verify by expanding the pressure derivative using the product rule and inserting the density equation (3.1). Choosing first the electron pressure, we can reorganise by combining the diamagnetic advection term and the binormal component of \mathbf{q}_e , before moving it to the right hand side to show its form as the curvature drive of the pressure

$$\frac{5}{2} \frac{1}{e} \frac{\partial (p_e T_e)}{\partial \mathbf{x}} \cdot \nabla \times \left(\frac{\mathbf{b}}{B} \right). \quad (3.66)$$

We can also drop one of the perpendicular components of \mathbf{q}_e (keeping the binormal part), as well as the parts proportional to $\mathbf{b} \times \mathbf{J}$, as they are smaller than the diamagnetic contributions by the square root of the mass ratio. Similarly we can drop the terms proportional to $\mathbf{J} \cdot \mathbf{J}_{\perp}$ and $\mathbf{J} \cdot (\mathbf{b} \times \nabla_{\perp} T_e)$ in Q_e (3.23), resulting in this evolution equation for the electron pressure

$$\begin{aligned} \frac{3}{2} \left[\frac{\partial}{\partial t} + (\mathbf{u}_E + \mathbf{u}_{\parallel,e}) \cdot \frac{\partial}{\partial \mathbf{x}} \right] p_e = -\frac{5}{2} \left[p_e \frac{\partial \phi}{\partial \mathbf{x}} + \frac{1}{e} \frac{\partial (p_e T_e)}{\partial \mathbf{x}} \right] \cdot \nabla \times \left(\frac{\mathbf{b}}{B} \right) \\ - \frac{5}{2} p_e \mathbf{B} \cdot \frac{\partial}{\partial \mathbf{x}} \left(\frac{u_{\parallel,e}}{B} \right) + \frac{0.71 T_e}{e} \mathbf{B} \cdot \frac{\partial}{\partial \mathbf{x}} \left(\frac{J_{\parallel}}{B} \right) \\ + \mathbf{B} \cdot \frac{\partial}{\partial \mathbf{x}} \left(\frac{\kappa_{\parallel,e}}{B^2} \mathbf{B} \cdot \frac{\partial T_e}{\partial \mathbf{x}} \right) + \frac{J_{\parallel}^2}{\sigma_{\parallel}} - Q_i. \end{aligned} \quad (3.67)$$

The corresponding ion energy equation can be obtained by a similar set of steps

$$\begin{aligned}
\frac{3}{2} \left[\frac{\partial}{\partial t} + (\mathbf{u}_E + \mathbf{u}_{\parallel,i}) \cdot \frac{\partial}{\partial \mathbf{x}} \right] p_i &= - \frac{5}{2} \left[p_i \frac{\partial \phi}{\partial \mathbf{x}} - \frac{1}{e} \frac{\partial (p_i T_i)}{\partial \mathbf{x}} \right] \cdot \nabla \times \left(\frac{\mathbf{b}}{B} \right) \\
&\quad - \frac{5}{2} p_i \mathbf{B} \cdot \frac{\partial}{\partial \mathbf{x}} \left(\frac{u_{\parallel,i}}{B} \right) - \frac{5}{2} p_i \frac{\partial}{\partial \mathbf{x}} \cdot (\mathbf{u}_{p,i} + \mathbf{u}_{\Pi}) \\
&\quad + \mathbf{B} \cdot \frac{\partial}{\partial \mathbf{x}} \left(\frac{\kappa_{\parallel,i}}{B^2} \mathbf{B} \cdot \frac{\partial T_i}{\partial \mathbf{x}} \right) + \frac{\partial}{\partial \mathbf{x}} \cdot (\kappa_{\perp,i} \nabla_{\perp} T_i) \\
&\quad + \mathbf{\Pi}_0 : \nabla \mathbf{u}_0 + Q_i
\end{aligned} \tag{3.68}$$

but we are later going to neglect the ion pressure (see 3.4.1).

3.4 STORM Model

The STORM⁶ model is a simplified set of drift-reduced equations describing the SOL, implemented through the STORM module for BOUT++ (see chapter 4).

3.4.1 Approximations

To derive the equations used in the STORM model we start from the general drift-reduced equations described at the end of section 3.3, and apply a series of additional approximations intended to make the model computationally tractable. Some of these assumptions can be fully or partially relaxed in more general models, but here we give only the forms which are used in this thesis.

Cold ions

A major first approximation we will make is to assume that the temperature of the ions is zero. (The STORM code does now allow for hot ions instead though.) This sets $T_i = p_i = 0$ and so drastically simplifies the equations, dropping the ion pressure equation (3.68), the ion diamagnetic drift, and the complicated gyroviscous terms in the ion viscous stress tensor.

However $T_i = 0$ is not experimentally justified, as in fact often $T_i > T_e$ in the SOL. It is nevertheless a common simplification in SOL models, because the main physics of filament motion (interchange drive and ExB motion) do not require hot ions, which apply only a correction to these mechanisms. As the ion pressure enters the charge conservation equation (which as we will see in section 3.4.3 becomes the vorticity equation, the dominant equation for perpendicular motion) in the same way as the electron pressure, we expect a system with non-zero ion temperature to display similar overall dynamics, even if the absolute magnitude of the

⁶(Either Scrape-off layer TuRbulence Models, or Scrape-Off layer Turbulence Oriented Module, depending on who you ask.)

drives are different. For fusion physics, capturing the overall trends is the most important goal, because they can then be calibrated against experimentally-derived scalings. Some work has been performed with a generalized version of the STORM model which includes hot ions[188]. It was found that finite ion temperature increased the coherency of filament-like structures, and the increased pressure increased the strength of the curvature drive, both of which lead to greater radial transport.

Electrostatic

The drift-ordering restricts inductive fluctuations of the magnetic field such that the total field contains only small local deviations $\tilde{\mathbf{B}}$ from the dominant static parallel component $B_{\parallel}\mathbf{b}$ around which the particles are magnetized

$$\mathbf{B} = B_{\parallel}\mathbf{b} + \tilde{\mathbf{B}}. \quad (3.69)$$

The amplitude of these fluctuations is much smaller compared to the amplitude of the equilibrium field \mathbf{B}_{eq} , so it is not necessary to include their feedback in the equations. The fluctuating component can be expressed in terms of the parallel component of the magnetic vector potential A_{\parallel}

$$\tilde{\mathbf{B}} = \nabla \times (A_{\parallel}\mathbf{b}), \quad (3.70)$$

which is self-consistently calculated from the parallel plasma current as

$$J_{\parallel} = -\mu_0\nabla^2 A_{\parallel}. \quad (3.71)$$

In general these fluctuations then act back on the electric field through

$$\begin{aligned} \mathbf{E}_{\perp} &= -\nabla_{\perp}\phi \\ \mathbf{E}_{\parallel} &= -\nabla_{\parallel}\phi - \frac{\partial A_{\parallel}}{\partial t}\mathbf{b}, \end{aligned} \quad (3.72)$$

as seen in equation (3.63).

However, in the Bohm normalisation (see section 3.4.2) the magnetic vector potential becomes normalised as

$$\frac{\beta m_i c_s}{2e}\psi = A_{\parallel} \quad (3.73)$$

where β is the plasma beta, the ratio of thermal to magnetic pressures. In the low-beta limit we neglect the variations in A_{\parallel} .

This low-beta or electrostatic approximation is well-justified numerically in that for an L-mode plasma in MAST $\beta \approx 1.6 \times 10^{-4}$ in the SOL, but work with an electromagnetically-generalised version of the STORM model argued that electromagnetic effects could still be

significant for SOL filaments in hotter H-mode plasmas, or in general for high- β machines including future reactors[6].

With the electrostatic approximation applied we can neglect all time derivatives of \mathbf{B} , and calculate \mathbf{E} directly from the electric potential.

Straight field lines

The three perpendicular equations (3.62), (3.56), & (3.67) all contain the so-called ‘‘curvature operator’’, defined as

$$\mathcal{C}(f) \equiv \nabla \times \left(\frac{\mathbf{b}}{B} \right) \cdot \nabla f, \quad (3.74)$$

where f is a scalar field. This operator can also be written as

$$\nabla \cdot \left(\frac{\mathbf{b} \times \nabla f}{B} \right). \quad (3.75)$$

While in a completely homogenous and straight magnetic field there would be no curvature term at all, this would lead to no drive for filament motion, and so clearly some curvature effects must be retained.

Equation (3.75) can be divided into two parts

$$\nabla \cdot \left(\frac{\mathbf{b} \times \nabla f}{B} \right) = \nabla \cdot \left(\frac{1}{B} \right) \cdot (\mathbf{b} \times \nabla f) + \frac{1}{B} (\nabla \times \mathbf{b}) \cdot \nabla f, \quad (3.76)$$

the first of which represents only the contribution of magnetic gradients, while the second is primarily due to magnetic curvature. The second can be manipulated sequentially by a circular shift of the triple product, the chain rule, the product rule for the curl operator, and Ampere’s law

$$\begin{aligned} \frac{1}{B} (\nabla \times \mathbf{b}) &= - \left(\mathbf{b} \times \nabla \left(\frac{1}{B} \right) \right) \\ &= \frac{1}{B^2} (\mathbf{b} \times \nabla B) \\ &= \frac{\nabla \times \mathbf{b}}{B} - \frac{\nabla \times \mathbf{B}}{B^2} \\ &= \frac{\nabla \times \mathbf{b}}{B} - \frac{\mu_0 \mathbf{J}}{B^2}. \end{aligned} \quad (3.77)$$

We can now write both terms of equation (3.76) in terms of the magnetic curvature vector $\boldsymbol{\kappa} \equiv (\mathbf{b} \cdot \nabla) \mathbf{b} = -\mathbf{b} \times (\nabla \times \mathbf{b})$, by using

$$\begin{aligned} \mathbf{b} \times \boldsymbol{\kappa} &= -\mathbf{b} \times (\mathbf{b} \times (\nabla \times \mathbf{b})) \\ &= -\mathbf{b} \cdot (\nabla \times \mathbf{b}) \mathbf{b} + \nabla \times \mathbf{b} \\ &= \nabla \times \mathbf{b} - \frac{\mu_0 \mathbf{J}_{\parallel}}{B}. \end{aligned} \quad (3.78)$$

These terms combine to give

$$\nabla \times \left(\frac{\mathbf{b}}{B} \right) = 2 \frac{\mathbf{b} \times \boldsymbol{\kappa}}{B} + \frac{\mu_0 (\mathbf{J}_{\parallel} - \mathbf{J}_{\perp})}{B^2}, \quad (3.79)$$

where one unit of $(\mathbf{b} \times \boldsymbol{\kappa})/B$ is from magnetic gradients, and the other from curvature.

The magnitude of the additional current-dependent term can be estimated. The dominant contribution to the perpendicular current is given by the diamagnetic contribution (which is equivalent to saying that the current is mostly that required for MHD force balance $\nabla p = \mathbf{J} \times \mathbf{B}$):

$$\begin{aligned} J_{\perp} &\approx B^{-1} \left| \mathbf{b} \times \frac{\partial(p_i + p_e)}{\partial \mathbf{x}} \right| \\ &\sim \frac{1}{L_{\perp}} \frac{\beta B}{\mu_0}. \end{aligned} \quad (3.80)$$

Charge conservation or quasineutrality implies $J_{\parallel} \sim J_{\perp}$, so the whole current-dependent term in (3.79) is $\mathcal{O}(\beta)$, and we neglect it by assuming low beta.

We now have an expression for the magnetic curvature term explicitly in terms of the magnetic curvature vector $\boldsymbol{\kappa}$. In this work we are considering only a simplified magnetic slab geometry (see section 3.5), which allows us to further simplify this expression for the curvature operator. The dominant magnetic field in a tokamak is toroidal, so to first order the field falls off radially as $1/R$, and would be represented in a cylindrical coordinate system (R, Φ, Z) as

$$\mathbf{B} = \frac{B_0 R_0}{R} \hat{\boldsymbol{\Phi}}. \quad (3.81)$$

As the magnitude of the curvature vector is the inverse of the radius of curvature, this gives the curvature vector as simply $\boldsymbol{\kappa} = (1/R) \hat{\mathbf{R}}$, so in our simplified magnetic geometry the curvature operator evaluated at the separatrix (denoted hereon as $\mathcal{C}(f)$) becomes

$$-\frac{2}{R_0 B_0} \frac{\partial f}{\partial y}, \quad (3.82)$$

where $R_0 = R_{\text{major}} + r_{\text{minor}}$ and $B_0 = B(R = R_0)$. By identifying Z with the binormal direction y perpendicular to both the major radius and the field, we have the simplified expression we will use for the curvature terms

$$\mathcal{C}(f) \equiv \nabla \times \left(\frac{\mathbf{b}}{B} \right) \cdot \nabla f \approx -\frac{2}{R_0 B_0} \frac{\partial f}{\partial y}. \quad (3.83)$$

By neglecting variations in R and B within the outboard SOL we have effectively also assumed low aspect ratio here.

These curvature operator terms are the only place in which we will keep any effects of non-uniformity of magnetic field: our approximation neglects any variation in \mathbf{B} in any other

terms. In conjunction with the electrostatic approximation, this approach effectively assumes that \mathbf{B} is constantly straight and has uniform magnitude in all terms, except for the specially-included curvature terms.

Boussinesq approximation

The magnetic curvature acts in a way analogous to buoyancy, as if filaments' radial motion were them rising to the top of a fluid. In buoyancy-driven convection systems in neutral fluids it is common to make the ‘‘Boussinesq approximation’’, used because it allows for removing the density entirely from the Navier-Stokes momentum equation.

In neutral fluids the Boussinesq approximation involves treating the density as temporally and spatially constant in convection terms, and assuming the only effect of the density variation is in the gravitational term (which represents the buoyancy forces). In the ESEL model the Boussinesq approximation is referred to instead as the thin layer approximation [189].

We make a similar approximation in the polarization current term in the charge conservation equation. Again it is possible to relax this approximation, but here we present only the simplest form.

The actual approximation used in the STORM model is

$$\begin{aligned} \frac{\partial}{\partial \mathbf{x}} \cdot \left[\frac{n_i}{B} \frac{d_0}{dt} \left(\frac{\nabla_{\perp} \phi}{B} \right) \right] &= \frac{n_i}{B} \frac{\partial}{\partial \mathbf{x}} \cdot \frac{d_0}{dt} \left(\frac{\nabla_{\perp} \phi}{B} \right) + \frac{d_0}{dt} \left(\frac{\nabla_{\perp} \phi}{B} \right) \cdot \frac{\partial}{\partial \mathbf{x}} \frac{n_i}{B} \\ &\approx \frac{n_i}{B} \frac{d_0}{dt} \left[\frac{\partial}{\partial \mathbf{x}} \cdot \frac{\nabla_{\perp} \phi}{B} \right], \end{aligned} \quad (3.84)$$

which effectively treats the density as being unaffected by the temporal and spatial derivatives. As in neutral fluids, this approximation is valid when density fluctuations are small relative to the typical background value, i.e. $\delta n/n_{e,0} \ll 1$. This is not well-justified in the SOL, where order-unity fluctuations are common.

Simplified dissipation

We have so far neglected to include the frictional drift term explicitly in the evolution equations on the grounds that it is $\mathcal{O}(\delta^2)$ (3.52). But small-scale diffusion is important numerically, and is further motivated by the analogy to neutral fluid equations. For these reasons artificial small-scale diffusion is often used in turbulence simulations, but if we keep the frictional and viscous terms in each evolution equation that it ultimately gives rise to (classical) collisional diffusion terms[189]. In the density equation the frictional term becomes

$$\nabla \cdot (n_e \mathbf{u}_{\text{fri}}) \approx -\nabla \cdot (D \nabla_{\perp} n_e) \approx -D \nabla_{\perp}^2 n_e. \quad (3.85)$$

The last approximation is an optional additional simplification of assuming that D is spatially-constant, or at least varying more slowly than the density. In the quasi-neutrality equation the ion viscosity term can be similarly approximated as

$$\nabla \cdot \Pi_i = -m_i n_e \mu_\omega \nabla_\perp^2 \mathbf{u}_E, \quad (3.86)$$

which sets the viscous drift velocity as

$$\mathbf{u}_{\text{vis}} = \frac{m_i \mu_\omega}{e B^2} \nabla_\perp \nabla_\perp^2 \phi, \quad (3.87)$$

where μ_ω is the effective cross field kinematic viscosity of the ions. This becomes a current term in the quasi-neutrality equation, which under divergence becomes a diffusion of the scalar quantity $\nabla_\perp^2 \varphi$

$$\nabla \cdot \left(\frac{m_i \mu_\omega}{e B^2} \nabla_\perp \nabla_\perp^2 \varphi \right). \quad (3.88)$$

We will also add a diffusion term to the electron temperature evolution equation

$$\nabla \cdot (\chi_e \nabla_\perp T_e), \quad (3.89)$$

representing the divergence of the perpendicular part of \mathbf{q}_e . Technically, as $\kappa_{e,\perp} \neq \kappa_{e,\times}$, we should have anisotropic diffusion within the drift-plane, but we will neglect this and use only the perpendicular value.

The particle diffusion, viscosity, and temperature diffusion coefficients D , μ_ω , and χ_e can be classical, neoclassical, or just arbitrarily set if desired. They represent collisional cross-field transport, with expressions derived in terms of local plasma parameters [161]

$$D^{\text{cl}} = \left(1 + \frac{T_i}{T_e} \right) \rho_e^2 \nu_{ei} \quad (3.90)$$

$$\mu_\omega^{\text{cl}} = \frac{3}{4} \rho_i^2 \nu_{ii} \quad (3.91)$$

$$\chi_e^{\text{cl}} = 4.66 \rho_e^2 \nu_{ei}. \quad (3.92)$$

In a toroidal plasma the collisional perpendicular transport coefficients are adjusted according to neoclassical transport theory, and now given by [161]

$$D^{\text{neo}} = (1 + 1.3q^2) D^{\text{cl}} \quad (3.93)$$

$$\mu_\omega^{\text{neo}} = (1 + 1.6q^2) \mu_\omega^{\text{cl}} \quad (3.94)$$

$$\chi_e^{\text{neo}} = (1 + 1.6q^2) \chi_e^{\text{cl}}. \quad (3.95)$$

The factor q is the so-called safety factor, which measures the average pitch of the magnetic field lines. In large aspect ratio circular tokamaks, q is given by

$$q = \frac{r B_\Phi}{R B_\theta}, \quad (3.96)$$

where r is the minor radius, R the major radius, B_Φ the toroidal field, and B_θ the poloidal field. The dependence of these expressions on ν_{ei} and ρ_i means that we cannot set the ion temperature to zero as we have assumed elsewhere, instead we retain a fixed finite T_i (comparable to T_e) only as an input to these expressions.

3.4.2 Normalisation

The Braginskii fluid equations are only rigorously valid for lengths much greater than the ion Larmor radius and times much longer than the ion gyration time, so it is convenient to normalise the length and time scales in order to work in units of $\rho_s \equiv c_s/\Omega_i$, & Ω_i :

$$\frac{\mathbf{x}}{\rho_s} \rightarrow \mathbf{x}, \quad \Omega_i t \rightarrow t. \quad (3.97)$$

For the 2D closures in section 3.7 we will need a characteristic length in the parallel direction, which we also represent in terms of the same length scale

$$L_\parallel \equiv \frac{l_\parallel}{\rho_s}. \quad (3.98)$$

The evolving variables of the model are normalised relative to characteristic values. For density and temperature these are simply some values chosen to typical of the SOL. When discussing the drift-ordering, characteristic potential fluctuations are set by the temperature ($e\phi \sim T$), so are normalised similarly. We need to allow for parallel velocities to be of the order of the ion sound speed (as the parallel dynamics are fluid-like), and vorticity (which has units of rotations per unit time) is expressed in terms of the ion gyration frequency:

$$\begin{aligned} n &\equiv \frac{n_e}{n_{e,0}}, & T &\equiv \frac{T_e}{T_{e,0}}, & \phi &\equiv \frac{e\varphi}{T_{e,0}}, \\ V &\equiv \frac{u_{\parallel,e}}{c_s}, & U &\equiv \frac{u_{\parallel,i}}{c_s}, & \Omega &\equiv \frac{\omega}{\Omega_i}. \end{aligned} \quad (3.99)$$

From these we can construct the characteristic sizes of currents and sources

$$J_\parallel \equiv \frac{j_\parallel}{en_{e,0}c_s}, \quad S_n \equiv \frac{S^{(n)}}{n_{e,0}\Omega_i}, \quad S_E \equiv \frac{W}{n_{e,0}T_{e,0}\Omega_i}. \quad (3.100)$$

and of dissipation coefficients

$$\nu_\parallel \equiv \frac{0.51\nu_{ei}}{\Omega_i}, \quad \hat{\eta} \equiv \frac{\eta_\parallel}{B/(en_{e,0})} = \frac{\nu_\parallel}{\mu n}, \quad (3.101)$$

$$D_n \equiv \frac{D}{D_{\text{Bohm}}}, \quad \mu_\Omega \equiv \frac{\mu_\omega}{D_{\text{Bohm}}}, \quad \chi_e \equiv \frac{\chi_\perp}{D_{\text{Bohm}}} \quad (3.102)$$

where ν_{\parallel} is the normalised resistivity (obtained by inverting (3.13)), $D_{\text{Bohm}} \equiv \rho_s^2 \Omega_i$ is the Bohm diffusion coefficient. We also normalise the magnitude of the effective gravity drive

$$\hat{g} \equiv \frac{g}{\rho_s \Omega_i^2} = \frac{2\rho_s}{R}, \quad (3.103)$$

and define a shorthand for the ion-to-electron mass ratio (~ 3600 for a deuterium plasma)

$$\mu \equiv \frac{m_i}{m_e}. \quad (3.104)$$

3.4.3 Equations

With these approximations we can now simplify the drift-reduced equations (3.62), (3.56), (3.64), (3.63) & (3.67) to obtain the equations used in the STORM model.

The operator representing advection of the scalar field f in the perpendicular plane has a simplified form when the advection is due to the $\mathbf{E} \times \mathbf{B}$ velocity

$$\begin{aligned} (\mathbf{u}_{\mathbf{E}} \cdot \nabla) f &= \left(\frac{\mathbf{b} \times \nabla \phi}{B} \right) \cdot \nabla f \\ &\rightarrow \frac{1}{B} (\mathbf{b} \times \nabla \phi) \cdot \nabla f \\ &= \frac{1}{B} \left(\frac{\partial \phi}{\partial x} \frac{\partial f}{\partial y} - \frac{\partial \phi}{\partial y} \frac{\partial f}{\partial x} \right). \end{aligned} \quad (3.105)$$

We therefore define the *Poisson bracket* operator as

$$\{\phi, f\} \equiv \frac{1}{B} \left(\frac{\partial \phi}{\partial x} \frac{\partial f}{\partial y} - \frac{\partial \phi}{\partial y} \frac{\partial f}{\partial x} \right), \quad (3.106)$$

where for example the bracket $\{\phi, n\}$ would physically represent the advection of density n in the perpendicular drift plane by the $\mathbf{E} \times \mathbf{B}$ drift caused by the potential ϕ .

Density equation

The drift-reduced density equation (3.56) is already almost in a form suitable for computation. In slab geometry the B -dependence in the first term on the RHS of (3.56) cancels out, $\mathbf{u}_{\mathbf{E}} \cdot \frac{\partial n}{\partial \mathbf{x}}$ becomes a Poisson bracket, and the second term on the RHS can be represented using the simplified curvature operator. We also add in the perpendicular density diffusion term that stems from the frictional drift. Expressed in STORM-normalised units this gives the mass continuity (or density evolution) equation as

$$\frac{\partial n}{\partial t} = -\{\phi, n\} - V \nabla_{\parallel} n - n \nabla_{\parallel} V + \mathcal{C}(p) - n \mathcal{C}(\phi) + \nabla \cdot (\mu_n \nabla_{\perp} n) + S_n. \quad (3.107)$$

Ion parallel momentum equation

The STORM ion parallel momentum equation can be derived starting from (3.64), in the electrostatic limit, using $R_{\parallel,i}$ from (3.11). The ion diamagnetic advection disappears because $p_i = 0$, and the viscous term is small in δ , so remaining is

$$\frac{\partial U}{\partial t} = -\{\phi, U\} - U\nabla_{\parallel}U - \nabla_{\parallel}\phi - \frac{\nu}{\mu}(U - V) + 0.71\nabla_{\parallel}T - U\frac{S_n}{n} \quad (3.108)$$

Electron parallel momentum equation

In the electrostatic case (3.63) becomes

$$m_e \left[\frac{\partial}{\partial t} + \mathbf{u}_{0,e} \cdot \frac{\partial}{\partial \mathbf{x}} \right] u_{\parallel,e} = e\nabla_{\parallel}\phi - \frac{\nabla_{\parallel}p_e}{n} + \frac{eJ_{\parallel}}{\sigma_{\parallel}} - 0.71\nabla_{\parallel}T_e + \frac{R_{\parallel,0} - m_e u_{\parallel,e} S_n}{n}. \quad (3.109)$$

The electron diamagnetic advection is not present because of the diamagnetic cancellation: the nearly divergence-free nature of the flow means that we only keep diamagnetic advection terms when they appear under a divergence, as they do in the density, vorticity and pressure equations, but do not here.

The $R_{\parallel,0}$ term represents interactions with other species, for example neutrals. Here our model does not consider neutrals (though some versions of the STORM model do include a simple fluid model of neutrals), so we drop this term.

$$\frac{\partial V}{\partial t} = -\{\phi, V\} - V\nabla_{\parallel}V - \mu\nabla_{\parallel}\phi - \frac{\mu}{n}\nabla_{\parallel}p + \nu(U - V) - 0.71\mu\nabla_{\parallel}T - V\frac{S_n}{n} \quad (3.110)$$

Vorticity equation

In the electrostatic limit equation (3.62) becomes

$$\begin{aligned} m_i \frac{\partial}{\partial \mathbf{x}} \cdot \left[\frac{n_i}{B} \frac{d_0}{dt} \left(\frac{\nabla_{\perp}\phi}{B} + \frac{\nabla_{\perp}p_i}{enB} \right) \right] - \frac{\partial}{\partial \mathbf{x}} \cdot \left(\mathbf{b} \times \frac{\partial}{\partial \mathbf{x}} \cdot \mathbf{\Pi}_0 \right) \\ = \mathbf{B} \cdot \frac{\partial}{\partial \mathbf{x}} \left(\frac{J_{\parallel}}{B} \right) + \frac{\partial(p_i + p_e)}{\partial \mathbf{x}} \cdot \nabla \times \left(\frac{\mathbf{b}}{B} \right) \end{aligned} \quad (3.111)$$

We drop the ion terms as $p_i = 0$, and applying the Boussinesq approximation (3.84), zero ion temperature and static, constant magnetic field allows us to write the first term in terms of the parallel component of vorticity (the fluid rotation in the perpendicular plane)

$$\frac{\partial}{\partial \mathbf{x}} \cdot \left[\frac{n_i}{B} \frac{d_0}{dt} \left(\frac{\nabla_{\perp}\phi}{B} \right) \right] \approx \frac{n_i}{B^2} \frac{d_0}{dt} \omega, \quad (3.112)$$

where the vorticity is equivalent to the parallel component of the curl of the $\mathbf{E} \times \mathbf{B}$ flow

$$\omega \equiv \mathbf{b} \cdot (\nabla \times \mathbf{u}_E) = \nabla \cdot (\nabla_{\perp}\phi). \quad (3.113)$$

(This definition also means that the electric potential plays the role of the streamfunction of the incompressible part of the flow in the perpendicular plane.) This means that through the polarization current, the charge conservation equation (3.62) becomes an evolution equation for the vorticity, which includes advection by the $\mathbf{E} \times \mathbf{B}$ velocity. In normalised units, with the viscosity term included, we have

$$\frac{\partial \Omega}{\partial t} = -\{\phi, \Omega\} - U \nabla_{\parallel} \Omega + \nabla_{\parallel} (U - V) + (U - V) \nabla_{\parallel} \log(n) + \frac{\mathcal{C}(p)}{n} + \frac{\nabla \cdot (\mu_{\Omega} \nabla_{\perp} \Omega)}{n} \quad (3.114)$$

Laplacian inversion

Equation (3.114) evolves the vorticity, but we need the potential to evaluate the other equations on the next timestep. Equation (3.113) is therefore an auxiliary equation which must also be solved at each timestep, and in normalised units is a Laplacian inversion problem

$$\Omega = \nabla \cdot \left(\frac{\nabla_{\perp} \phi}{B^2} \right). \quad (3.115)$$

Electron temperature equation

Starting from (3.67), we normalise, and add a term $\frac{1}{2\mu} V^2 S$ to account for the kinetic energy of particles introduced by the density sources to get

$$\begin{aligned} \frac{3}{2} \frac{\partial p}{\partial t} = & -\frac{3}{2} \{\phi, p\} - \frac{3}{2} V \nabla_{\parallel} p - \frac{5}{2} p \mathcal{C}(\phi) - \frac{5}{2} p \nabla_{\parallel} V - \nabla_{\parallel} q_{\parallel} \\ & - 0.71 j_{\parallel} \nabla_{\parallel} T + \frac{\nu}{\mu n} j_{\parallel}^2 + \frac{5}{2} [p \mathcal{C}(T) + T \mathcal{C}(p)] + \nabla \cdot (\chi_{\parallel, e} \nabla_{\perp} T) \\ & + S_E + \frac{1}{2\mu} V^2 S_n - \frac{V^2}{2\mu} \mathcal{C}(p) \end{aligned} \quad (3.116)$$

where we have introduced the parallel electron heat flux

$$q_{\parallel} = -\kappa_{\parallel 0} T^{5/2} \nabla_{\parallel} T - 0.71 j_{\parallel} T, \quad (3.117)$$

and S_E is defined by the normalisation relation (3.100).

In the version of the STORM code used in this thesis we evolve electron temperature instead of pressure. We can obtain the evolution equation for the temperature by multiplying the density equation (3.107) by $\frac{3}{2}T$ and subtracting it from the pressure equation (3.116), giving

$$\begin{aligned} \frac{\partial T}{\partial t} = & -\{\phi, T\} - \frac{2}{3} T \mathcal{C}(\phi) - V \nabla_{\parallel} T - \frac{2}{3} T \nabla_{\parallel} V - \frac{2}{3n} \nabla_{\parallel} q_{\parallel} \\ & - \frac{2}{3} 0.71 (U - V) \nabla_{\parallel} T + \frac{2}{3n} \frac{\nu}{\mu n} J_{\parallel}^2 + \frac{5}{3} T \mathcal{C}(T) + \frac{2T}{3n} \mathcal{C}(p) + \frac{2}{3n} \nabla \cdot (\chi_{\parallel, e} \nabla_{\perp} T) \\ & + \frac{2}{3n} S_E + \frac{2}{3n} \frac{1}{2\mu} V^2 S_n - \frac{2}{3n} \frac{V^2}{2\mu} \mathcal{C}(p) - \frac{T}{n} S_n. \end{aligned} \quad (3.118)$$

The only functional difference between (3.118) and (3.116) is that we have simplified the dissipation by ignoring the density diffusion term which would technically propagate through. Equations (3.107), (3.108), (3.110), (3.114), (3.115), (3.117) and (3.118) form a complete system, and require only the specification of initial and boundary conditions to solve.

3.5 Slab Geometry

The simulations performed in this thesis use a so-called *slab geometry*, which in addition to having straight field lines throughout, has target plates at each end perpendicular to the field lines. The slab (depicted in figure 3.5) also does not represent the full toroidal extent of the plasma - instead it is periodic in the binormal direction (the direction perpendicular to both the radius of curvature and the field lines), aiming to simulate only a fraction of the toroidal extent. Using a smaller domain is appropriate so long as the structures in experiment that we are trying to resolve do not exhibit variations on a global scale, or any scale larger than that of the simulation domain.

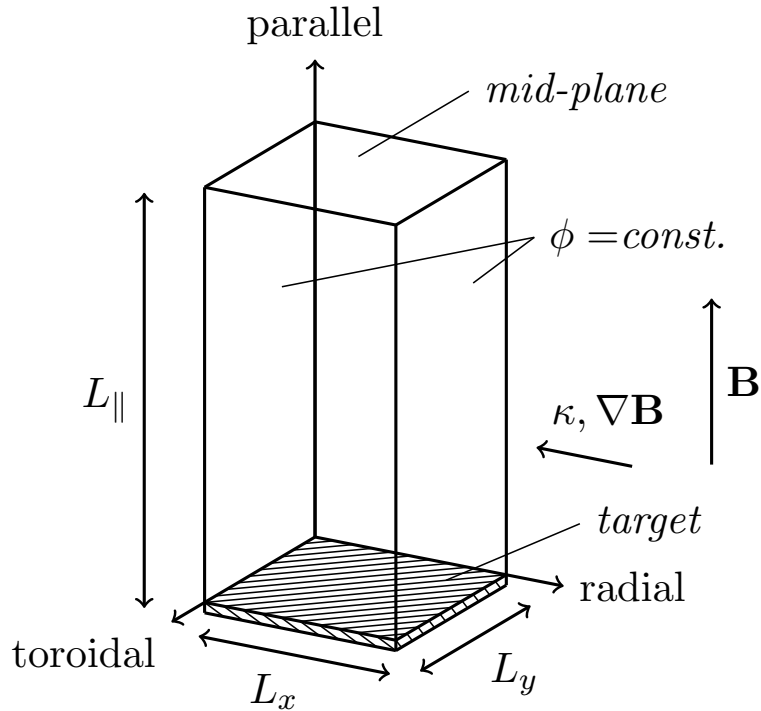


Figure 24: Schematic diagram of a simplified slab model of the scrape-off-layer. The geometry used in the 3D simulations extends upwards through the mid-plane to a symmetric second target above (not shown in this diagram).

3.6 Boundary Conditions

3.6.1 Location of domain boundaries

In 3D, our simulation domain for all simulations used in this thesis is a cuboid box, without explicit curvature or shear in the domain (see figure 3.5).

Therefore the domain is completely bounded by 6 sides: two target plates at the top and bottom, which lie perpendicular to the magnetic field (which is oriented along the y direction); two radial boundaries, one inner and one outer; and two binormal boundaries.

The binormal boundaries are simply periodic in all dynamical variables (i.e. n, T, U, V, Ω, ϕ), but the other two sets of boundaries are represented through more complicated conditions.

3.6.2 Sheath boundary conditions

In slab geometry (see section 3.5) we have solid target plates at either end of the domain in the vertical direction. At solid surfaces, the greater mobility of the electrons relative to the ions causes electrons to stick to that solid surface at a greater rate, imparting a negative charge to the surface. This creates a potential well, which then pulls positive charges towards it. This well can only extend a short distance into the plasma, because of Debye screening effects. The result is that the negatively-charged surface acts to accelerate ions towards it, whilst a thin layer of positive space charge forms in front of the surface and prevents deep penetration of the potential into the bulk plasma.

In the case of perpendicular field lines, this layer is known as the Bohm sheath, and the constraints it imposes on the velocities are given by standard theory[190]. The ion velocity is accelerated to the plasma sound speed as the sheath entrance (justifying our earlier choice of unrestricted ordering on the parallel velocities), which in normalised units is

$$|U| \geq \sqrt{T}. \quad (3.119)$$

The electron velocity is moderated:

$$|V| = \begin{cases} \sqrt{T} \exp(-V_{\text{fl}} - \phi/T), & \text{if } \phi > 0 \\ \sqrt{T} \exp(-V_{\text{fl}}), & \text{otherwise} \end{cases} \quad (3.120)$$

where the floating potential V_{fl} is

$$V_{\text{fl}} = \frac{1}{2} \log\left(\frac{2\pi}{\mu}(1 + 1/\mu)\right), \quad (3.121)$$

and the absolute value of U and V means only that the sign of the velocities is flipped for the other target plate. For the transmission of energy we have

$$Q_{\parallel} = \gamma_e pV \quad (3.122)$$

where the parallel power flux Q_{\parallel} is defined as

$$Q_{\parallel} = \frac{5}{2}pV + \frac{1}{2} \frac{nV^3}{\mu} + q_{\parallel}, \quad (3.123)$$

and γ_e , the electron energy transmission coefficient, is defined as

$$\gamma_e \equiv 2 - \frac{1}{2} \log\left(\frac{2\pi}{\mu}\right). \quad (3.124)$$

Therefore this boundary condition is actually enforced on the parallel heat flux q_{\parallel} as

$$q_{\parallel} = \left(\frac{1}{2} \log\left(\frac{\mu}{2\pi}\right) - \frac{1}{2}\right)pV + \frac{1}{2\mu}nV^3. \quad (3.125)$$

Therefore the boundary conditions in y placed on the variables U , V , and q_{\parallel} at the target plates are given by equations (3.119), (3.120), and (3.125) respectively.

No constraints on the other dynamical variables are imposed at the target plates, instead being left as *free* boundary conditions. This means that ϕ , Ω , n , and T are extrapolated in y from the inner domain to the divertor plates using a one-sided third-order finite difference scheme, such that these variables are available for the computations of expressions (3.119) - (3.125) above.

These target boundaries do not exist in 2D: the targets are instead treated through the closure approximations described in section 3.7.

3.6.3 Radial boundary conditions

As described we employ periodic boundary conditions on all variables in the binormal direction. The radial boundaries are more challenging: whilst there are a few first-principles theories describing how a fluid plasma model interacts with the vessel wall available in the literature (e.g.[191]), they introduce unnecessary complications. We wish to represent the core-SOL interaction with as few assumptions as possible, and so assume the wall is infinitely distant and impose reasonable boundary conditions. For the fluid variables n , T , Ω , U and V Neumann boundary conditions are used in order to allow the variables to “float” and hence be determined by the balance of radial turbulent transport and parallel loss. More precisely, at the inner and outer radial boundaries x_{in} and x_{out} we impose $\partial_x f = 0$ on $f = n, \Omega, U, V$ and T .

However, the electric potential must still be constrained in order to satisfy Laplace’s equation (3.115). To minimise the external constraint on ϕ whilst providing sufficient information to solve Laplace’s equation, we employ the same ad hoc approach used in [133]. We employ “evolving boundary conditions” in which the potential everywhere on the boundary is set to the mean value of the potential on that boundary averaged over the preceding time period τ . Formally this means we set ϕ on the inner and outer radial boundaries x_{in} and x_{out} through

$$\begin{aligned}\phi(x = x_{\text{in}}) &= \langle \phi(x = x_{\text{in}} + \Delta x_{\text{in}}/2) \rangle_{z,t \in [(j-1)\tau, j\tau]} \\ \phi(x = x_{\text{out}}) &= \langle \phi(x = x_{\text{out}} - \Delta x_{\text{out}}/2) \rangle_{z,t \in [(j-1)\tau, j\tau]}\end{aligned}\tag{3.126}$$

for all $t \in [j\tau, (j+1)\tau]$, where $j \in \mathbb{Z}^+$, and $\langle - \rangle_{z,t \in [(j-1)\tau, j\tau]}$ denotes a binormal- and time-average over the time interval $[(j-1)\tau, j\tau]$. τ is an input parameter which sets the length of preceding time over which the ϕ values are averaged, and all the simulations presented here used $\tau = 50/\Omega_{i,0}$.

In 2D the same conditions are used at the radial boundaries. This approach allows us to constrain fluctuations in the potential at the boundaries without fixing it at any specific arbitrary value.

3.7 2D STORM Model

A lot of SOL modelling work has previously been done using models which simplify the three-dimensional system by approximating the transport processes in the parallel direction. Not constrained by the magnetic field, the parallel physics is broadly separated from the drift dynamics of the perpendicular plane, and (when collisionality is high enough that kinetic effects can be ignored) is similar to that of a neutral fluid. The parallel flow speeds are different, being of the order of the parallel ion sound speed down the field lines, as opposed to being related to the gyration radius or gyrofrequency. However the difference in length scale (the parallel connection length L_{\parallel} vs the SOL width λ_n) means the timescales end up similar.

If the transport down the field lines is parameterized purely in terms of upstream or average fluid variables, then the terms depending only on perpendicular variations can be separated, and the remaining terms grouped into an overall parallel loss term. This requires making assumptions about the mechanism dominating the parallel transport, which may also entail making assumptions about the variation of the fluid variables in the parallel direction in experiment. This leads to different choices or “closures” which apply to different regimes of parallel dynamics.

These closures are computationally useful: as well as reducing the dimension, by eliminating the fastest parallel timescales in the system, they lead to large speedups. The fastest parallel timescale in 3D is either the electron thermal speed or the Alfvén speed, which are $\sim ns$, leading to a speedup of around a factor of 100 before reaching the ion cyclotron frequency limiting (3.34).

3.7.1 2D STORM equations

The parallel and perpendicular parts of the system of 3D equations are largely separable. If we group all terms containing any parallel derivatives into catch-all “loss” terms, then in the perpendicular drift-plane equations (3.107), (3.114), & (3.116) become

$$\frac{\partial n}{\partial t} = \frac{1}{B} \{\phi, n\} + n\mathcal{C}(\phi) + \frac{1}{n}\mathcal{C}(p) + S\mu_n \nabla_{\perp}^2 n - n_{\text{loss}}, \quad (3.127)$$

$$\frac{\partial \Omega}{\partial t} = \frac{1}{B} \{\phi, \Omega\} + \frac{\mathcal{C}(p)}{n} + \mu_{\Omega} \nabla_{\perp}^2 \Omega - \Omega_{\text{loss}}, \quad (3.128)$$

$$\begin{aligned} \frac{\partial T}{\partial t} = & \frac{1}{B} \{\phi, T\} - \frac{2}{3}T\mathcal{C}(\phi) + \frac{2T}{3n}\mathcal{C}(p) + \frac{5}{3}T\mathcal{C}(T) \\ & + \frac{2}{3n}S_E - \frac{TS}{n} + \frac{2}{3n}\kappa_{\perp 0} \nabla_{\perp}^2 T - T_{\text{loss}}, \end{aligned} \quad (3.129)$$

with the Laplacian inversion for the electrostatic potential (3.115) unchanged.

Evaluating the loss terms requires making assumptions about the parallel velocities. As we will therefore be setting U and V by assumption, we no longer require the evolution equations for U and V .

3.7.2 Parallel closures

At the target, the velocity of the electrons into the sheath is given by (3.120)

$$V_{\text{sh}}(\phi, T) = V_{\text{sh}0} \sqrt{T} e^{-\phi/T} \quad (3.130)$$

where

$$V_{\text{sh}0} = e^{-eV_{\text{th}}/T_{e,0}}. \quad (3.131)$$

“Sheath dissipation” closure

In the “sheath dissipation” closure we assume that the density and temperature are constant in the parallel direction, and treat the parallel velocities as equal to those at the sheath,

so $V = V_{\text{sh}}(\phi, T)$ and $U = 1$ (c_s in normalised units). The loss of density is then due to advection of particles at the speed V_{sh}

$$n_{\text{loss}} = \frac{1}{L_{\parallel}} n V_{\text{sh}}(\phi, T), \quad (3.132)$$

where the parallel derivative becomes the inverse parallel length scale. This can be interpreted as fluid variables (n, T, Ω, ϕ) being replaced by a corresponding average of the parallel domain $\langle n \rangle_{\parallel}$ etc., where

$$\langle \dots \rangle_{\parallel} = \frac{1}{L_{\parallel}} \int_{-L_{\parallel}}^{L_{\parallel}} \dots dz. \quad (3.133)$$

The vorticity loss term is set by the parallel current term in (3.111)

$$\frac{1}{n} \nabla_{\parallel} J_{\parallel}, \quad (3.134)$$

which expands to

$$\nabla_{\parallel}(U - V) + (U - V) \nabla_{\parallel} \log(n) \quad (3.135)$$

in equation (3.114). This can be evaluated at the sheath

$$\Omega_{\text{loss}} = \frac{1}{L_{\parallel}} (V_{\text{sh}}(\phi, T) - \sqrt{T}) \quad (3.136)$$

The parallel drainage rate for temperature is derived starting from equations (3.118). Assuming that $\nabla_{\parallel} n \approx \nabla_{\parallel} T \approx 0$, the only remaining parallel terms give us

$$\begin{aligned} \frac{3n}{2} \frac{\partial T}{\partial t} &= -\nabla_{\parallel}(nTV) - \nabla_{\parallel}(q_{\parallel}) + \dots \\ &= -\nabla_{\parallel}(nTV + q_{\parallel}) + \dots \end{aligned} \quad (3.137)$$

With $V \sim V_{\text{sh}}$, and averaged over the parallel domain of length L_{\parallel} this becomes

$$\frac{3n}{2} \frac{\partial T}{\partial t} = -\frac{1}{L_{\parallel}} \nabla_{\parallel}(nTV_{\text{sh}} + q_{\parallel, \text{sh}}), \quad (3.138)$$

where (following Stangeby [190]) the conductive parallel heat flux is

$$\begin{aligned} q_{\parallel, \text{sh}} &= Q_{\parallel, \text{sh}} - \frac{5}{2} nTV_{\text{sh}} \\ &= \gamma_e nTV_{\text{sh}} - \frac{5}{2} nTV_{\text{sh}} \\ &= \left(\gamma_e - \frac{5}{2} \right) nTV_{\text{sh}}. \end{aligned} \quad (3.139)$$

Therefore the parallel heat loss in the basic ‘‘sheath dissipation’’ closure is

$$\begin{aligned} T_{\text{loss}} &= \frac{2}{3n} \frac{1}{L_{\parallel}} \left(nTV_{\text{sh}} + \left(\gamma_e - \frac{5}{2} \right) nTV_{\text{sh}} \right) \\ &= \frac{2}{3n} \frac{1}{L_{\parallel}} \left(\gamma_e - \frac{3}{2} \right) nTV_{\text{sh}}, \end{aligned} \quad (3.140)$$

where $\gamma_e \approx 5.5$.

“Vorticity advection” closure

In contrast to the sheath dissipation closure’s assumption of constant parallel velocities, the “vorticity advection” closure models specifically the mid-plane, and assumes velocities decrease linearly from zero up to their full values at the sheath [135]. The mid-plane quantities are assumed to be advecting away down the field lines at the sound speed, so neglecting parallel currents, we approximate parallel advection terms as

$$U\nabla_{\parallel} \approx V\nabla_{\parallel} \approx \frac{\sqrt{T}}{L_{\parallel}}, \quad (3.141)$$

leads to loss terms of the form

$$n_{\text{loss}} = \frac{n\sqrt{T}}{L_{\parallel}}; \quad \Omega_{\text{loss}} = \frac{\Omega\sqrt{T}}{L_{\parallel}}; \quad T_{\text{loss}} = \frac{2T\sqrt{T}}{3L_{\parallel}}. \quad (3.142)$$

These can all be interpreted as an advective loss driven by parallel gradients, where (in the isothermal case) the rate of loss is just linearly proportional to the magnitude of the mid-plane quantity.

“Heuristic” closure

In this thesis we use a modified version of the sheath dissipation closure, which is motivated by the parallel transport processes known to be dominant in particular SOL regimes. For the density and vorticity loss term, this “heuristic” closure takes the density, temperature and parallel length scalings from the sheath dissipation closure, and linearises the sheath exponential term.

$$n_{\text{loss}} = \frac{1}{L_{\parallel}} n\sqrt{T} \left(1 - \left(V_{\text{fl}} + \frac{\phi}{T} \right) \right) \quad (3.143)$$

$$\Omega_{\text{loss}} = -\frac{1}{L_{\parallel}} \left(V_{\text{fl}} + \frac{\phi}{T} \right) \quad (3.144)$$

The temperature loss term begins with the dependence on parallel heat flux q_{\parallel} from equation (3.118)

$$T_{\text{loss}} = \frac{2}{3n} \frac{1}{L_{\parallel}} q_{\parallel}, \quad (3.145)$$

but attempts to capture the two main possibilities for parallel transport of temperature in the SOL in different regimes. This is done by interpolating between two regimes using an approach similar to Myra[192]

$$\frac{1}{q_{\parallel}} = \frac{1}{q_{\parallel\text{SL}}} + \frac{1}{q_{\parallel\text{CL}}}, \quad (3.146)$$

where a harmonic average is used because we are interpolating between two rates.

3.7.3 Parallel temperature regimes

Depending on the collisionality, there are different regimes for parallel transport of heat. We are interested in particular in the “Sheath-limited” and “Conduction-limited” regimes, because each of these can be associated with a different parallel profile of temperature.

“Sheath-limited”

The sheath-limited regime applies when collisionality is relatively low [68], and results in a parallel temperature profile that is relatively flat. This can occur in two ways.

The first way is the standard picture in which convective transport dominates over conductive in the domain. Power flows unimpeded towards the target, with nothing changing the temperature as it flows, leading to a flat parallel temperature profile. The limiting factor for overall power loss becomes the flux through the sheath at the target.

If instead the collisionality is low because the temperature at the mid-plane is sufficiently high, then the strong T -dependence of q in equation (3.117) can mean that the conductive part of the parallel heat flux dominates over the convective part, and even a small T gradient is immediately flattened by the large resultant flux. In this regime, only a small difference in upstream and target temperature is enough to transport all of the upstream power down to the target via conduction. The factor limiting the rate of heat transport out of the domain therefore becomes the flux through the sheath at the target. Confusingly, this particular regime is conduction-*dominated* whilst still being “sheath-limited”.

In either case the total heat flux leaving the domain in the parallel direction is limited by what can pass through the sheath and there are small parallel temperature gradients, so we make the same simplifications as we did in the “sheath dissipation” closure (i.e. that $\nabla_{\parallel} T \approx 0$, and $V \sim V_{\text{sh}}$). We therefore use equation (3.140), which after linearization gives

$$q_{\parallel\text{SL}} = \left(\gamma_e - \frac{3}{2} \right) nT\sqrt{T} \left(1 - \left(V_{\text{fl}} + \frac{\phi}{T} \right) \right). \quad (3.147)$$

“Conduction-limited”

The conduction-limited regime applies at higher collisionality, usually because everything is happening at relatively low temperatures. This means the conductive term in equation (3.117) is dominant over the convective term, but not strong enough to immediately flatten any parallel temperature gradient. Now that a significant gradient can be sustained, not only do we have a clearly different parallel profile to the sheath-limited case, but the size of the gradient between mid-plane and target now controls the total parallel heat flux.

With conductive heat transfer stronger than convective transfer, the overall flux is determined by the conductive part

$$q_{\parallel\text{CL}} = \frac{2}{7} \frac{1}{L_{\parallel}} \kappa_0 T^{7/2}. \quad (3.148)$$

(Myra[192] introduces an additional regime - “flux-limited” - which attempts to capture the failure of fluid theory to model parallel transport in the case that low collisionality causes the mean free path to be larger than the system size. We do not consider that here.)

We can now also see an alternative physical explanation of why the interpolation in equation (3.146) is a harmonic average: the harmonic average causes q_{\parallel} to tend towards whichever is the smaller of $q_{\parallel\text{SL}}$ and $q_{\parallel\text{CL}}$, corresponding to the bottleneck for the power coming from upstream to escape either being the transfer at the sheath or conductive transfer in the domain.

The “heuristic” parallel closure that we use is therefore equivalent to a linearized version of the “sheath-dissipation” closure, but which interpolates between two different regimes of parallel heat transport.

Chapter 4

Numerical Implementation

4.1 Introduction

The evolution of the physical model outlined in chapter 3 was simulated using the STORM module, which is built on the BOUT++ framework. In this chapter we outline the numerical implementation, beginning with a description of the BOUT++ framework, and differences from other similar codes. After explaining the generality available in the BOUT++ framework, we detail the specific choices of numerical methods made in the STORM module. Finally, the new xBOUT data processing and analysis package developed during this thesis project is described.

4.2 BOUT++

BOUT++ (BOUndary Turbulence in C++) is a software framework for solving arbitrary numbers of non-linear partial differential equations in 3D curvilinear coordinates in parallel[193]. The software is fully open-source, and the code is available at <https://github.com/boutproject/BOUT-dev>. Although BOUT++ can solve quite general sets of time-dependent equations in various geometries, it was designed for solving plasma fluid systems in the edge region of tokamak plasmas.

By providing many of the generic features required in a fluid simulation code, BOUT++ aims to automate a huge fraction of the development process for new physical models. For example, to write a tokamak plasma simulation code from scratch would require writing routines for memory management, parallelization over a single processor, communication between multiple processors, spatial differentiation, time integration, file input/output, curved geometry, and the complex topology of the tokamak edge region. BOUT++ provides implementations

of all of these core features, while retaining model flexibility, which drastically reduces the development time required.

BOUT++ was developed as a replacement for the older BOUT code[194], but with a emphasis on flexibility and modularity. It operates in general 3D curvilinear coordinates and complex mesh topologies, so can model various plasma configurations of interest. Since its first development BOUT++ has been upgraded with various different solver options and pre-conditioners[195], and verified with the method of manufactured solutions[196].

A description of the main features and capabilities of BOUT++ as used in STORM will be given here, but for an in-depth description of the code see the BOUT++ documentation[197].

4.2.1 Operator Representation

As BOUT++ is a framework, rather than a specific model, it allows a large set of differential equations to be solved. These are represented in the code by functions representing differential operators which act on Field variables, each of which represents a spatially-varying physical quantity. These functions are then expanded into a specific implementation depending on the numerical scheme chosen in the input file.

4.2.2 Physics Model

Specifying a complete system of equations to solve is done with a BOUT++ physics model. The model consists of C++ code which overloads methods in classes provided by the BOUT++ framework.

The physics model specifies the variables to solve for, how the simulation should be initialised, and the equations which are integrated at each timestep. The object-oriented operator representation allows the physics model to be relatively short for simple or common systems. For example, to solve a simplified 2D SOL model (2D slab, isothermal, SOL-only, normalised, with linear parallel loss terms)

$$\begin{aligned}\frac{dn}{dt} &= -\{\phi, n\} - ng\frac{\partial n}{\partial z} + g\frac{\partial n}{\partial z} - \frac{n}{L_{\parallel}} + D\nabla_{\perp}^2 n \\ \frac{d\omega}{dt} &= -\{\phi, \omega\} + \frac{g}{n}\frac{\partial n}{\partial z} - \frac{\omega}{L_{\parallel}} + \mu\nabla_{\perp}^2 \omega \\ \omega &= \nabla_{\perp}^2 \phi\end{aligned}\tag{4.1}$$

the system of equations 4.1 could be specified by the code in listing 4.1.

Listing 4.1: Example BOUT++ physics model for a simple 2D SOL turbulence model.

```
1 #include <bout/physicsmodel.hxx>
```

```

2 #include <invert_laplace.hxx>
3
4 class SOL2D : public PhysicsModel {
5 public:
6     virtual ~SOL2D() {}
7 protected:
8     int init(bool restarting);
9     int rhs(BoutReal t);
10 private:
11     // Define spatial variables: density, potential, and vorticity
12     Field3D n, phi, vort ;
13
14     BoutReal L ; // parallel connection length
15     BoutReal D, mu, g ; // diffusion, viscosity, drive
16
17     class Laplacian* phiSolver; // Laplacian solver for potential
18 } ;
19
20 // Initialise simulation
21 int SOL2D::init(bool restart) {
22
23     // Read options section from input file
24     Options *options = Options::getRoot()->getSection("sol2d");
25     OPTION(options, D, 0.01) ; // Read normalised diffusion
26     OPTION(options, mu, 0.01) ; // Read normalised viscosity
27     OPTION(options, g, 1.0) ; // Read effective gravity drive
28
29     // Read parallel connection length
30     Options::getRoot()->getSection("mesh")->get("Ly", L, 5000.);
31
32     SOLVE_FOR2(n, vort) ; // Explicitly evolve these variables
33     SAVE_REPEAT(phi) ; // Also write out potential
34
35     phiSolver = Laplacian::create() ; // Laplacian inversion
36
37     // Initialise the fields from expressions in input file
38     initial_profile("n", n) ;
39     initial_profile("n", vort) ;
40     phi = 0.0 ;
41
42     return 0;
43 }

```

```

44
45 // Specify equations to be integrated forwards in time
46 int SOL2D::rhs(BoutReal time) {
47
48 // Communicate variables between processors
49 mesh->communicate(n, vort) ;
50
51 // Solve for potential
52 phi = phiSolver->solve(vort) ;
53
54 // Communicate phi
55 mesh->communicate(phi) ;
56
57 // Continuity equation:
58 ddt(n) = - bracket(phi, n)           // ExB advection
59           - n*g*DDZ(phi) + g*DDZ(n) // interchange drive
60           - (1.0/L)*n                // parallel loss
61           + D*Delp2(n) ;            // diffusion
62
63 // Vorticity equation:
64 ddt(vort) = - bracket(phi, vort)    // ExB advection
65              + g*DDZ(n)/n           // interchange drive
66              - (1.0/L)*vort         // parallel loss
67              + mu*Delp2(vort) ;    // diffusion
68
69 return 0;
70 }
71
72 BOUTMAIN(SOL2D);

```

4.2.3 Numerical Flexibility

BOUT++ employs the method of lines, which separates the time integration from evaluation of spatial derivatives. In conjunction with the object-oriented structure of the code, this allows the user to choose which numerical methods are used for which terms - for example STORM uses an Arakawa scheme[198] for the perpendicular $\mathbf{E} \times \mathbf{B}$ advection terms.

Laplacian inversion problems are common in plasma physics, and BOUT allows the solver to be chosen separately.

There are various defaults for common boundary conditions such as Dirichlet, but there is also the option to implement custom boundary conditions.

4.2.4 Possible Geometries

BOUT++ is capable of solving equations on grids with varying geometry, different coordinate systems, and with different topologies.

The geometry is specified by providing the coordinate spacing between grid points, dx_{ij} , dy_{ij} , and dz_{ij} , where $i = 0, \dots, n_x$, where n_x is the number of grid points in the x direction etc. This makes the physical distance between grid points $\sqrt{g_{ij}dx^i dx^j}$, where g^{ij} are the components of the metric tensor, which are also required.

BOUT++ is most commonly used to simulate single- or double-null tokamak geometries, but has also been used to simulate linear devices[199], Stellarators (after considerable modifications [200]) and even Hall thrusters (albeit in 1D)[201].

As an example, figure 25 shows a rectilinear grid warped to model a hypothetical tokamak plasma edge with extremely strong shaping. A periodic boundary condition is then imposed on the two edges touching at the outboard mid-plane, to create a poloidally-continuous domain.

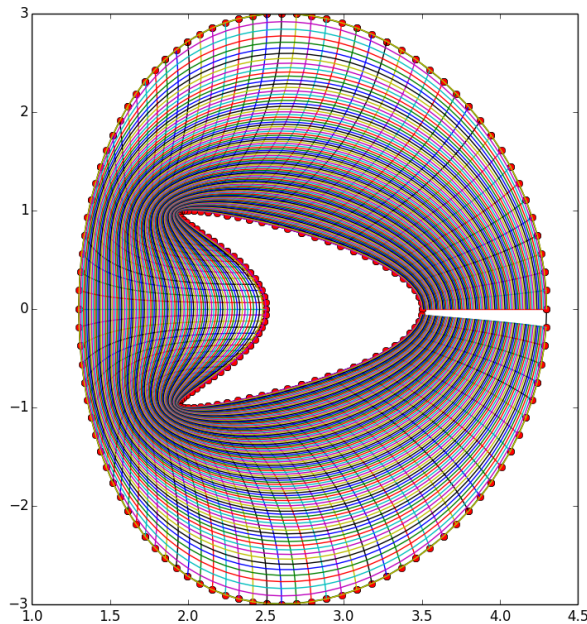


Figure 25: An example of a curvilinear BOUT++ simulation grid, modelling a hypothetical tokamak plasma edge with extremely strong shaping. (This plasma configuration may be physically impossible to realise, it is shown here only to emphasise the ability of BOUT++ to model a wide range of shapes.) Figure from the BOUT++ documentation at https://bout-dev.readthedocs.io/en/latest/user_docs/input_grids.html.

A slab geometry is much simpler, however - the grid spacings become uniform, and the metric tensor is simply the identity matrix. A 3D slab geometry is depicted in figure 3.5 in chapter 3.

4.3 STORM

Various models for scrape-off layer turbulence have been implemented in BOUT++, including STORM[135], Hermes[202], and SOLT3D[203].

These models are then comparable to several other plasma edge turbulence codes, such as GBS[172], TOKAM3X[176], GRILLIX[204], and HESEL[205]. (HESEL is similar enough that versions of that model have been re-implemented in BOUT++.)

STORM was originally developed by Luke Easy[135] for single-filament simulations in both 2D and 3D[148]. It was validated against GBS, HESEL and TOKAM3X[206], and then extended to model nonisothermal filaments[150], filaments propagating through a background of neutral particles[207], and electromagnetic filaments[6]. STORM was used to model multiple filaments interacting[153], and a simplified slab-divertor geometry[5] before being used for full MAST-U geometry simulations[133].

Here we briefly describe the main numerical features of STORM, but a more thorough explanation can be found in [135].

4.3.1 Time Solver

Both STORM2D and STORM3D integrate forwards in time using a fully implicit, variable order, variable time-step, Newton-Krylov Backwards Difference Formula (BDF) solver, which is from the PVIDE library [135, 208]. As an implicit scheme, the timestepping is more stable than an explicit scheme would be, at least in principle. In practice, implicit schemes require the solution of a large nonlinear system of equations as each step. The iterations required to solve this system may not converge, or converge very slowly, if the timestep is made too large.

4.3.2 Laplace Solver

The electrostatic potential needs to be obtained from the vorticity. In the general case, this requires solving for the generalised vorticity in three dimensions

$$\bar{\Omega} = n \nabla \cdot \nabla \phi + \nabla n \cdot \nabla_{\perp} \phi. \quad (4.2)$$

However, we apply the Boussinesq approximation (described in section 3.4.3), and then the flute approximation, $k_{\parallel} \ll k_{\perp}$, which allows us to neglect the parallel derivatives between each drift-plane. This leaves only

$$\Omega = \nabla_{\perp}^2 \phi, \quad (4.3)$$

to be inverted for ϕ on each drift-plane separately, which is a set of independent *Laplacian Inversion* problems.

This treatment of each drift-plane as independent (except for through the parallel momentum equations), as well as periodic boundary conditions in the binormal direction, means we can Fourier transform (4.3) in 2 dimensions to get

$$\frac{\partial^2 \hat{\phi}_{k_y}}{\partial x^2} + k_y^2 \hat{\phi}_{k_y} = \hat{\Omega}_{k_y}, \quad (4.4)$$

where \hat{f}_{k_y} is the k_y^{th} Fourier mode of the field f . As each of these k_y 's is independent, this transform further decomposes the problem. The second derivative can be written as a tri-diagonal matrix, and solved with a fast Thomas-like algorithm[209], before transforming back to real space to get $\phi(x)$.

It is worth noting that we could only use this fast method because we made the Boussinesq approximation - a significant motivation for employing it. Relaxing the Boussinesq approximation would introduce another term to (4.3), coupling the Fourier modes together so that the 2D domain has to be solved as one matrix, rather than decomposed into 1D problems which can be solved in parallel. Simulations without the Boussinesq approximation can be performed with STORM using the (more expensive) iterative ‘‘Naulin’’ method[210].

4.3.3 Staggered Grids

In order to avoid chequerboard-like numerical instabilities, STORM3D solves the parallel velocity fields U and V on grids which are staggered in the parallel direction relative to the other variables. It is simpler to stagger the parallel velocities instead of n & ϕ as the enforcing of the target boundary conditions is then simpler.

4.3.4 Evolving Logarithms

One way in which stability problems manifest in practice is when a turbulent fluctuation causes a field which should always be positive-valued (such as density or temperature) to become close to zero (or even negative) at some location. Multiple terms in the STORM model equations are divided by density or temperature, and so will blow up if the values of these fields approach zero.

To mitigate this problem, STORM actually evolves the logarithms of the density and temperature, not their absolute values. This means that even if a fluctuation causes $\log x$ to take a value < 0 at the end of a timestep, $x = e^{\log x}$ calculated at the start of the next will still be positive.

This formulation is analytically equivalent however, so the solutions should converge to the same answer at the same rate with increasing precision.

4.3.5 Boundary Conditions

The staggering of U and V mean that the implementation of the parallel boundary conditions at the target deal with a half-grid-point offset, and extrapolate the other variables as necessary onto the exact position of evaluation.

4.4 Analysis and post-processing tools

Although BOUT++ provides analysis and post-processing tools in python[211], IDL, MATLAB, and Mathematica, for this work the python tools were rewritten in order to take advantage of new capabilities of the latest available open-source software.

A new python analysis package for BOUT++ called xBOUT was written (available at <https://github.com/boutproject/xBOUT>), which principally relies upon the xarray package[212]. The core package including loading routines were written by myself, with additional features to handle non-slab geometries later added by John Omotani. Xarray is a library which provides labelled multidimensional array structures, which work by wrapping array objects provided by the numpy[213, 214] and dask[215] libraries. Xarray also facilitates easy file input & output via the netCDF[216] data format. Significant features were implemented upstream in xarray by myself as part of the development of xBOUT.

The new package can handle all types of BOUT++ geometries, up to double-null configurations. It is also designed with extensibility in mind, encouraging the subclassing of “accessor” classes for use with specific BOUT++ physics modules. For example, xSTORM is a small python package which contains analysis tools specifically to be used on simulation data generated using the STORM module for BOUT++.

Of particular note is the use of the Dask library, which allowed analysis functions to be applied across large datasets, operating in parallel in an out-of-core fashion[217]. This enabled easier analysis of much larger datasets, including the results of the 3D simulations presented in this thesis. Whilst the original tools available could only perform computational analysis on

arrays whose total size fit into local RAM, the parallel task management afforded by dask allows for analysis of almost arbitrarily large arrays, including ones many Terabytes in size. All the original numerical plots in this thesis were produced using these open-source tools. The SciPy library[218] was integral to several of the analysis functions applied. The analysis work was largely performed and recorded using Jupyter notebooks[219].

Chapter 5

Comparison of 2D and 3D

SOL-only models

The material in this chapter has been submitted as part of the jointly-authored paper “Comparing Two- and Three-Dimensional Models of Scrape-Off-Layer Turbulent Transport”, Nicholas et al., to *Plasma Physics and Controlled Fusion*, and is accessible on ArXiv[2].

5.1 Introduction

In this chapter we present simulation results comparing two- and three-dimensional models of a simplified SOL-only model. We show where the models agree, and demonstrate deviations in the results both between models and from experimental regimes.

5.2 Motivation

There exists a large catalogue of previous work done with the various 2D models (e.g. [113, 115, 139, 220, 221]), which continue to possess some advantages over the 3D models, such as computational speed, model simplicity, and physical interpretability.

If it were possible to understand the key differences between the results of simplified 2D and the more general 3D models, a lot of understanding might be transferable. Additionally if it turns out that the 2D models can consistently reproduce key features of the physics of the SOL, they could continue to be useful. Conversely, if 2D models omit important features of 3D models, then that should also be understood, so that the limitations of conclusions drawn from them are better known. Therefore in this chapter we systematically compare a representative 2D model with the closest 3D analogue.

5.3 Setup and Domain Geometry

The STORM code numerically solves equations (3.107)-(3.116) in 3D, and equations (3.127) - (3.129) in 2D. The dissipative parameters (μ_n , μ_Ω , κ_\perp , and κ_\parallel) were kept constant in time and space, and calculated using the classical expressions from [161], evaluated using the reference normalisation values of density and temperature (given in table 3). These are the same values used to simulate the MAST SOL in [179], and are similar to those used for the full 3D MAST-U geometry STORM simulations performed in [133]. Ion temperature is set to zero in the derivation of the main model equations for simplicity, but is included in table 3 because a finite value is still required for some of the dissipative expressions from [161]. The resistivity η_\parallel was allowed to vary, following the $T^{-3/2}$ dependence that follows from the definition

$$\eta_\parallel = 0.51 \frac{\nu_{ei0}}{T^{3/2} \Omega_{e0}} \quad (5.1)$$

n_0 [10^{-19}m^{-3}]	$T_{e,0}$ [eV]	$T_{i,0}$ [eV]	B_0 [T]
0.5	15	30	0.24

Table 3: Reference normalisation values of density and temperature, used for all simulations.

D_n	μ_Ω	κ_\perp	κ_\parallel	$\eta_\parallel(T = T_0)$
$2.1 \cdot 10^{-4}$	$1.6 \cdot 10^{-3}$	$3.3 \cdot 10^{-4}$	$4.4 \cdot 10^4$	$3.6 \cdot 10^{-5}$

Table 4: Normalised values of various dissipation coefficients used in all simulations in this chapter. Calculated using the standard classical expressions from the parameters given in table 3.

The equations were solved on a simplified cuboid domain (rectangular in 2D), which maps onto a schematic representation of the real SOL (figure 26). Vertically extending from target to target, the simplified domain can be interpreted as a straightened SOL flux tube, which has periodicity only in one direction. The pitch of the field lines at the edge means that our periodic direction perpendicular to both the major radius and the magnetic field in our simulations is angled relative to the real toroidal direction in experiments, and so will hereon be referred to as the binormal direction instead. The domain contains no magnetic shear, though this is a choice which could be relaxed in future work with STORM.

The numerical domain for the baseline 3D simulation spans $140.625\rho_s$ in the radial (x) direction, $4000.0\rho_s$ in the parallel (y) direction, and $150.0\rho_s$ in the binormal (z) direction (i.e. $L_x = 140.625$, $L_y = 4000.0$ and $L_z = 150$ in normalized units). The 3D domain is resolved

with $240 \times 32 \times 256$ grid points, meaning that the grid cells were square in the perpendicular plane. In 2D the domain covers the same (x, z) extent in normalized units, but a larger resolution is used of 960×1024 grid points, and (by definition) only a single grid point in the y direction. Convergence tests were performed to assess the impact of the perpendicular grid resolution, which showed that the grid used for 3D simulations is well resolved (see appendix A).

The simulations are source-driven, meaning that a volumetric density and energy source are present near the inner boundary of the domain (see figure 26). The source-driven simulations represent a SOL constantly fed with particles and power coming from the core plasma, and were chosen over fixing either the incoming flux or the pressure at the inner boundary so as to most directly compare the 2D and 3D models. This choice was made to impose as few constraints as possible on the resultant variable and flux profiles, and separate the self-consistently generated profiles as much as possible from the inner boundary conditions.

The magnitude of the source terms was chosen so that the densities and temperatures in the 2D simulation were representative of the MAST SOL in L-mode near the “separatrix”, i.e. around $1.0 \times 10^{-19} \text{m}^{-3}$ and 10eV. This represents a relatively low-power L-mode shot. The sources in the 3D simulations were then set such that the total particles and energy injected per second was the same as in the 2D simulations.

The sources (both temperature and density) are constant in the binormal direction, but have a Gaussian profile in the radial direction, centered upon a point located at $L_x/10$, and with a radial width of $L_x/120$. They are therefore extremely localised, and present only at one location on the inner side of the domain. In 3D the sources also have parallel extent. A top-hat function is used, so that the source extends from the mid-plane half-way to the target in both directions (so $L_S = 0.5L_{\parallel}$ in figure 26). The point in the parallel direction at which the source ends is intended to roughly represent the position of X-point. The baseline 3D simulation therefore represents an experimental regime in which the main source of particles and power is from the core, crossing over the separatrix between the two X-points. The inner part of the domain is therefore not considered to be physical, meaning that profiles should be compared to one another only from the radial position of the sources outwards.

The sources create gradients which display growing instabilities, which eventually non-linearly couple to produce turbulence which drives transport in the radial direction. Throughout the domain particles, momentum, and energy are lost - in 3D by fluxes through the targets at either end, and in 2D by heuristic loss terms approximating those same parallel processes.

The sources do not inhabit their own topologically-distinct region (i.e. there is no distinct

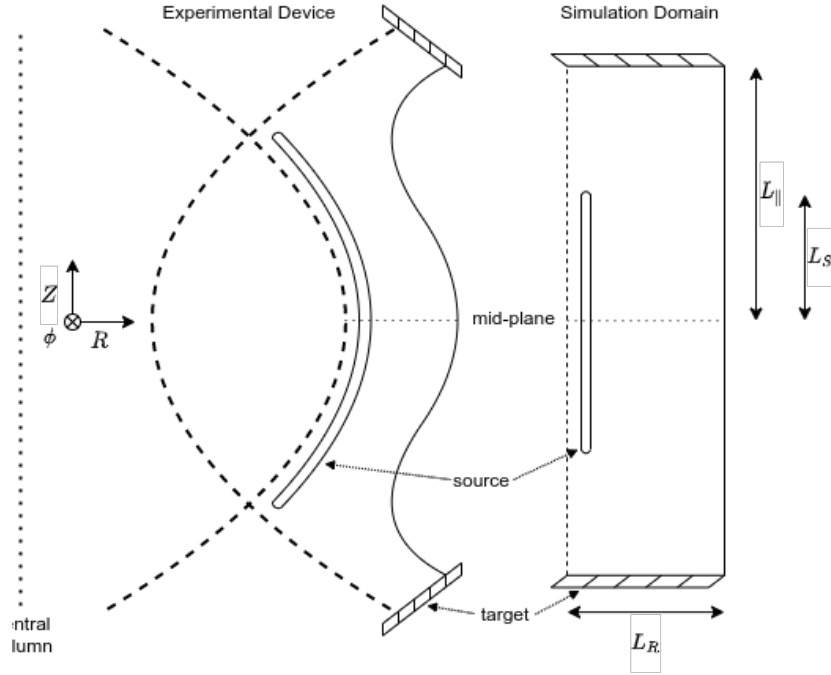


Figure 26: Schematic diagram of the relationship between the simplified 3D simulation domain and the full experimental device geometry. The 2D simulation domain here corresponds to a plane into the page located at the mid-plane. The basis set of vectors (R, Z, ϕ) denote the radial, vertical and toroidal directions in the experimental domain, but are aligned along the radial, parallel and binormal directions in the simplified simulation domain. In reality the simulation domain corresponds to a flux tube which is closer to horizontal than vertical (tilted into the page), because typically $B_{\text{tor}} > B_{\text{pol}}$ at the edge. In this paper the simulation domain only models the region outside of the separatrix, marked by the dashed line.

“core” region), as it was found that this setup introduces considerable complexities whose implications will be explored in chapter 6.

A statistical steady-state was required to represent a saturated L-mode turbulence regime. To obtain data from this state, each simulation was run with an initial “spin-up” phase which was then discarded, and only the following phase of statistical steady state was used for analysis. The spin-up phase lasted typically around 5ms, while the saturated phase was typically of the order of several milliseconds, which corresponds to thousands of turbulence correlation times.

A typical output of the code, which shows a snapshot of the density fluctuations at the mid-plane of a 3D simulation, is shown in figure 27.

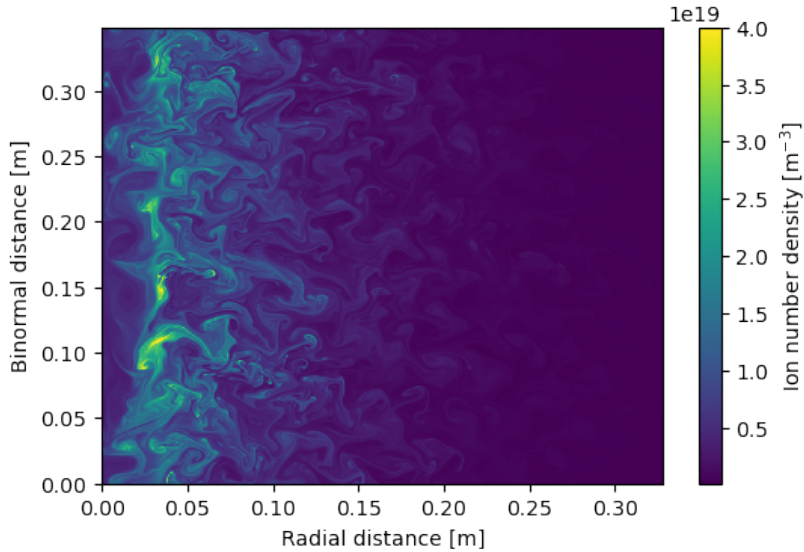


Figure 27: Snapshot of the typical spatial variation of the density during the saturated phase of a simulation using the two-dimensional STORM model.

5.4 Results and discussion

5.4.1 Comparison between 2D and 3D

There are multiple different metrics on which we can compare 2D and 3D simulations. Each of these metrics will help us assess the suitability of the simplified 2D for capturing some aspect of the more complex 3D physics, or for predicting some physical result of interest. As a baseline we first compare a single 3D simulation with a single 2D simulation, set up so as to have the same sources and parallel connection length.

Radial profiles

The time-averaged radial profiles of quantities represent the balance achieved in steady-state between perpendicular transport and parallel loss. In our model, which has hot electrons but cold ions, the fluid variables of interest that exist in both the 2D and 3D models are density, electron temperature, and potential.

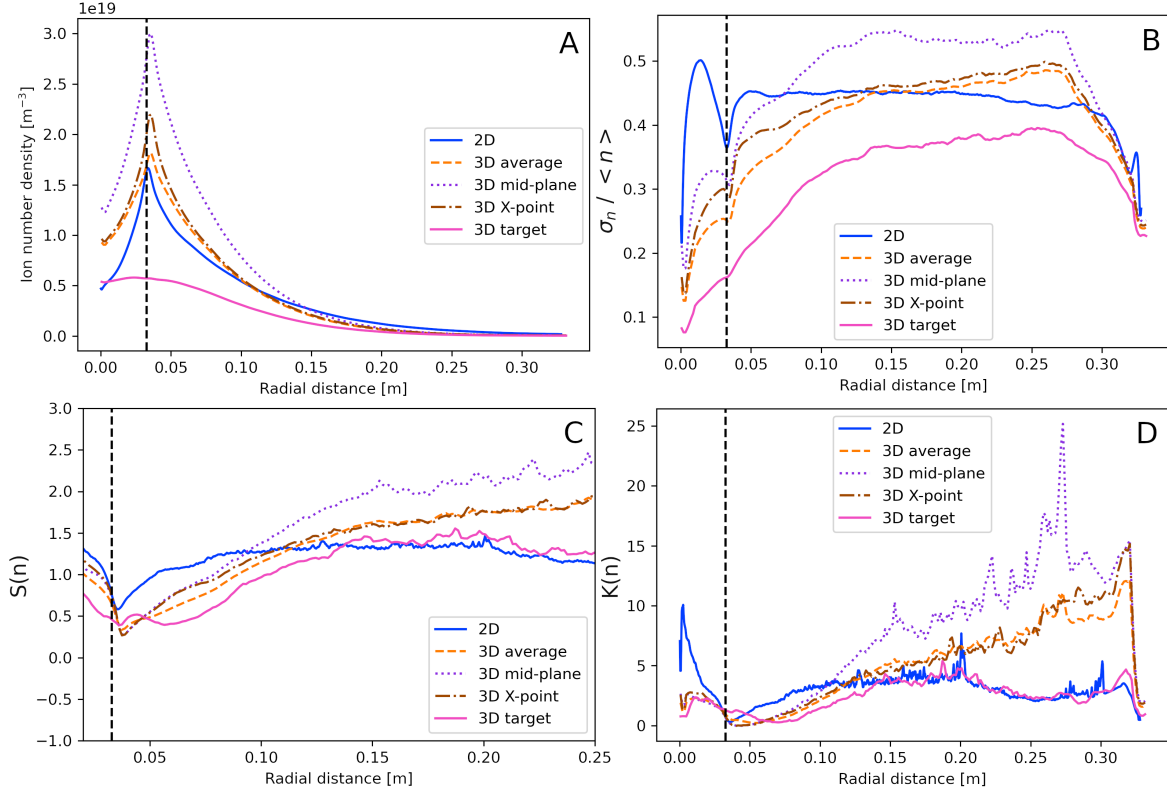


Figure 28: Average radial profiles of density (A), standard deviation of density fluctuations (B), skewness of density fluctuations (C), and kurtosis of density fluctuations (D). Fluctuations are defined relative to the time-averaged mean local density. Averages are performed over the saturated time periods, over the binormal direction, and in the case of the line labelled “3D average”, also over the parallel domain.

With respect to panel C, previous work [113] provides experimental (probe) values, indicating that in MAST experiments skewness increases radially, though to higher values than seen here (see figure 5 of [113]). This implies that the 3D simulations fit the experimental trend marginally better, though neither 2D nor 3D simulations really reproduced all of the features seen in the experimental skewness values.

We see in figure 28 (panel A) that the density profile is well-captured by the 2D simulation: the exponential falloff length is reproduced (fitting a decaying exponential to $x > L_x/10$ gives $\lambda_n = 6.5\text{cm}$ for the 2D line and $\lambda_n = 5.4\text{cm}$ for the 3D average line), and the absolute value matches that of the parallel-averaged value of the 3D domain.

However, the choice of which 3D average we compare to matters - there is a factor of 2 difference between the mid-plane value or the parallel-averaged value. For the 2D closure

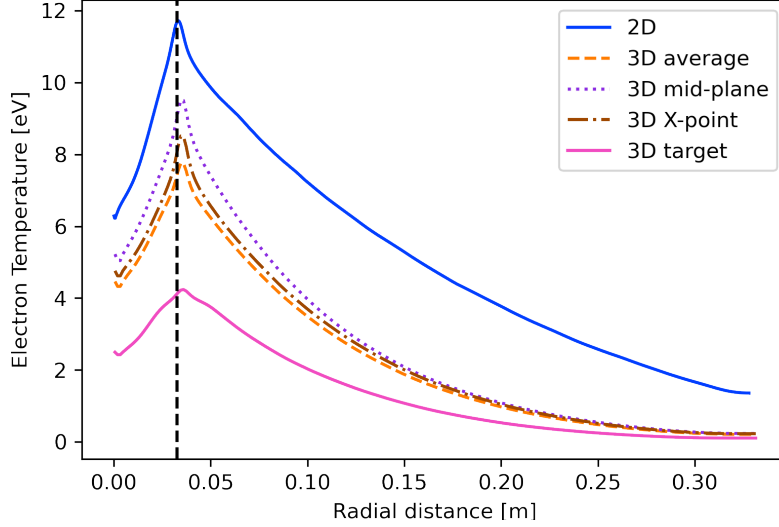


Figure 29: Average radial profiles of electron temperature. Averages are performed over the saturated time periods, over the binormal direction, and in the case of the line labelled “3D average”, also over the parallel domain.

used (see section 3.7) the most direct comparison is with the 3D results averaged along the parallel length. This follows from the derivation of the sheath-dissipation closure, which reduces a 3D problem to a 2D one by averaging along the parallel direction. Nevertheless in the profile plots in this chapter we explicitly include also the 3D mid-plane, 3D X-point, and 3D target profiles in addition to the 3D average profiles, so that more comparisons can be made.

The temperature is less well reproduced, being overestimated at all radial positions in 2D relative to 3D ($\lambda_T = 15.3\text{cm}$ for the 2D line and $\lambda_T = 8.2\text{cm}$ for the 3D average line). This implies that the parallel heat loss is weaker (for the same upstream temperature) in 2D than in 3D, as discussed in section 5.4.1. In the SOL the sheath causes characteristic potential fluctuations to be set by the temperature ($e\phi \sim T$), so a similar difference is seen in the potential.

Statistical properties

Whilst the profiles tell us about the overall balance of fluxes, the statistical properties of the timeseries capture some of the dynamics of the turbulent fluctuations themselves.

Figure 28 panel B, C and D show that the standard deviation, skewness, and kurtosis of the parallel-averaged fluctuations in 3D are comparable everywhere to the fluctuations in 2D. In

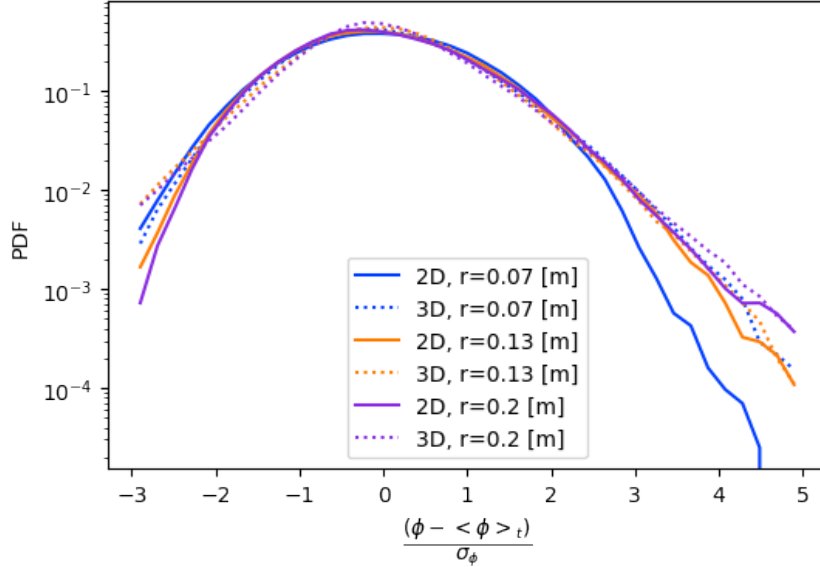


Figure 30: Averaged probability distribution functions of the fluctuations of the potential away from its mean value, plotted for different radial positions. There are some differences in the fluctuation distribution between the 2D and 3D simulations. The biggest differences seen at $r = 0.07$, where the 2D simulation under-predicts the frequency of extreme positive events relative to the 3D simulation. The differences are relatively small at $r = 0.13$, which is consistent with the 2D and 3D skewness curves crossing over at $r = 0.13$ in figure 28 panel C (however this figure plots potential fluctuations whilst figure 28 plots density fluctuations, so they do not match exactly). There are also some differences at $r = 0.2$, but concentrated in the left-hand side (i.e. negative fluctuations from the mean) and in the center.

the far SOL the skewness and kurtosis are relatively higher in 3D though - indicating that the 3D simulation allows a greater fraction of unusually high-density structures to persist out to the far SOL. This qualitative correspondence appears to hold for the whole distribution, not just for the first few moments - the probability distribution functions of the fluctuations in the potential show little difference between 2D and 3D in the SOL (figure 30).

This similarity is potentially encouraging for the purposes of comparison: it may indicate that the dominant perpendicular dynamics is largely unchanged by addition of parallel physics, and hence captured by the 2D model. This would then mean it is not important to capture the perpendicular modes which are present in 3D but not in 2D - for example the possibility of drift-waves in the 3D simulations.

However it is also possible that the dynamics needed to recreate the “universality” of fluctuation spectra observed both here and in experiment are relatively common[84], and that just

because a similar distribution is formed a similar underlying mechanism is not implied.

Power spectra

The power spectra tells us about cross-scale energetic transfer, as well as forcing and dissipation scales (at least in cases where the scales are not very broad).

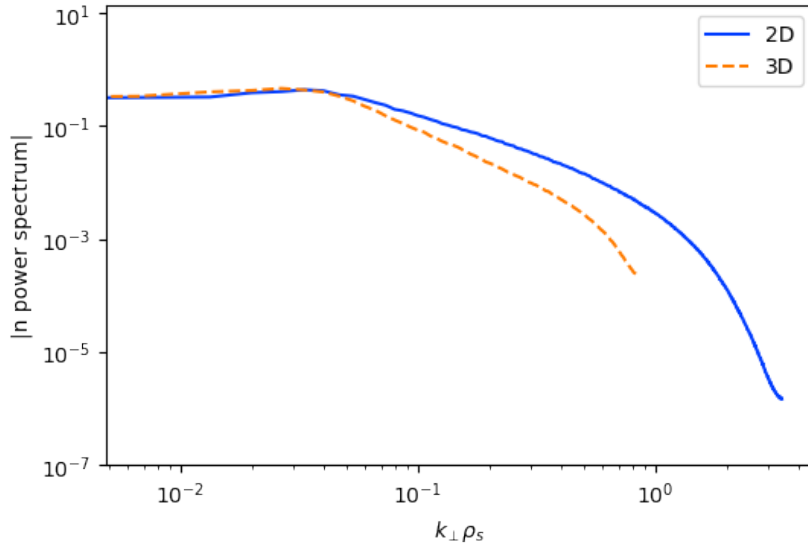


Figure 31: Power spectrum of density fluctuations at different spatial scales. In 2D the energy cascades to smaller scales before being dissipated.

Figure 31 shows that dissipative mechanisms remove power from the fluctuations at a smaller scale in the 2D simulation than in the 3D simulation. This observation motivated the choice to use substantially higher resolution in the 2D simulations, to verify that the cascade region was not distorted by the dissipation region. Nevertheless, appendix A shows that the choice of resolution in 3D does not significantly affect the overall results, implying that the location of the diffusion scale plays only a minor role. The temporal Fourier spectra (not shown) exhibits a similar trend: in 2D the activity extends down to smaller temporal scales.

It is not clear what causes this effect, or whether it is physically-relevant. As Garcia et. al. pointed out [139], a Fourier decomposition of the perpendicular scales in the vorticity equation (eq. (30) Garcia et. al. 2006) shows that the form of the parallel loss term affects the scales that are preferentially damped.

It is plausible that the parallel physics in the 3D model has the effect of damping at a scale above that of the dissipation scale in 2D, but this requires further investigation.

Parallel heat fluxes

The biggest systematic difference between the radial profiles in 2D and 3D is in the temperature profiles, so we now look at the cause of these differences in the form of the parallel heat fluxes.

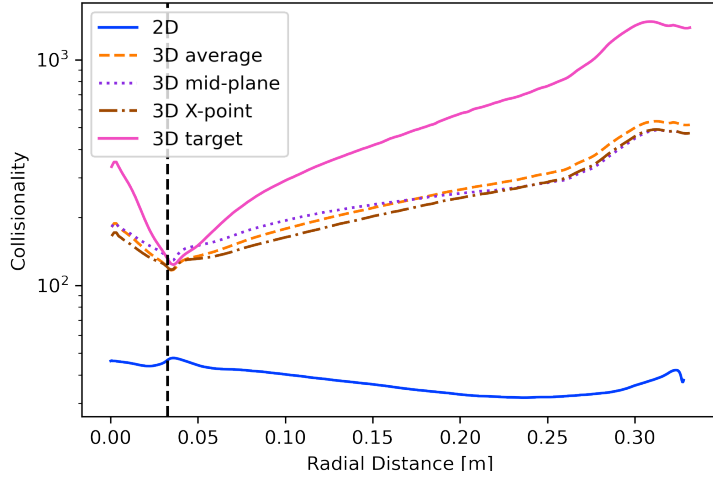


Figure 32: Average radial profiles of collisionality. Whilst the 2D simulations have $\nu^* \sim 35$ everywhere, the 3D simulations are much more collisional.

The collisionality can be estimated through equation (4.105) from Stangeby’s textbook[68]

$$\nu^* = 1.0 \times 10^{-16} \frac{nL_{\parallel}}{T^2}, \quad (5.2)$$

for n in m^{-3} , L_{\parallel} in m and T in eV. Figure 32 shows that in 2D the collisionality is high everywhere, which is due to the low temperature. The 2D parallel heat transfer is therefore very much in the conduction-limited regime (figure 33).

In the 3D models the average parallel heat flux is evaluated near the target in figure 34. The peak loss at a single target is $\sim 40\%$ larger than in 2D, which indicates the difference in radial temperature profiles in figure 29 is due to increased parallel heat transport at the same temperature rather than due to decreased radial transport. Decomposing the parallel transport into conductive and convective terms, again the conductive loss is smaller, which in 3D means the total loss is dominated by the convection. Therefore whilst in 2D the conduction is the limiting factor in parallel heat transport (compared to convection, see section 3.7.2), in 3D we have found that the convection is more significant instead.

The condition for the dominance of conduction over convection (and hence also for the validity

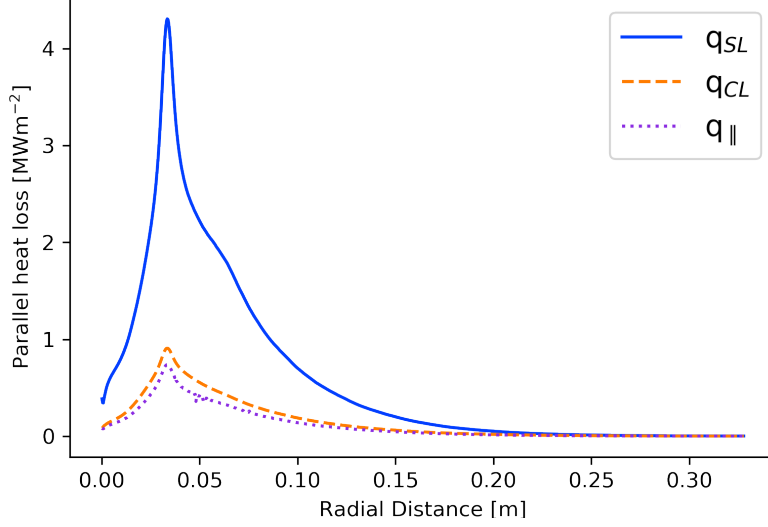


Figure 33: Average radial profiles of parallel heat flux in 2D. The harmonic averaging procedure in (3.146) means the total parallel heat flux in 2D, q_{\parallel} , is limited by the smaller value. Here q_{CL} is by far the smaller value, meaning this 2D simulation is in the conduction-limited regime. The radial location of the density and temperature sources is shown by the black dotted line.

of the standard two-point model [68]) can be estimated as

$$\kappa_{\parallel} \frac{T_{\text{up}}}{L_{\parallel}} \gg n T u_{\parallel}, \quad (5.3)$$

where T_{up} refers to the upstream temperature, which here we can replace with the temperature at the mid-plane.

Rewriting in terms of the parallel electron mean free path λ_{mfp} , the Mach number M , the sound speed c_s , and the electron thermal velocity $v_{\text{th},e}$ this becomes

$$v_{\text{th},e} \frac{\lambda_{\text{mfp}}}{L_{\parallel}} \gg M c_s. \quad (5.4)$$

Therefore in conjunction with the requirement to be in the collisional fluid limit ($\nu^* \gg 1$), the regime of validity of the two-point model (which assumes conduction dominates over convection) is a function of the local collisionality ν^* through

$$1 \ll \nu^* \ll M^{-1} \sqrt{\frac{m_i}{m_e}}. \quad (5.5)$$

In (5.5) the left-hand inequality is necessary to be in the fluid limit, and the right-hand inequality expresses convection being smaller than conduction.

In 3D, despite having the same total sources as in 2D, the lower temperature profile which emerges leads to a very high value of collisionality, shown in figure 32. Figure 32 shows that $\nu^* > 100$ everywhere in 3D, completely violating the right-hand inequality in (5.5). This explains the presence of both significant convective as well as conductive heat loss in the 3D simulations.

Conventionally the dependence on Mach number M is removed from (5.5), because at the target the Bohm conditions normally imply $M = 1$. However, in this case the supersonic flow near the target allows $M \sim 2$ (see section 5.4.2), making the value of collisionality where convection becomes comparable to conduction a factor of two lower again than it would be otherwise.

Overall this means that despite choosing sources to be consistent between simulations, and values representative of the MAST SOL, the results are not in the regime of validity expected: in 2D the conduction dominates but the conventional assumption of negligible convection is not well-justified, and in 3D convection dominates significantly.

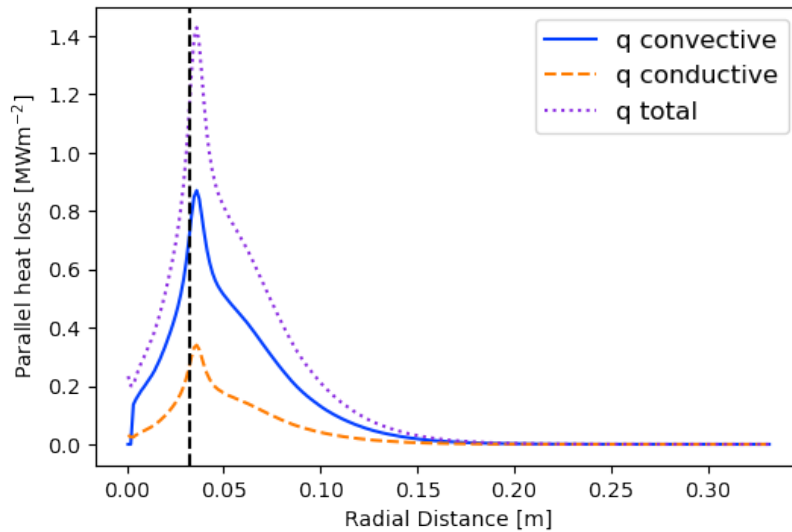


Figure 34: Average radial profiles of parallel heat flux in 3D, through a single target. The parallel transport is in a convective regime.

5.4.2 Varying divertor leg length

The parallel connection length is a key parameter in SOL physics, which enters at first order in the 2D parallel loss terms, and sets the domain size in 3D. However it is not always obvious what numerical value to use for the parallel connection length in 2D - some models use the physical length of the field-line from mid-plane to target, whilst others instead use a value

intended to represent the characteristic parallel length of field-aligned structures[222]. We therefore treat this as a sensitivity parameter.

In 3D we compare 3 simulations with the same sources but different length divertor legs, the intention being to determine which lengths agree or disagree with 2D simulations with the same connection length. The length of the leg beyond the X-point is alternatively doubled and halved relative to the baseline simulation, creating three domains with a respective L_{\parallel}/L_S ratio of $\{3, 2, 1.5\}$, where the size of the source region L_S is fixed.

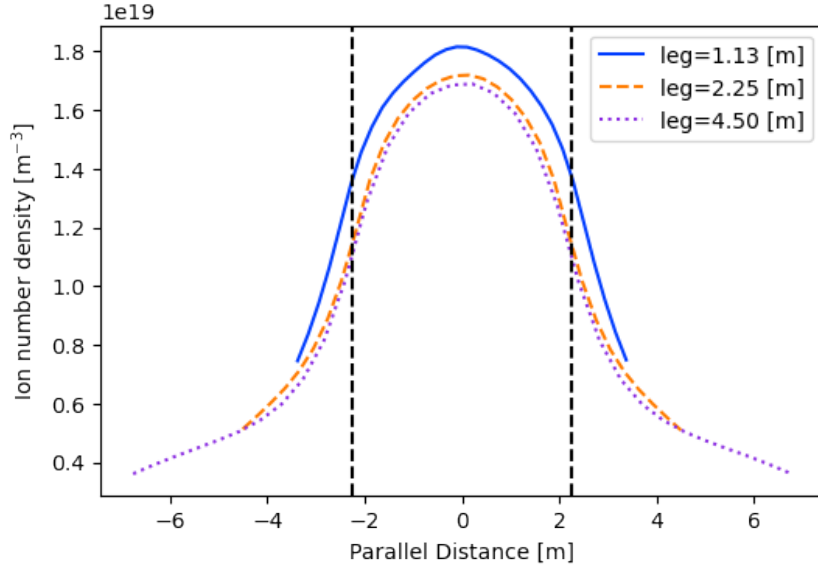


Figure 35: Parallel profiles of density for 3D simulations with differing divertor leg lengths, averaged over time at radial position of 6cm (close to the particle source). The length of the leg does not significantly affect the density at the mid-plane, or the overall profile.

Figure 39 shows that the parallel velocity reaches sonic speeds before the target in all cases. This result might at first appear to be inconsistent with standard nozzle theory, which derives the parallel gradient of the plasma Mach number to be (as shown in section (1.8.2.3) of [68])

$$\frac{dM}{ds_{\parallel}} = \frac{S_n (1 + M^2)}{nc_s (1 - M^2)}. \quad (5.6)$$

However in our case $M = 1$ would not correspond to a singularity in the Mach gradient because we also have $S_n = 0$ at the same location ($S_n = 0$ anywhere past the “X-point” by assumption in our geometric setup). The mach-gradient relation 5.6 arguably still rules out this sonic transition in the source region. (The model used to derive is isothermal, unlike our model, but figure 37 shows that the temperature only drops by $\sim 25\%$ from the mid-plane to the sonic region.)

Supersonic flow is expected in the system being studied here. The parallel conduction of

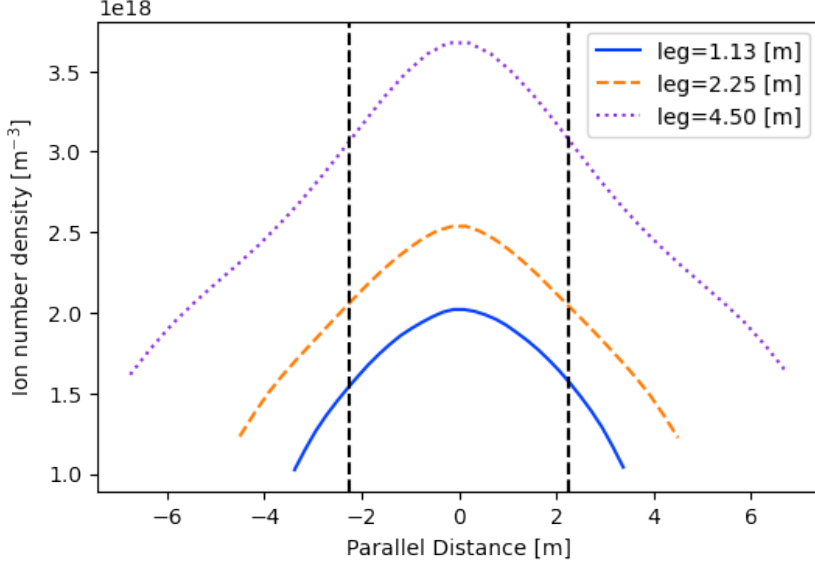


Figure 36: Parallel profiles of density for 3D simulations with differing divertor leg lengths, averaged over time at radial position of 15cm (in the far SOL). The length of the leg does not significantly affect the overall profile, but the densities are separated due to the different overall radial decay lengths. Therefore the shorter leg is allowing higher particle flux into the target and out of the domain.

heat causes a temperature drop along the parallel direction, which lowers the local sound speed. Meanwhile the density also drops away from the mid-plane density source. Therefore an increasingly rarefied and cold plasma accelerates away from the mid-plane. This model includes no momentum exchange terms to stop this flow from accelerating to supersonic speeds. That the inclusion of momentum exchange terms is necessary to avoid cold supersonic flow is expected given that the plasma fluid has no way to exchange parallel momentum because parallel viscosity is neglected, there are no neutral collisions, and no charge exchange. This been noted before in 1D modelling of detachment onset, such as with SD1D[134].

Another valid interpretation of this phenomenon is that whilst the spatially-varying parameter S_n is explicitly set to zero beyond the X-point, cross-field transport between flux tubes creates an effective particle sink, which is what is actually represented in the 1D model used to derive (5.6). This sink makes the effective S_n negative, so that even with $M > 1$ past the X-point the plasma continues to accelerate supersonically. As Ghendrih et. al. [223] describe, “when this particle sink prevails from the X-point region towards the target plate, one finds that transitions to supersonic flows will occur, the bifurcation point being in the vicinity of the X-point”.

This phenomenon then takes the dynamics further into a high collisionality regime, by in-

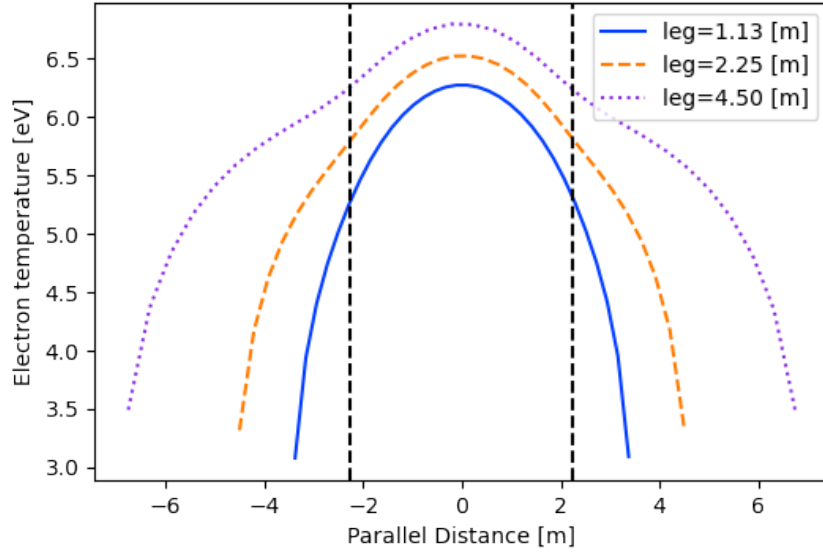


Figure 37: Parallel profiles of temperature for 3D simulations with differing divertor leg lengths, averaged over time at radial position of 6cm (close to the energy source). Whilst the temperature is peaked at mid-plane, most of the temperature loss occurs in the last 1m before the target, regardless of leg length.

creasing M in (5.4.2), making the assumption that parallel thermal transport is only through conduction increasingly invalid.

This indicates a clear avenue for future work: a similar domain setup but with a density source in the divertor should prevent supersonic parallel flows, whilst imitating a high-recycling regime. It would therefore be closer to an experimental reactor-relevant regime, and also include more of the key neutral effects identified as being important in 1D studies (such as [197]). The challenge of this model experiment would be in either (1) deciding what shape & size the sources should be without introducing too many arbitrary assumptions, or (2) choosing the simplest possible neutrals model that can satisfactorily model the recycling in the divertor. A starting point for (1) might use a divertor source with a radial exponential decay length set to the typical mean free path of ions before neutralisation.

5.4.3 Sensitivity to parameters in 2D

We also tested the sensitivity of the 2D results with a simple parameter scan, alternately doubling or halving (a) the magnitude of all the parallel loss terms, (b) the magnitude of the particle source term, and (c) the magnitude of the energy source term. The aim was to assess whether the effect on the profiles was linear with changing parameters, and to see if a regime of closer agreement with the 3D models existed. For each change ((a),(b), or (c)), we

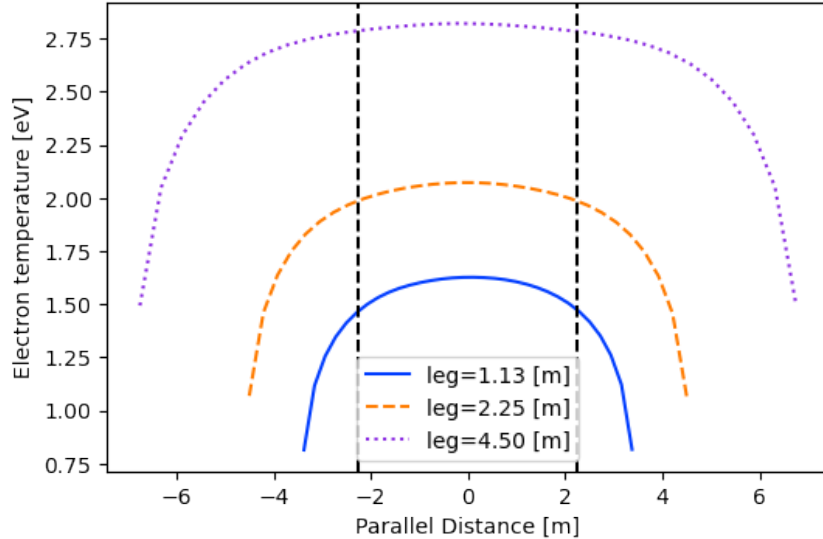


Figure 38: Parallel profiles of temperature for 3D simulations with differing divertor leg lengths, averaged over time at radial position of 15cm (in the far SOL). The temperature is mostly constant along parallel direction (figure 38) - the drop occurs in a small region in front of the target.

looked at the effect on the time-averaged radial density and temperature profiles, for both the absolute value and the shape (by normalising to the maximum value). Whilst we will now describe the results for all these cases, we will only show the profiles for the cases which displayed some form of non-trivial or unexpected result.

Doubling or halving the magnitude of all parallel loss terms in 2D increases or decreases the average density profiles at all radial locations, as expected. It also changes the temperature profiles, but in a way which leaves the maximum value fixed, whilst altering the decay lengths (figure 41). Therefore the magnitude of the loss terms cannot be used on its own to tune the 2D simulations to match the 3D results in both density and temperature because increasing the losses (equivalent to a shorter L_{\parallel}) will depress the density profiles as well as the temperature decay lengths, and the temperature profiles do not change their absolute value so will not match either.

Altering the magnitude of the density source terms has a larger effect on the density profiles than changing the size of the loss terms does, with the absolute height of the profiles varying almost linearly with the density sources. When normalised, the profiles are coincident, so there is no change the the decay length, as expected. The temperature profile scales inversely with the size of the density source, which is expected because the same energy has been distributed amongst twice as many particles in the same time period. However, increasing

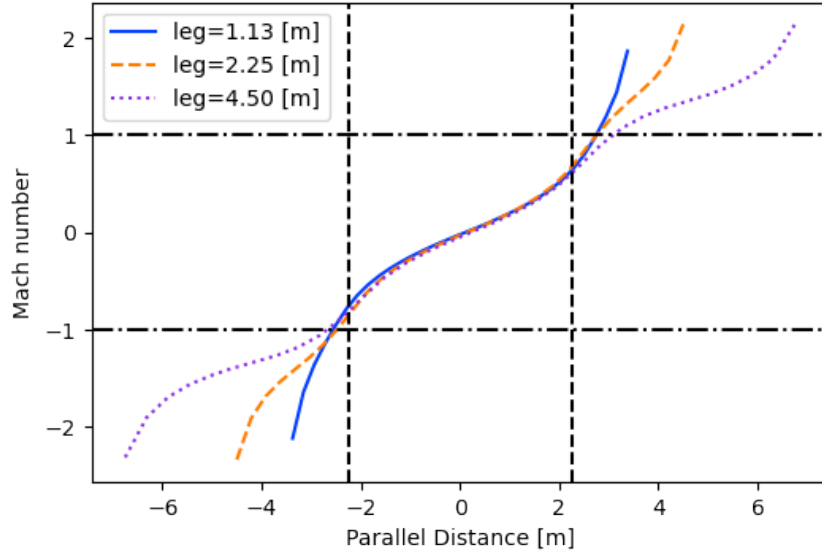


Figure 39: Parallel profiles of mach number for 3D simulations with differing divertor leg lengths, averaged over time at radial position of 6cm (close to the particle source). The length of the leg does not significantly affect the overall profile. A transition to supersonic flow can be seen in all simulations, which occurs in the divertor leg beyond the "X-point".

the density sources also broadens the normalised temperature profile, shown in figure 42.

Scaling the energy source terms causes the absolute value of the temperature profile to vary linearly as expected, but changes the normalised shape of the profiles (figure 43), with smaller energy input creating broader profiles. Therefore, as the 2D temperature profile is broader than the 3D one, and scaling the energy sources does not change the shape, the discrepancy between the 2D and 3D temperature profiles cannot be resolved by simply scaling the energy sources in 2D. The density profile scales inversely with energy source (figure 44), but with no change to the normalised shape.

Since decreasing the energy source brings the absolute temperature closer to the 3D profile but makes the 2D density increase, we also tried decreasing both the density and the energy source terms (again by a factor of 2). We found that whilst the temperature profiles now matched 3D, the density profile was everywhere lower.

We conclude that over a range of a factor of 4 changing the magnitude of the loss and source terms in the 2D simulation is not sufficient to easily recreate the average 3D profiles of both density and temperature simultaneously.

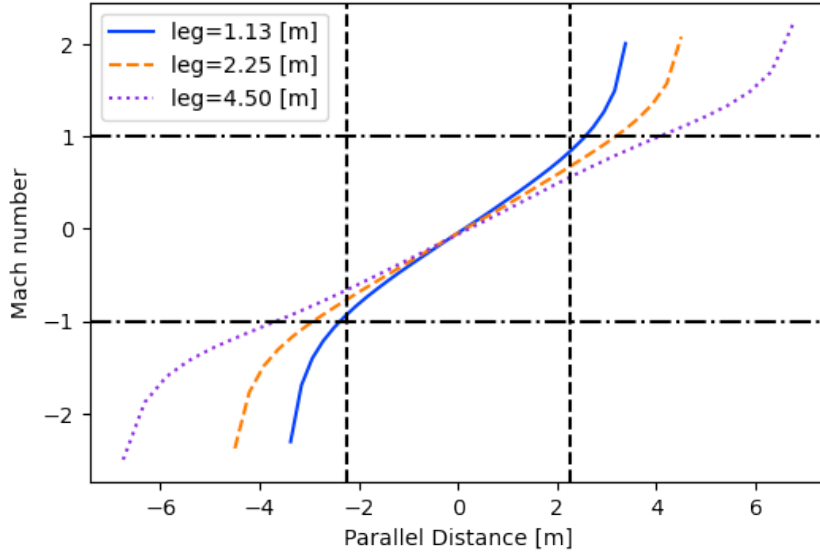


Figure 40: Parallel profiles of mach number for 3D simulations with differing divertor leg lengths, averaged over time at radial position of 15cm (in the far SOL). The length of the leg does not significantly affect the overall profile. A transition to supersonic flow can be seen in all simulations, which occurs in the divertor leg beyond the “X-point”.

5.5 Conclusions

We have taken a first-principles approach to evaluating the approximations used to truncate SOL turbulence models to 2D, comparing the 2D case with 3D simulations set up so as to form the closest possible analogues of the 2D models

The 2D model successfully replicates the mean density profile of the 3D models with matched sources and no parameter tuning. The 2D model also reproduces the fluctuation statistics of the 3D model well, and the results are robust to changing the length of the divertor leg in 3D or the source and sink sizes in 2D.

One systematic difference was a broadening of the mean temperature profile in 2D compared to in 3D. The reason for this difference is an interplay of issues caused by two reasonable-seeming assumptions in the model setup. In particular, in very high collisionality conditions, the assumptions used to close 2D models are not valid, because high enough collisionality suppresses thermal conduction so that convection becomes important. Further, the source setup used in the parallel direction for the 3D simulations causes supersonic flows beyond the X-point, which make the thermal convection compete with conduction at lower collisionality than would otherwise be the case. Since this highly supersonic flow is not typically observed in experiments, we suggest that future work always include particle sources in the divertor

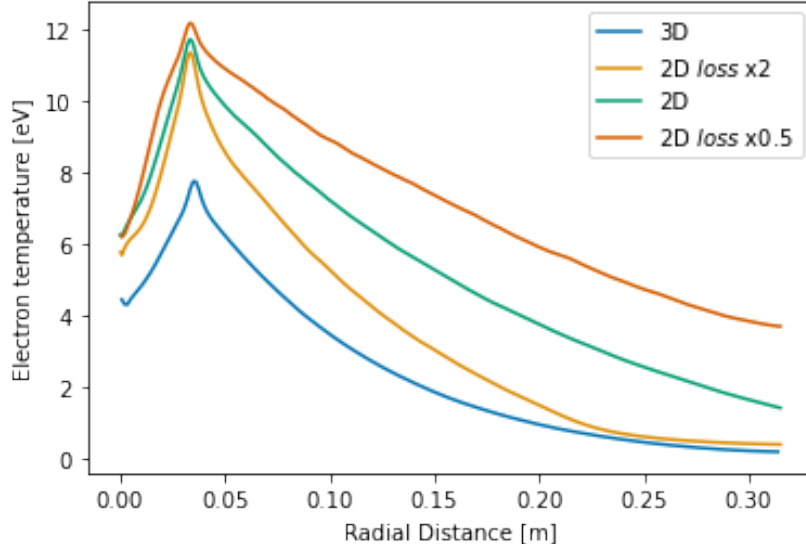


Figure 41: Alternately doubling or halving the magnitude of the parallel loss terms (n_{loss} , Ω_{loss} , T_{loss} in (3.127) - (3.129)) scaled the density profiles proportionally everywhere as expected (not shown), but changed the decay length of the temperature profiles without altering their maximum value. Therefore scaling the loss terms by a overall constant factor cannot create agreement with the 3D profiles in both density and temperature.

leg.

Finally, we examined the effect of altering the magnitude of source and sink terms in 2D, and conclude that they cannot easily be used to recreate both the density and temperature profiles observed in 3D simultaneously.

The good qualitative agreement between these two types of reduced models provides a basis for interpreting 2D and 3D models relative to one another, our results also motivate future work. Our results open up avenues for future work moving the 3D models step by step towards more detailed representations of tokamak divertors, in particular using a larger power source (to obtain a higher temperature and hence lower collisionality) and a divertor density source (to keep the parallel flows subsonic), would provide a more consistently analogous system.

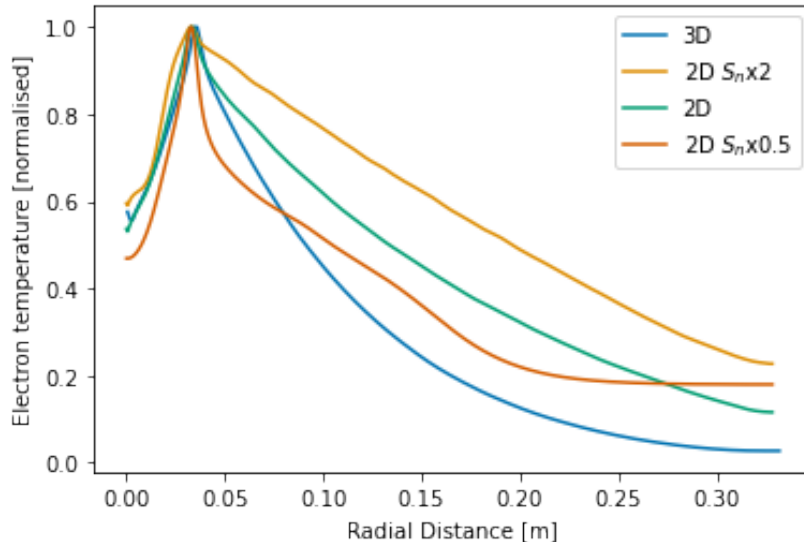


Figure 42: Altering the density source S_n by a factor of 2 scaled the density profiles linearly at all locations (not shown), but also altered the shape of the normalised temperature profiles relative to their maximum value.

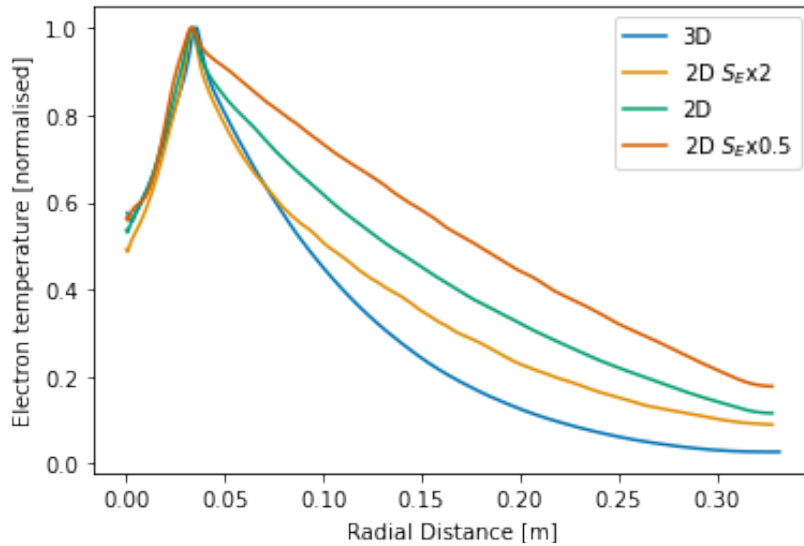


Figure 43: Scaling the energy source S_E by a factor of 2 scales the absolute value of the temperature profiles linearly as expected (not shown), but also has the effect of broadening the temperature profiles.

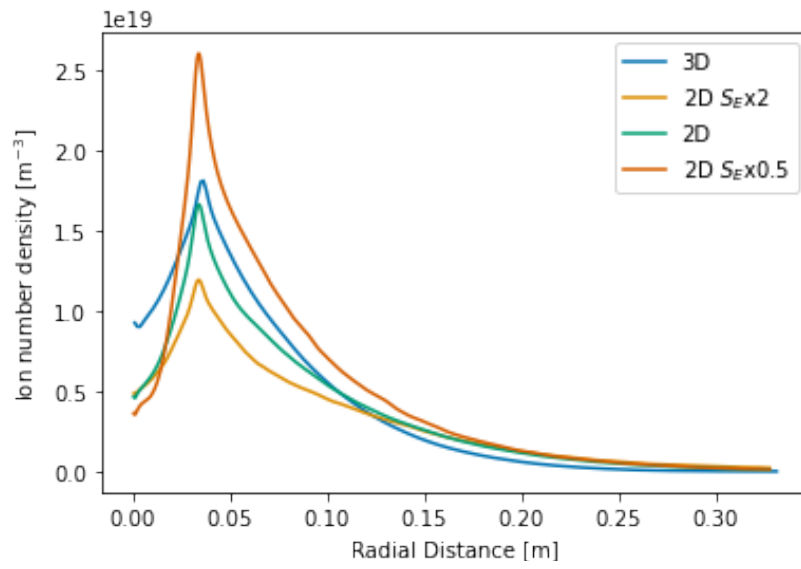


Figure 44: Scaling the energy source S_E by a factor of 2 scales the absolute value of the density profiles inversely.

Chapter 6

Including a Core Region in 2D models

6.1 Introduction

In this chapter we motivate and then present an extension of the model used in the previous chapter, which adds a new region which represents the presence of the core immediately on the inboard side of the scrape-off layer region. We show that within certain parameter regimes strong spontaneous zonal-like flows can occur, which present a considerable challenge for producing experimentally-relevant simulation results. We analyse this behaviour as a function of input parameters, and compare it to similar behaviour seen in related 2D neutral fluid systems. Finally we compare a few different approaches which modellers can use to circumvent this problem.

6.2 Motivation of Coupled Core-SOL Modelling

There are multiple reasons why a coupled model which includes a description of both the core, SOL, and the interaction between them, is desirable.

In the filamentary view of SOL turbulence there is evidence that filaments are born in a shear layer near the inside of the separatrix, and then travel outwards into the SOL[87]. Capturing this layer requires some model of the core dynamics.

The turbulence in the SOL is saturated once it displays a steady state in its statistical properties, but does not necessarily have all the characteristics that saturated neutral fluid turbulence typically displays. In theoretical turbulence studies in neutral fluid dynamics it is common to consider a system driven at a certain spatial scale, in which the injected kinetic

energy is only removed once it has cascaded¹ down (or up, in the case of 2D systems) to a different scale at which it is removed through dissipation[226]. This approach requires that a saturated state is created where turbulent structures exist in the domain for long enough to reach the removal scale. In the core this assumption is reasonable, and means that analysis of the resulting spectra of kinetic energy can display various power law “cascades“ (e.g. [227]). However in the SOL the turbulent structures interact and fragment, a process which may be slower than their removal due to parallel losses. A valid question therefore is whether or not the turbulence crossing the separatrix retains any features of the core turbulence, or whether there is no “memory” of the mode structure in the core. It is also possible that the structures’ amplitude and extent are dictated by the behaviour in the core, but their ejection rate is independent of it.

A coupling also allows for modelling modes which extend across the separatrix itself, and also to potentially investigate any feedback of changes to SOL physics on the edge and core behaviour.

Even if none of these couplings matter, that in itself would be an interesting result, because it would imply that the fluid dynamics of the SOL are independent of the core.

Practically, for systems with large parallel losses, a source-driven simulation does not have a clear enough separation between the profile created in the immediate region of the (unphysical) source term and the resulting extended SOL profile. Adding a core-like region allows arbitrary space between the source and the SOL, avoiding this interpretation issue.

6.3 Setup and Domain Geometry

For this chapter the choice of domain setup is relatively similar to the previous chapter, concentrating on 2D source-driven drift-plane models with a rectangular geometry. The difference between this geometry (shown in figure 45) and the one depicted in figure 26 is the addition of a “core” region on the inner side of the domain, which is distinguished purely by

¹Here “cascade” has a specific meaning, referring to a situation in which turbulent structures are present at a range of spatial scales, with no scale dependence in the governing equations within that range. This leads to an equilibrium where the rate of energy transfer between scales (conventionally denoted ϵ) is constant, and is matched by the rate of energy dissipation at a fixed terminal scale. In an ideal situation the energy transfer rate can be inferred by fitting to the variation of kinetic energy density with scale, or more directly calculated via a Yaglom law. Such a law relates the third order structure function (which is a statistical moment of the distribution of the difference between flow velocities at two different nearby points in the flow) to the energy transfer rate. [224, 225] However, this calculation is beyond the scope of the work presented here.

using different closures for the parallel physics than are used in the “SOL” region. This is achieved by having the parallel loss terms be a function of radial position, and the point (or thin region) at which they change behaviour defines the “separatrix”.

Again, a source-driven setup is used, motivated by a conceptual model of the plasma in which particles and energy travel outwards through the core, across the separatrix, and down the magnetic field to the targets in the SOL.

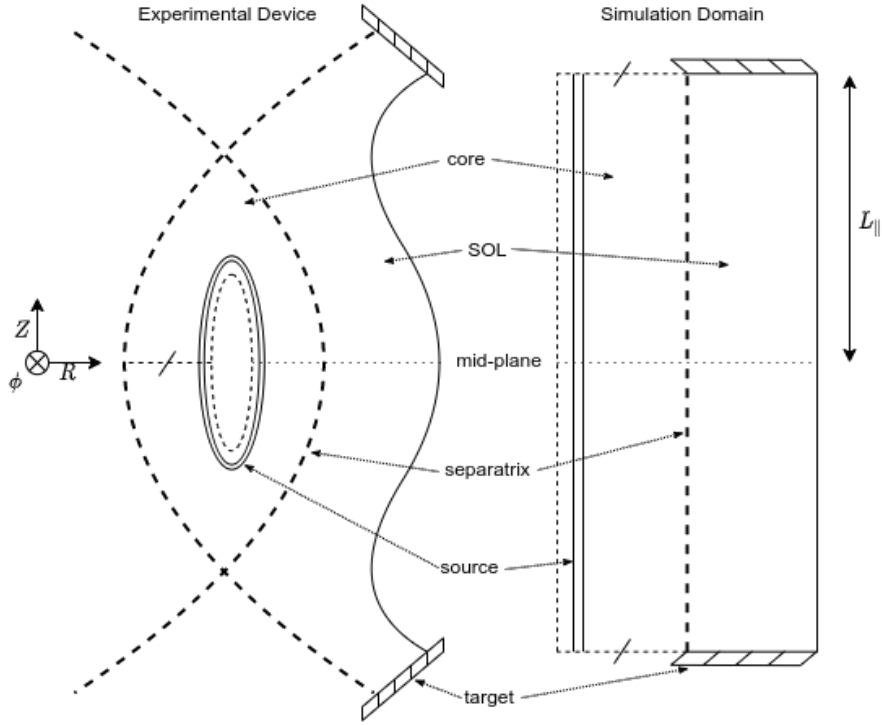


Figure 45: Schematic diagram of relationship between the simplified 3D simulation domain and the full experimental device geometry. This geometry differs from 26 through the addition of a core region on the inboard side, which is modelled as a doubly-periodic cuboid, and encompasses only the outer part of the core region. The basis set of vectors (R, Z, ϕ) denote the radial, vertical and toroidal directions in the experimental domain, but are aligned along the radial, parallel and binormal directions in the simplified simulation domain. Within the core, the parallel direction is periodic. The 2D simulation domain here corresponds to a plane into the page located at the mid-plane, and 2D simulations which include a core are the focus of this chapter.

The numerical domain for the 2D simulations used in this chapter spans $\rho_s = 400$ in the radial (x) direction and $\rho_s = 150.0$ in the binormal (z) direction (i.e. $L_x = 400$ and $L_z = 150$ in normalized units). A resolution is used that is comparable to the resolution used for the 3D drift-plane in chapter 5, specifically the domain is resolved with 480×256 grid points. The

separatrix is located at the 200th grid point, which corresponds to $L_x = 166.7$ in normalised units.

All other parameters, such as the magnetic field strength were kept the same as in table 3, with the exception of the diffusion coefficients, which will be discussed.

6.4 Problem of Unphysical Flow Generation

The simplest representation of a core region is to assume that the parallel transport is so large that the plasma parameters are homogeneous in this direction, so no net parallel loss occurs, and hence $n_{\text{loss}} = T_{\text{loss}} = \Omega_{\text{loss}} = 0$. This simple approach has been used in previous publications to represent a core region, for example in [179].

However, in the particular setup we used this displays a problem: over time the average value of the electric potential in the core starts slowly dropping, continuing until it reaches values which depend on the parameters, but can be as high as $10\text{-}20\times$ the typical size of potential fluctuations in the SOL (equivalent to several hundreds of Volts).

As an example of this problem, figures 46 to 48 show the results of running a typical simulation as described in section 6.3. Figure 46 shows the typical spatial structure of such a potential drop in the drift-plane, for a simulation that has been run for $\sim 0.1\text{ms}$.

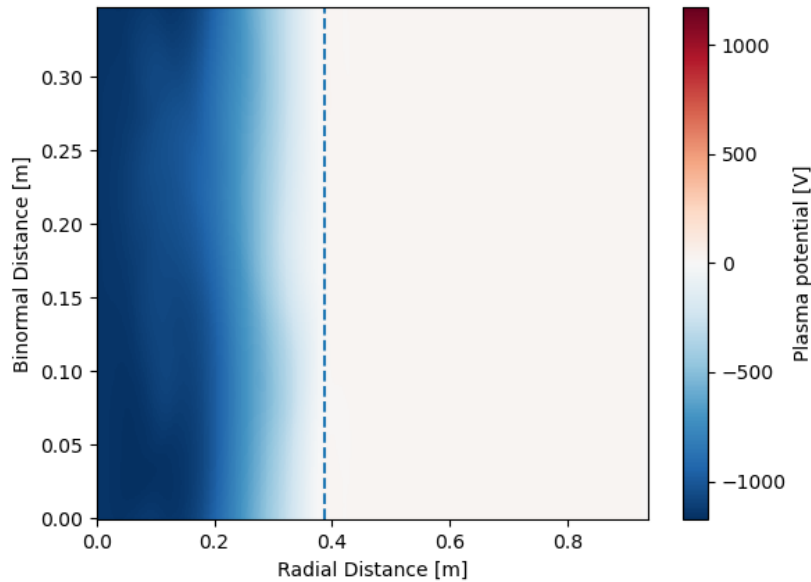


Figure 46: A typical 2D simulation including a core region (everywhere to the left of the dashed line). A persistent and unphysically-large drop in the electric potential is observed in the core region.

We can chart the development of this structure over time - figure 47 shows the mean value

of the potential across the entire core region as a function of time.

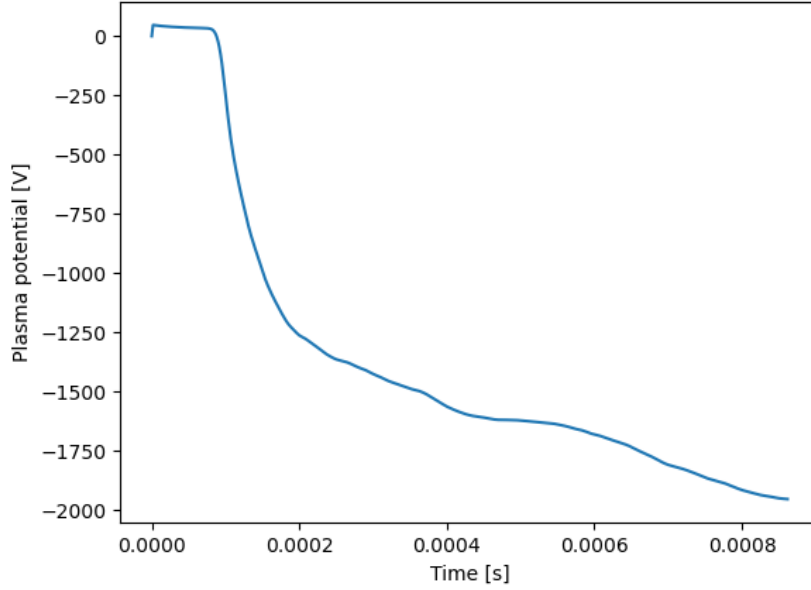


Figure 47: The spatially-averaged core potential drops over time.

As the potential in the SOL is effectively pinned to be close to the temperature through the sheath loss term, the localised change in potential in the core implies large radial electric fields have been created. Through Laplace’s equation (4.3) and the definition of the vorticity (3.113), a gradient in the radial electric field is equivalent to a radial shear in the binormal component of the $\mathbf{E} \times \mathbf{B}$ flow velocity:

$$\frac{\partial^2 \phi}{\partial x^2} \propto \frac{\partial \mathbf{u}_{E_x}}{\partial x}. \quad (6.1)$$

This radial shear becomes extremely strong, dominating the shape of structures in the core region (as seen in the case of the temperature in figure 48).

This presents a problem: despite choosing a set of seemingly-reasonable physical assumptions in our simplified model, we have obtained a result which does not correspond to the steady-state SOL turbulence observed in reality. We have also added nothing to the 2D SOL-only model used in chapter 5, we merely removed the loss terms over a portion of the domain. These specific simulations appear to be unable to obtain a statistical steady state that does not exhibit unphysically-large shear flows in the “core”, making them unsuitable for statistical analysis, comparison to a 3D model, or comparison to experiment, at least without some further modification.

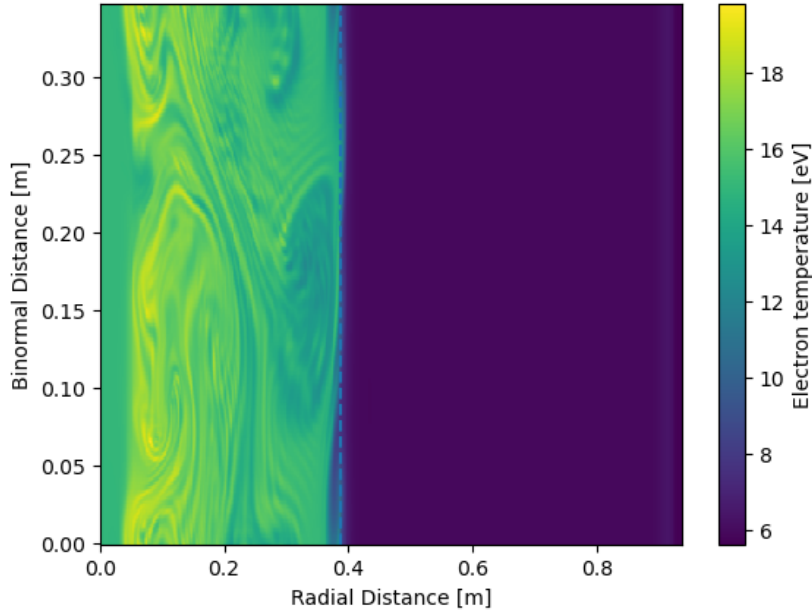


Figure 48: A typical 2D simulation including a core region (everywhere to the left of the dashed line). An unphysically-large drop in the electric potential causes huge binormal flow shear in the advected variables, for example in the electron temperature shown here.

6.5 Alterations not affecting mean flows

Various alterations were made to the system and setup to try to achieve a saturated state of turbulence without strong mean flows in the core.

6.5.1 Boundary Conditions

The simulation shown in figures 46 - 48 has a Neumann boundary condition on the electric potential at the inner radial boundary. This is consistent with the approach in chapter 5, in which ϕ is fixed on the outer radial boundary but the absolute value is not constrained on the inner boundary.

If we instead use a Dirichlet condition on ϕ to fix its value on the inner boundary, the mean flows still develop, they are merely confined to the centre of the core region, as shown in figure 49. Figure 49 also shows that the potential reaches more extreme values when the inner boundary is not constrained.

6.5.2 Loss Terms

Changing the exact form of the loss terms appears not to affect the development of the flows in the core either. Specifically using the “sheath dissipation” closure rather than the

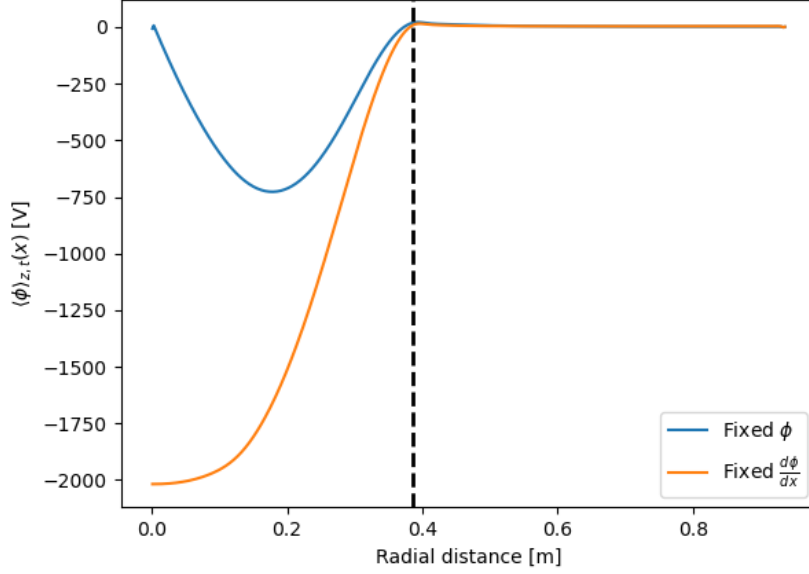


Figure 49: Radial profile of electric potential for different inner radial boundary conditions. Using a Dirichlet boundary condition on the inner radial boundary fixes the value of the potential, but does not prevent the generation of binormal flows.

“heuristic“ closure described in 3.7 does not affect the core potential significantly, and neither does arbitrarily increasing the magnitude of the vorticity loss term in the SOL by a factor of 10.

6.5.3 Relaxing the Boussinesq approximation

We suspected that the radial electric field in the core might be the product of the Boussinesq approximation violating charge conservation. To relax this approximation, the vorticity is replaced with an alternate generalised vorticity

$$\bar{\Omega} = n \nabla \cdot \nabla_{\perp} \phi + \nabla_{\perp} n \cdot \nabla_{\perp} \phi, \quad (6.2)$$

whose definition does not require neglecting density fluctuations like we assumed in (3.112). As well as changing the definition of the vorticity by a factor n , this alteration also requires the addition of a term

$$-\left\{ \frac{|\mathbf{v}_E|^2}{2}, n \right\} \quad (6.3)$$

to the vorticity equation (3.114) (and hence (3.128) in 2D), where $\mathbf{v}_E = |\nabla \phi|$. However, the mean flows still developed in a similar way.

6.6 Effect of dissipation coefficients

One significant choice of input parameters are the value of normalised perpendicular diffusion coefficients. As any diffusive processes transports particles, momentum, and energy, there are corresponding perpendicular diffusion coefficients for density (D_n), vorticity (μ_Ω), and temperature (κ_\perp).

These coefficients are defined for so-called *classical* diffusion through equations (3.90) - (3.92), and for so-called *neoclassical* diffusion through equations (3.93) - (3.95), which are related to the classical expressions through a quadratic dependence on the edge safety factor q (itself defined by (3.96)). In chapter 5 we used the (lower) classical values everywhere in the SOL, in both 2D and 3D. However differences of opinion do exist within the community on whether classical or neoclassical values should be used in the SOL - for example Fundamenski[161] argues in favour of using neoclassical values instead. (The reality will likely be somewhere in between the two extremes.)

This choice can make a large difference to the value, especially for machines with a large edge safety factor, such as MAST. For example the difference between using a classical value (corresponding to $q = 0$), a neoclassical value of $q = 3$ typical of DIII-D, and a neoclassical value of $q = 6$ typical of MAST corresponds to density diffusion coefficients approximately either $1\times$, $13\times$, or $48\times$ larger than the classical value. In our simplified slab geometry q basically does not enter the model anywhere else, meaning that using a high value of q with neoclassical expressions corresponds to increasing the diffusion coefficients independent of any other change to the system.

In practice, there are numerical stability difficulties with resolving highly nonlinear turbulence simulations. Grid-scale fluctuations can cause the solver to “blow up”, in which the adaptive timestep reduces to an extremely small size, and forward progress becomes limited by the value at a single cell. It is therefore common to arbitrarily choose to use higher values of diffusion than classical ones, but this is not always well-justified (see for example [5]). The existence of neutrals and impurities in the real SOL will increase the collisional diffusion coefficients, but deriving a specific value is challenging. There is also an argument sometimes used that diffusion coefficients might as well be chosen large enough to damp out turbulent activity below the scale of the Larmor radius, because below this scale the drift-reduced equations are not applicable anyway.

To investigate the impact dissipation coefficients on the formation of these mean flows, we ran the coupled core-SOL 2D simulations over 3 decades of density diffusion and viscosity,

spanning classical & neoclassical MAST values. For reference, classical values for MAST can be found in table 4 in chapter 5.

6.6.1 Onset at low dissipation

As a diagnostic variable for determining the presence or absence of mean core flows, we can use the binormally-averaged binormal component of mean kinetic energy ($\langle K_z \rangle_z = \langle v_z^2 \rangle_z$) as a function of time. This quantity is then averaged over the entire core region before plotting, and hence shows the total magnitude of the binormal flows in the core (as it will be a positive quantity regardless of whether the potential dropped or rose on average).

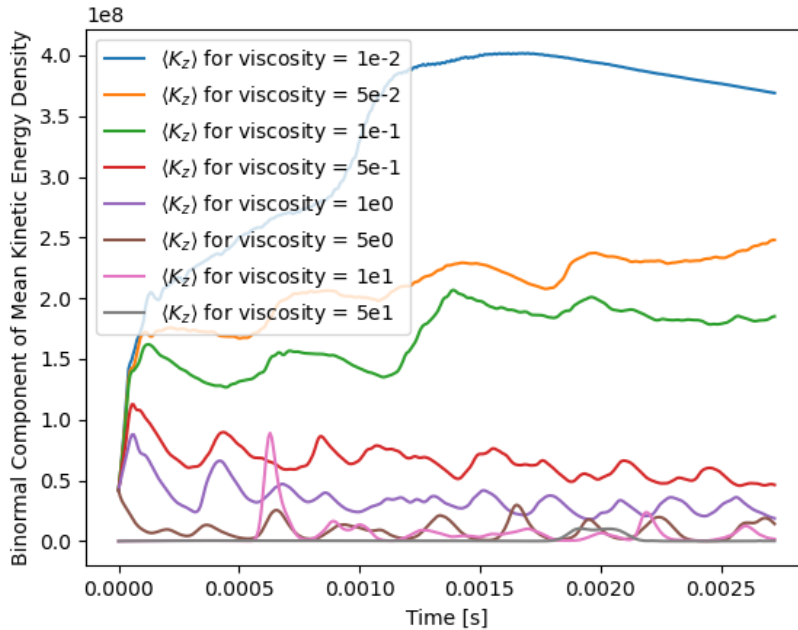


Figure 50: Binormal component of mean kinetic energy ($\langle K_z \rangle_z = \langle v_z^2 \rangle_z$) averaged over time and over radial position in the core, for a range of different values of core viscosity coefficient μ_Ω . A broadly monotonic increase in the average strength of the binormal flows with decreasing viscosity is observed.

Figure 50 shows the effect of varying the viscosity coefficient whilst holding the diffusion coefficient constant (held at a normalised value of 0.01). A broadly monotonic increase in the average strength of the binormal flows with decreasing viscosity is observed.

The effect of altering the density diffusion coefficient in the core was also tested. Figure 51 shows that (for viscosity coefficient fixed at 0.01) below $D_n \sim 0.01$ the binormal flows are far stronger, and below $D_n \sim 0.005$ they begin oscillating in strength. For values of diffusion above 0.05 the mean flow is both small and stable over time.

This indicates a distinct bifurcation in core ϕ stability, being stable only above a threshold value of diffusion. The threshold value of density diffusion is comparable to the neoclassical value for MAST (~ 0.01 for $q = 6$), which means it is possible that previous studies of MAST SOL which used neoclassical values were only just in the regime of stability.

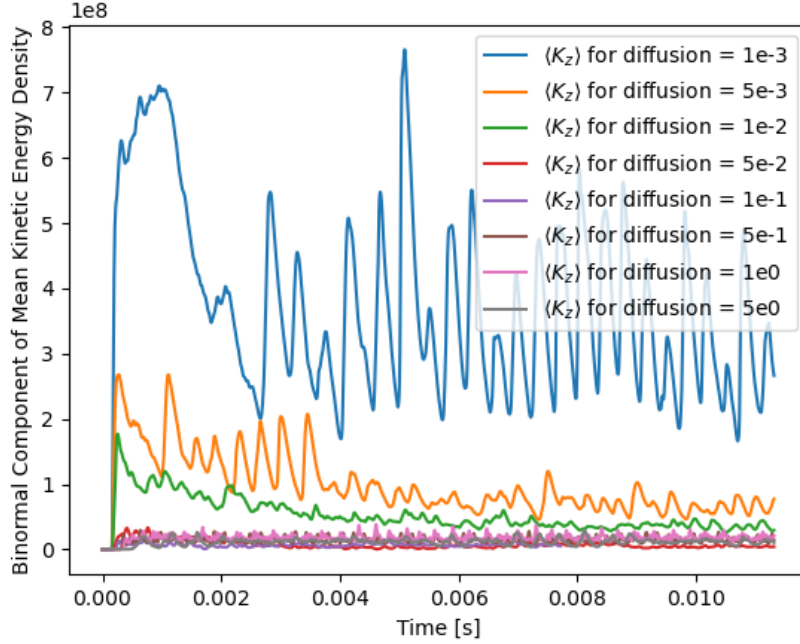


Figure 51: Binormal component of mean kinetic energy ($\langle K_z \rangle_z = \langle v_z^2 \rangle_z$) averaged over time and over radial position in the core, for a range of different values of core diffusion coefficient D_n . Below $D_n \sim 0.01$ the binormal flows are much stronger, and below $D_n \sim 0.005$ they begin oscillating in strength.

6.6.2 Variation of profiles

The strength of these mean flows in the core affects radial transport, which affects averaged density and temperature profiles, so we now discuss the variation of time-averaged density and temperature profiles as a function of diffusion and viscosity.

The mean density profile varies considerably in the core, as a function of diffusion (figure 52) and of viscosity (figure 54). In both cases the mean density is generally higher for lower values of dissipation. The density profiles in the core vary much less than those in the SOL, so there is some degree of insensitivity to the core. However the profile height still varies by a factor of 3 or more in the SOL. The trend of increasing diffusion creating shallower SOL density profiles is reversed for varying viscosity.

The temperature profiles are much less sensitive to either diffusion (figure 53) or viscosity

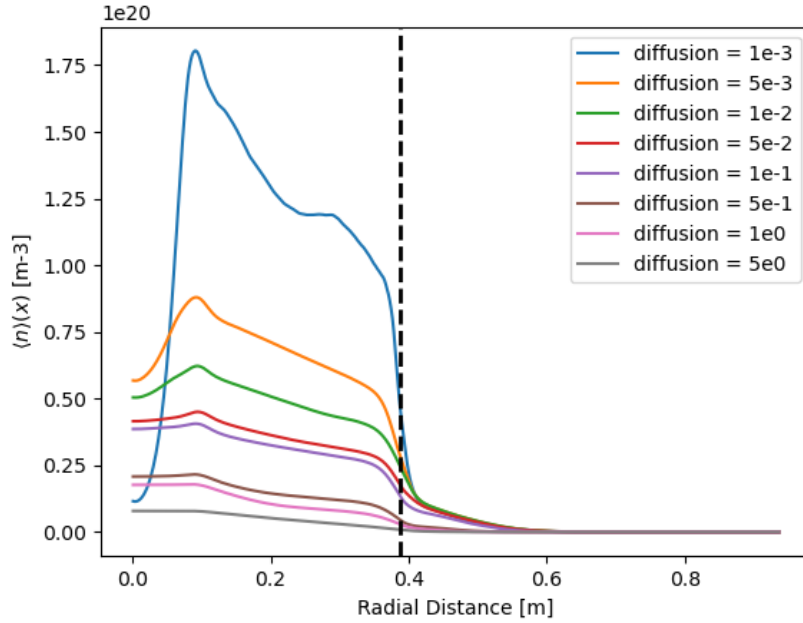


Figure 52: Mean core-SOL density profiles as a function of core diffusion. Varying the diffusion coefficients in the core causes the mean density in the core region to vary by more than a order of magnitude, growing with decreasing diffusion. The mean profiles in the SOL also vary considerably, but very steep profiles near the separatrix reduce the variation relative to the core.

(figure 55). There is still a general trend of decreasing dissipation coefficient creating a higher mean profile in the core, but the variation is much smaller than it is for density in the core. This might mean that there is still considerable diffusive energy transport radially even when convective transport is cut off by the mean flows. Temperature profiles in the SOL vary little for changing diffusion, except for a shoulder-like formation in the near SOL, which is present only for diffusion coefficients < 0.1 .

Overall, we see that the effect of core diffusion and viscosity on both core and SOL profiles cannot be neglected, even whilst holding SOL dissipation coefficients constant. This is especially the case for density profiles, which can vary considerably. However it is also interesting that very large variations in the core profiles make a comparatively small difference to the SOL profiles.

6.6.3 “Bursting Convection” Regime

The oscillations in figure 51 show that for a certain range of parameter values it is possible to observe an interesting state of the turbulence: “bursting convection”. In this state the

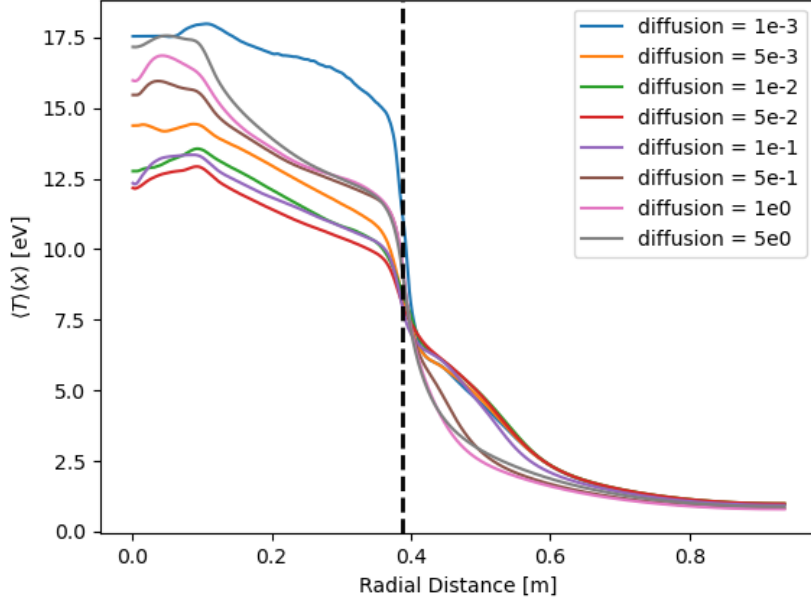


Figure 53: Mean core-SOL temperature profiles as a function of core diffusion. Varying the diffusion coefficients in the core causes the mean temperature in the core region to vary, but only by a factor of $\sim 50\%$, growing with decreasing diffusion. The profiles vary little in the SOL, except for a shoulder-like formation in the near SOL, which is present only for diffusion coefficients < 0.1 .

density gradient builds up in the core over a quiescent period, because the flow shear prevents convective radial transport, before a violent relaxation occurs, expelling filament-like structures out into the SOL. This process happens periodically and figure 56 shows the evolution of a single such “burst”. During the quiescent period between bursts, the particle transport in the SOL is entirely diffusive. When the burst occurs, an eruption of filaments across the separatrix relaxes part of the density gradient that has built up through convective particle transport.

The cyclical nature of this process can be seen in figure 57, which shows a quasi-periodic oscillation in both the radial particle transport (represented by the mean radial component of the kinetic energy $\langle K_x \rangle$), and the strength of the binormal flow (represented the mean binormal component of the kinetic energy $\langle K_z \rangle$).

This behaviour is challenging to deterministically reproduce (as is sometimes the case with nonlinear turbulence simulations[229]). Whilst it has been observed only below a certain threshold of normalised viscosity coefficient (holding the diffusion coefficient constant), simply running a simulation with the same values of the dissipation parameters is not always sufficient to generate the bursting behaviour. Instead, it seems that the bursting state depends on the

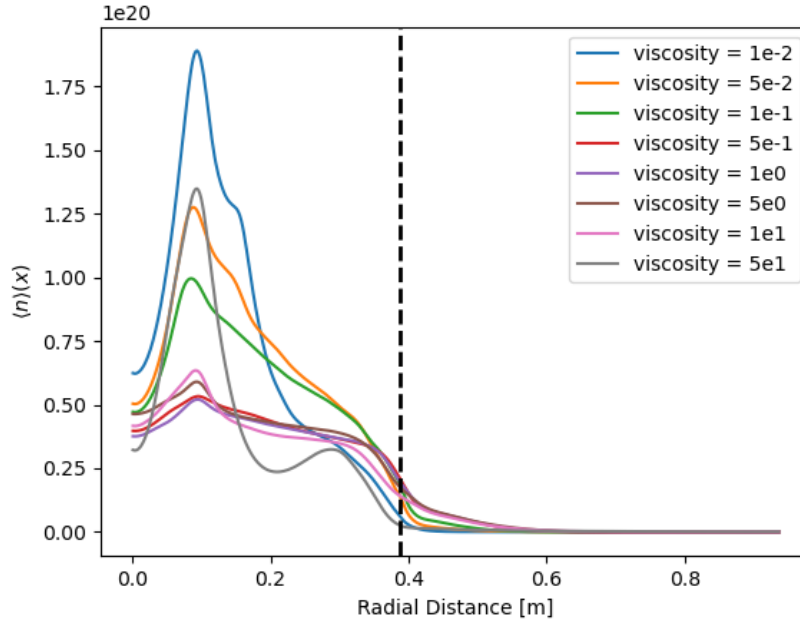


Figure 54: Mean core-SOL density profiles as a function of core viscosity. Values of diffusion $0.1 < D_n < 50$ create very similar core and SOL density profiles, with values outside of that range having much higher mean densities in the core.

previous state of the turbulent system, requiring the correct shear flow structures to have formed before the viscosity is set to the final value. The violent motions are also numerically challenging to resolve.

The phenomenon appears to still be a robust solution of the system - transplanting initial conditions taken from a snapshot of a simulation displaying the bursting causes the behaviour to repeat even if minor alterations are made to the system (for example by changing the loss terms in the SOL, or changing the exact numerical representation of an analytically-equivalent term). Whilst an exact recipe for always creating this bursting behaviour however remains elusive, the formation of strong binormal mean flows (without bursting) is not difficult to reproduce at all: it was replicated in isothermal simulations, simulations using the Bisai model[94], and simulations using the Hermes model².

This sensitivity implies that the mechanism setting the total size of the mean flows is strongly non-linear.

This sensitivity is in contrast to the SOL-only simulations presented in chapter 5, for which the same set of input parameters seem to always create the same final state of turbulence (after a few correlation times have elapsed), regardless of the trajectory taken through parameter

²Performed by the author.

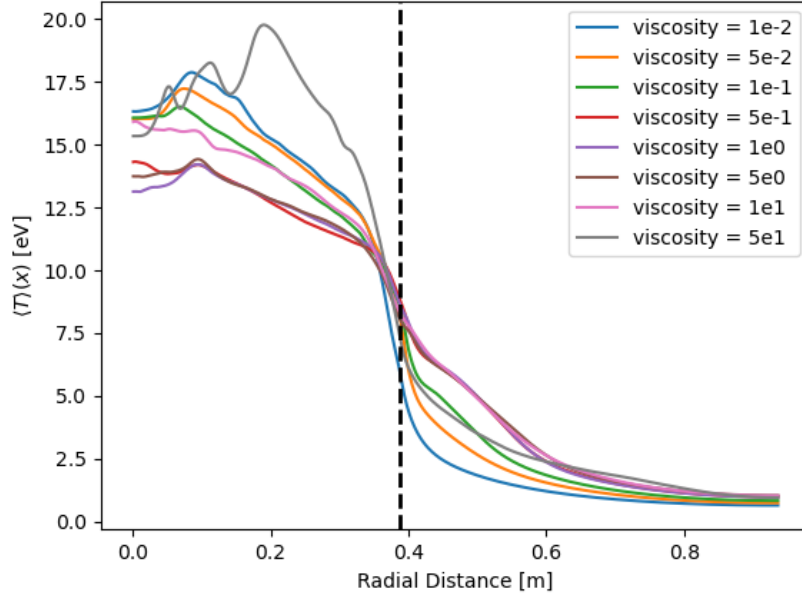


Figure 55: Mean core-SOL temperature profiles as a function of core viscosity. The temperature profiles in the core vary relatively little with viscosity, but do display a trend of increasing mean profile with decreasing viscosity (with the exception of the very high viscosity case $\mu_{\Omega} = 50$.) Step profiles just inside the separatrix connect to a SOL in which the trend is reversed, with steeper more exponential profiles having lower values of viscosity.

space beforehand.

These simulations all have classical dissipation coefficients used in the SOL, and only vary the core values, but qualitatively similar results were obtained for simulations in which the diffusion coefficients were radially-constant.

6.7 Possible Solutions

6.7.1 Stay Above Threshold

It is possible to simply choose to run coupled core-SOL simulations only with values of dimensionless dissipation parameters which lie above the threshold at which the binormal flows form. This can also be done whilst using classical dissipation coefficients in the SOL: choosing neoclassical values in the core region and classical in the SOL is perfectly appropriate (the linear stability implications of this were studied in [157]). This arguably affects the generalizability of the simulations however.

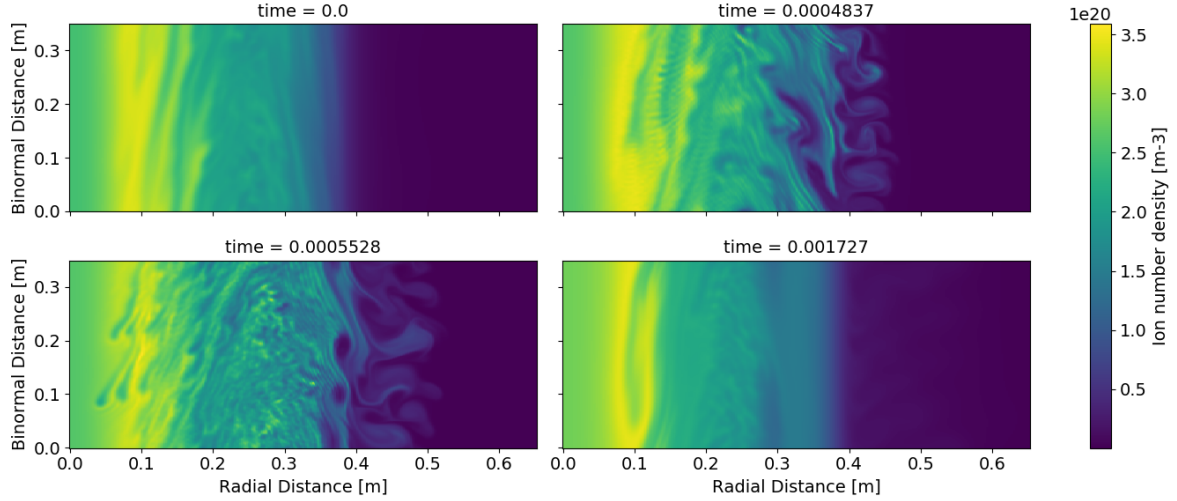


Figure 56: Density snapshots showing the lifecycle of an intermittent burst of transport. The first and last panels (top-left and bottom-right) show the quiescent state in between bursts, during which the particle transport in the SOL is dominated by diffusion. Time is in seconds, and these snapshots are from a simulation with normalised viscosity $\mu_\Omega = 0.05$, normalised perpendicular temperature diffusion $\kappa_\perp = 0.02$, and normalised diffusion $D_n = 0.01$.

6.7.2 Hasegawa-Wakatani Term

Our previous assumption in section 6.3 assumed no parallel current. We now try instead including the parallel terms, but assuming only a small level of fluctuations, which have a small parallel wavenumber, so as not to have to model the entire parallel mode structure. The additional terms we are deriving follow Russell et al[230], but are originally from Hasegawa and Wakatani[231, 232].

To allow the parallel dynamics to re-enter the equations, we take the parallel component of the divergence of electron velocity that appears in 3D density equation (3.107), as well as the parallel component of the divergence of current that appears in the 3D vorticity equation (3.111), which both have the form

$$\nabla_{\parallel} n V_{\parallel e}. \quad (6.4)$$

Having added terms which depend on the parallel electron velocity V , we require a closure to specify V . For this we can use the electron parallel momentum equation (3.110), otherwise known as Ohm's law. Taking the component parallel to the magnetic field, neglecting electron inertia and ion velocity, and including the friction due to collisions with ions at a rate ν_{ei} , we

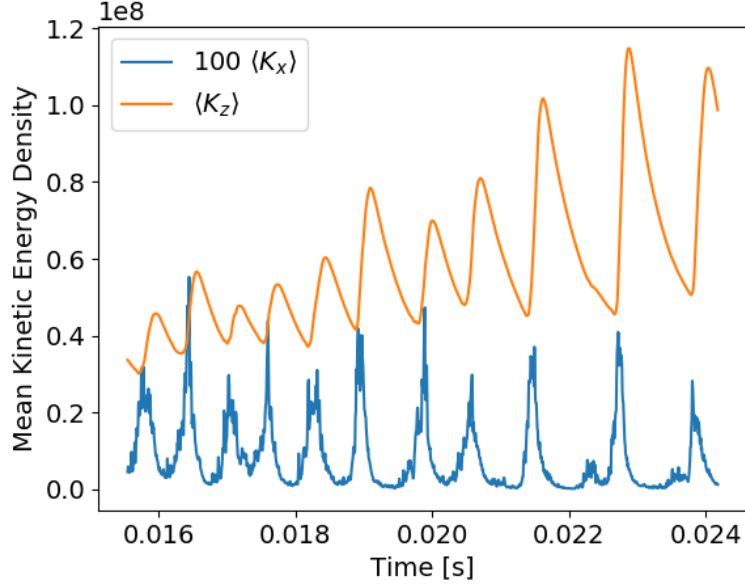


Figure 57: Evolution of the mean kinetic energy in the radial $\langle K_x \rangle$, and binormal $\langle K_z \rangle$ flows. An interplay can be seen whereby the radial kinetic energy only spikes when the binormal mean flows become proportionally weaker. This behaviour is very similar to that displayed in figure 7 in [228], as well as figure 13 in [139]

have

$$0 = -eE_{\parallel} - \frac{1}{n} \nabla_{\parallel} p_e - m_e \nu_{ei} V_{\parallel e}. \quad (6.5)$$

If we assume that the electron temperature is constant in the parallel direction, this becomes

$$m_e \nu_{ei} V_{\parallel e} = e \nabla_{\parallel} \phi - \frac{e T_e}{n} \nabla_{\parallel} n. \quad (6.6)$$

We can now substitute this into the parallel velocity term in (3.107) & (3.111), which becomes

$$\nabla_{\parallel} e n V_{\parallel e} = \nabla_{\parallel} \left[\frac{n e T_e}{m_e \nu_{ei}} \left(\frac{1}{T_e} \nabla_{\parallel} \phi - \frac{1}{n} \nabla_{\parallel} n \right) \right]. \quad (6.7)$$

We now make the reduction to 2D, which comes from assuming that the parallel structure of the variables has only one Fourier mode, so $\nabla_{\parallel}^2 \rightarrow k_{\parallel}^2$. We then set this wavenumber by assuming that the parallel structure has the smallest wavenumber that the system allows, i.e. the parallel connection length in the core $L_{\parallel e}$, so $\nabla_{\parallel}^2 \rightarrow 1/L_{\parallel e}^2$. This assumption is normally justified by appealing to the fact that the dispersion relation of resistive drift-waves has the most unstable mode being the one of longest wavelength[231].

By defining the *dimensionless electron adiabaticity parameter* α_{dw} as

$$\alpha_{\text{dw}} = \frac{2 \rho_s m_i c_s}{L_{\parallel e}^2 \nu_{ei} m_e}, \quad (6.8)$$

the final result is that equations (3.127) and (3.128) correspondingly are replaced with

$$\frac{\partial n}{\partial t} = \frac{1}{B} \{ \phi, n \} + n \mathcal{C}(\phi) + \frac{1}{n} \mathcal{C}(p) + S \mu_n \nabla_{\perp}^2 n - n_{\text{loss}}(x) + \alpha_{\text{dw}}(x) T^{3/2} [\phi - T \ln(n)], \quad (6.9)$$

$$\frac{\partial \Omega}{\partial t} = \frac{1}{B} \{ \phi, \Omega \} + \frac{\mathcal{C}(p)}{n} + \mu_{\Omega} \nabla_{\perp}^2 \Omega - \Omega_{\text{loss}}(x) + \alpha_{\text{dw}}(x) \frac{T^{3/2}}{n} [\phi - T \ln(n)], \quad (6.10)$$

which differ only by the addition of the α_{dw} term. The loss terms have been restricted to $x > x_{\text{sep}}$, and the drift-wave term to $x < x_{\text{sep}}$.

Figure 58 shows the result of running a simulation with this term added. The dissipation parameters were set at $D_n = 0.0027$ and $\mu_{\Omega} = 0.024$, a combination in the same regime which caused the bursting oscillations. The drift-wave parameter was calculated from (6.8), giving a value of $\alpha_{\text{dw}} = 1.6 \times 10^{-5}$. The total binormal flow energy was about 1% of the typical value in the unstable cases shown in section 6.6, and whilst it fluctuates, the average appears to be stable.

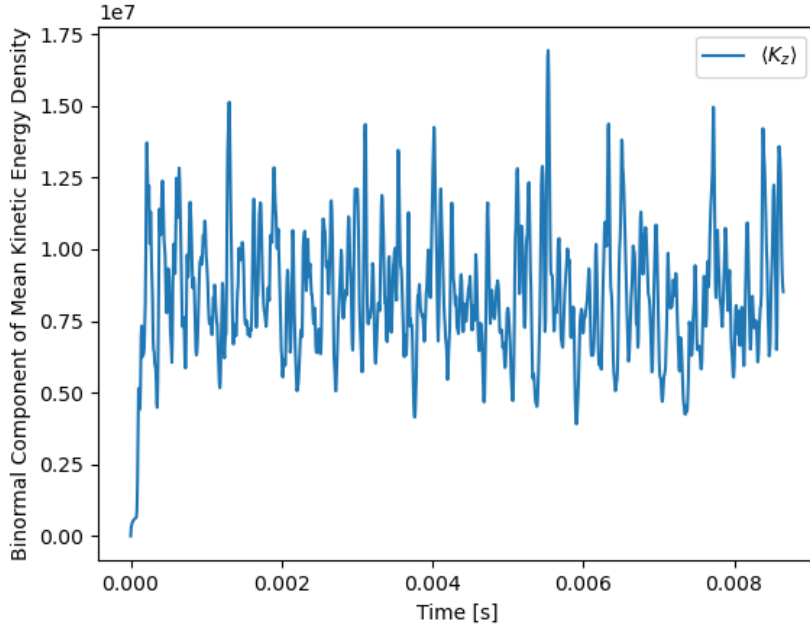


Figure 58: Kinetic energy in the mean binormal mean flow plotted over time, for a case with a Hasegawa-Wakatani type drift-wave term included in the core. The magnitude of the mean flows are only around 1% of their size without the drift-wave term.

However, figure 59 shows that large vortices do appear in the core region, which do not appear in the simulations with high values of dissipation coefficients.

This approach has been used in some 2D edge models, for example [230] and [4].

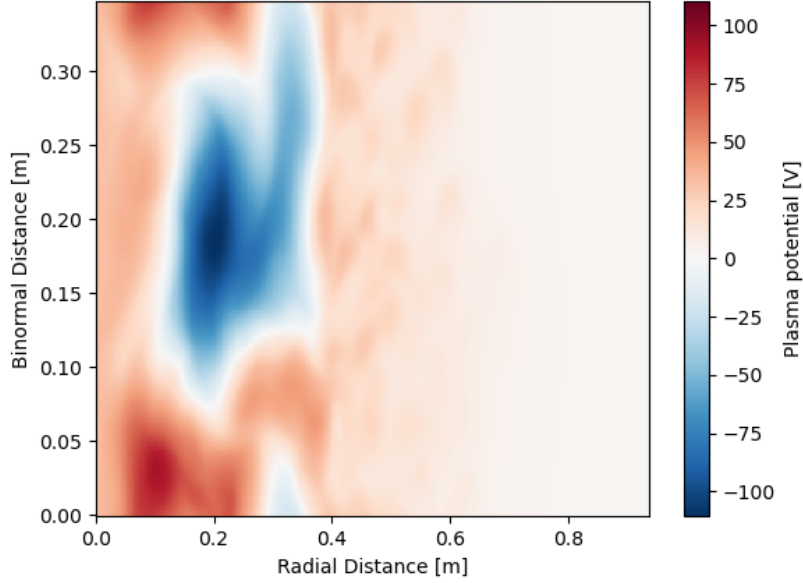


Figure 59: A snapshot of the electric potential for a simulation with the Hasegawa-Wakatani type driftwave closure term in the core included. No overall binormal mean flows have developed, but there are large vortices in the core.

6.8 Similarity to 2D Rayleigh-Bénard System

After performing this investigation, we subsequently learned that a considerable amount of this behaviour can be explained through analogy to similar systems studied in the neutral fluid turbulence literature.

In particular, numerical studies of the classic problem of Rayleigh-Bénard convection in two dimensions have observed the spontaneous generation of self-sustained shear flows, similar instances of “bursting”, as well as a threshold-like dependence on dimensionless parameters. Goluskin[228] sets up a two-dimensional, horizontally periodic system forced by temperature-driven vertical convection represented by the system

$$\nabla \cdot \mathbf{u} = 0 \quad (6.11)$$

$$\frac{\partial \mathbf{u}}{\partial t} + \mathbf{u} \cdot \nabla \mathbf{u} = -\nabla p + Pr \nabla^2 \mathbf{u} + Pr Ra T \hat{\mathbf{z}} \quad (6.12)$$

$$\frac{\partial T}{\partial t} + \mathbf{u} \cdot \nabla T = \nabla^2 T, \quad (6.13)$$

where Pr is the Prandtl number, Ra the Rayleigh number, \mathbf{u} fluid velocity (in a 2D plane), T temperature, and $\hat{\mathbf{z}}$ the direction parallel to the applied temperature gradient and effective gravitational field (which is contained in Ra , see (6.14)).

Despite having a completely different microscopic derivation, this system is similar to our 2D drift-reduced equations in the core. The connection is made by identifying the temperature T in the Goluskin equations with the density n in the STORM2D equations, taking the curl of (6.12) so it can be expressed in terms of vorticity like (3.128), then setting $T_e = 0$ to eliminate the STORM electron temperature equation. The system (6.11) - (6.13) is therefore very close to the 2D isothermal SOL model used in the earliest work with STORM[135] (and many other 2D SOL codes preceding it), though clearly with no SOL parallel loss terms. There are still some differences in the equations: in particular the 2D STORM density equation has curvature drive terms which the Goluskin temperature equation does not.

A larger difference is that Goluskin's system is gradient-driven, instead of source-drive, in the sense that the vertical boundaries are pinned to different temperatures. Their choice of vertical temperature difference Δ is also used to normalise the temperature, which means it enters in the strength of the drive term through

$$Ra = \frac{g\alpha d^3 \Delta}{\kappa\nu}, \quad (6.14)$$

where g is the gravitational acceleration along $-\hat{\mathbf{z}}$ (equivalent to x in the STORM model), ν the viscosity, κ the thermal diffusivity (equivalent to the particle diffusion in the STORM model), and α is the linear coefficient of thermal expansion. The Prandtl number is defined as

$$Pr = \frac{\nu}{\kappa} \quad (6.15)$$

The Goluskin system is equivalent to the “resistive-g” model studied by Garcia[233].

Studied same phenomenon in a very similar thermal convection system in [159], but again it was gradient-driven.

The simulations of section 6.6.3 can be partly explained in terms of these related models. The formation of strong mean binormal flows is clearly not just a numerical artifact, but a result seen across a class of similar systems. The behaviour of Goluskin's Rayleigh Bénard system, as well as the predator-prey cycle described by Garcia[139] both go some way to explaining the periodic bursting behaviour observed in 6.6.3. It also explains the onset of the bursting at low viscosity through a dependence on the Prandtl number (6.15).

Clearly some of the behaviour described earlier in this chapter has been observed in similar systems before - what we have added here is a demonstration that the problem persists in more complex SOL models (with a temperature equation), the problems it presents for would-be SOL modellers, and advantages and disadvantages of various solutions.

6.9 Conclusions

In this chapter we have experimented with adding a core region to SOL-only 2D simulations. We have found that this causes considerable complications, exhibiting strongly non-linear behaviour and sometimes compromising the validity of a simulation as a realistic comparison to experiment.

In particular strong binormal mean flows are consistently observed in the core region, whose presence is resistant to changes in boundary conditions and SOL physics. These flows can display an interesting oscillatory behaviour, whose characteristics we relate to previous work using simpler Rayleigh-Bénard models.

We also examine the effect of altering perpendicular diffusion coefficients, and find that both viscosity and density diffusion matter a lot for SOL profiles, even when only changed in the core.

Lastly, we have shown that some of these issues can be overcome by using a Hasegawa-Wakatani type parallel closure in the core region.

Chapter 7

Conclusions and Future Work

7.1 Conclusions

Role of fusion within a future energy mix

Nuclear fusion research promises one option for long-term supply, once a number of outstanding research challenges are solved. However, the size of the role that fusion will actually play in future energy grids is affected by the competition it will face, and how energy infrastructure changes in the time before fusion's commercialisation. We have reviewed the common picture of the advantages and disadvantages of fusion as an energy generation source relative to other technologies. A significant finding from this review is that recent research suggests that realistic fusion reactor designs will produce significant quantities of intermediate-level nuclear waste, weakening one of the advantages over conventional and advanced fission technologies. Our analysis also focuses partly on the implications of a rise of alternative energy sources before fusion becomes available [1]. In contrast to some assumptions previously made in the community, we conclude that a relatively specific set of circumstances need to occur in wider society and the energy mix in order for fusion to be deployed widely.

Scrape-off layer turbulence modelling with STORM

For any fusion reactor concept, management of the heat of exhausted charged particles represents a critical challenge. Good divertor performance is required with a burning plasma, reliability is necessary for competitive electricity production, and the better managed the heat loads the smaller a reactor can be constructed.

The heat fluxes incident on the plasma-facing components are largely determined by transport in the Scrape-Off Layer (SOL). Radial turbulent transport competes with transport parallel

to the magnetic field in order to set the width over which exhausted heat is deposited.

A large fraction of cross-field transport in the SOL can be understood as being due to the motions of field-aligned filamentary structures, which are spontaneously generated by the edge turbulence. Pressure gradients within these filaments create diamagnetic currents, which are closed partially by polarization currents. The latter create electric fields across the filaments in the drift-plane, which drive the filaments radially outwards through $\mathbf{E} \times \mathbf{B}$ drifts.

The work in this thesis builds upon previous single-filament modelling work with STORM, in which lone filaments were artificially seeded before propagating over a fixed background. Instead, saturated SOL turbulence is generated through a radial gradient in the temperature and density profiles, created through localised particle and energy sources. This approach allows for spontaneous filament generation, inter-filament interactions, and no separation between the filamentary fluctuations and the averaged profiles.

To enable this work the STORM2D code used for previous single-filament modelling has been extended, including to model non-isothermal electrons. A new analysis package xBOUT has also been written, which facilitates rapid and scalable analysis of all data generated with BOUT++, including STORM data.

Comparisons between 2D and 3D models

There exists a body of work using simplified 2D drift-plane models to treat the problem of SOL turbulent transport. We described a simulation setup which aims to produce the closest possible comparison between the 2D STORM model and the 3D STORM model, run for plasma parameters representative of the MAST SOL in L-mode.

We found that an interplay of issues caused by two reasonable-seeming assumptions in the model setup were the main reason for differences between the 2D and analogous 3D models. In very high collisionality conditions, the assumptions used to close 2D models are not valid, because high enough collisionality suppresses thermal conduction so that convection becomes important. Despite these differences, the 2D model successfully replicates the mean density profile of the 3D models with matched sources and no parameter tuning. The 2D model also reproduces the fluctuation statistics of the 3D model fairly well, but the agreement is considerably worse for the mean temperature profile. We also found that the simplistic source setup used in the parallel direction for the 3D simulations causes supersonic flows beyond the X-point, which make the thermal convection compete with conduction at lower collisionality than would otherwise be the case.

This work helps provide a basis for extrapolating the body of work using 2D models into

three dimensional studies.

Coupled core and SOL models

After motivating the coupling of a core region to the SOL models, we adjust our model by adding a core region inside the SOL region.

We have found that this causes considerable complications, exhibiting strongly non-linear behaviour and sometimes compromising the validity of a simulation as a realistic comparison to experiment. In particular strong binormal mean flows are consistently observed in the core region, whose presence is resistant to changes in boundary conditions and SOL physics. These flows can display an interesting oscillatory behaviour, whose characteristics we relate to previous work using simpler Rayleigh-Bénard models.

We also examine the effect of altering perpendicular diffusion coefficients, and find that both viscosity and density diffusion matter a lot for SOL profiles, even when only changed in the core. Lastly, we have shown that some of these issues can be overcome by using a Hasegawa-Wakatani type parallel closure in the core region.

7.2 Future Work

Our analysis of the potential future role for fusion within the energy grid suggests a few avenues for future work, in particular to understand the economic and mechanical suitability of various reactor designs for fast load-following, the lifecycle Energy Return On Invested of a fusion plant, scalability constraints affecting specific raw materials, and the plausibility or desirability of recycling reactor structural materials.

The simulations presented in this thesis assume several simplifications. Whilst a finite electron temperature is modelled, finite ion temperature is neglected. The Boussinesq approximation is employed, despite not being rigorously justified in the SOL. Neutral physics are neglected, as are electromagnetic corrections. The simulations deliberately assume simplified geometries, which include neglecting magnetic shear. Many of these simplifications can be relaxed, at the cost of increased complexity and computational expense. Relaxing these assumptions therefore represents opportunities for future work, building on the basis presented here.

The 2D vs 3D model comparison suggests further work, in particular running with a lower collisionality. We also suggest that future studies always include particle sources in the divertor leg, in order to avoid the highly supersonic flow we observed. Having started with simple 3D models that are the closest possible analogues of the 2D models, a natural direction

for future investigations would be moving the 3D models step by step towards more realistic representations of tokamak divertors.

Appendix A

Scan in Grid Resolution

To test the impact of the choice of grid resolution on the 3D simulations used for results presented in sections 5, additional 3D simulations with different perpendicular grid resolutions were run.

The baseline simulation used for the main results had $240 \times 32 \times 256$ grid points along (x, y, z) , which was supplemented by a lower resolution simulation with $120 \times 32 \times 128$ grid points, and a higher resolution one with $480 \times 32 \times 512$ grid points.

Figure 60 shows that the change in resolution has negligible effect on the average density profile (a similar lack of variation is seen in all other averaged variables).

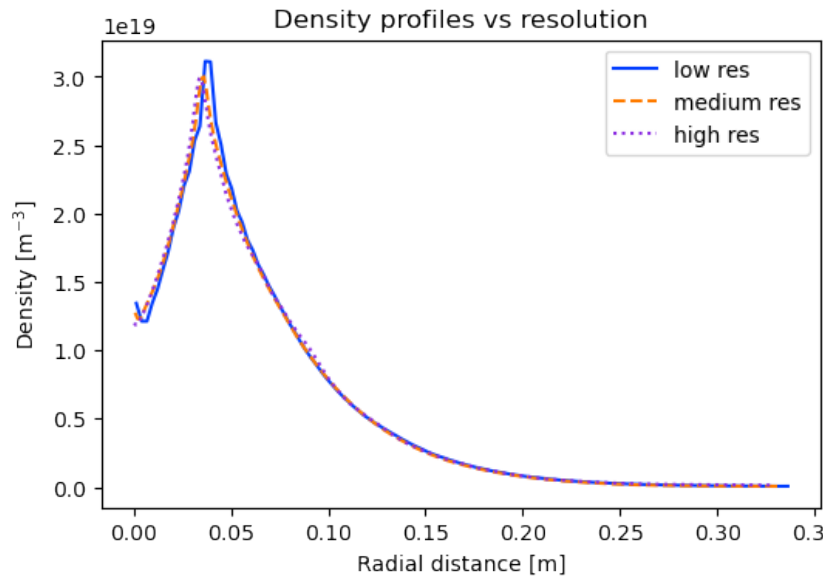


Figure 60: Averaged profiles of density for 3D simulations with three different perpendicular resolutions, showing negligible changes.

There is some difference in the power spectra of the density fluctuations: the lower resolution

simulations show a small “arching” of the power spectrum at smaller spatial scales, but the difference between the medium resolution simulation used and the higher resolution one is small.

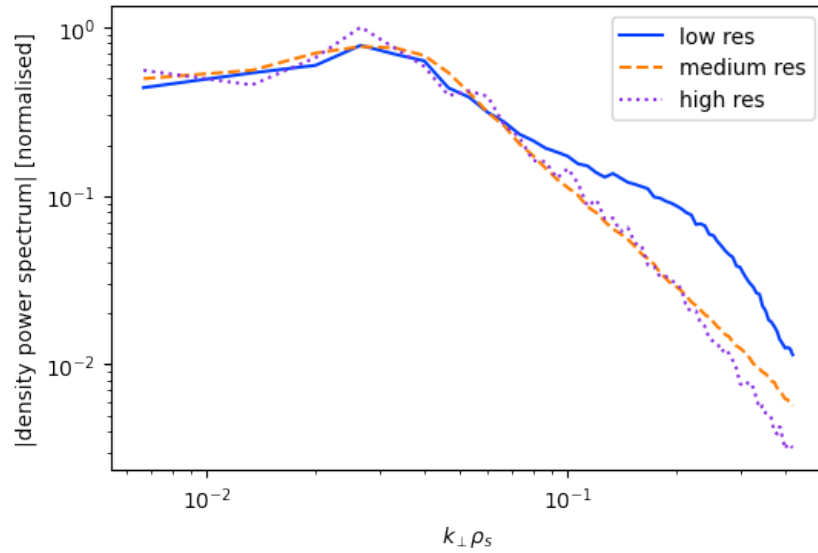


Figure 61: Power spectra of density fluctuations compared across three 3D simulations with different perpendicular resolutions. There is some difference for the lower resolutions, but this reduces to only a small difference when comparing the medium resolution case to the high resolution one.

References

- [1] T E G Nicholas et al. “Re-examining the role of nuclear fusion in a renewables-based energy mix”. In: *Energy Policy* 149.June 2020 (2021), p. 112043. ISSN: 0301-4215. DOI: 10.1016/j.enpol.2020.112043. URL: <https://doi.org/10.1016/j.enpol.2020.112043>.
- [2] T. E. G. Nicholas et al. “Comparing Two- and Three-Dimensional Models of Scrape-Off-Layer Turbulent Transport”. In: (2021), pp. 1–14. arXiv: 2103.09727. URL: <http://arxiv.org/abs/2103.09727>.
- [3] G. Decristoforo et al. “Blob interactions in 2D scrape-off layer simulations”. In: *Physics of Plasmas* 122301.27 (2020). DOI: 10.1063/5.0021314. arXiv: 2007.04260. URL: <https://aip.scitation.org/doi/pdf/10.1063/5.0021314>.
- [4] G Decristoforo et al. “Numerical simulations of intermittent fluctuations in 2D scrape-off layer turbulence”. In: *Physics of Plasmas* (2021), pp. 1–23. arXiv: arXiv:2102.04723v1. URL: <https://arxiv.org/abs/2102.04723>.
- [5] N R Walkden et al. “3D simulations of turbulent mixing in a simplified slab-divertor geometry”. In: *Nuclear Materials and Energy* 18.July 2018 (2019), pp. 111–117. ISSN: 2352-1791. DOI: 10.1016/j.nme.2018.12.005. URL: <https://doi.org/10.1016/j.nme.2018.12.005>.
- [6] D Hoare et al. “Dynamics of scrape-off layer filaments in high β plasmas”. In: *Plasma Physics and Controlled Fusion* 61 (2019).
- [7] Iñaki Arto et al. “The energy requirements of a developed world”. In: *Energy for Sustainable Development* 33 (2016), pp. 1–13. ISSN: 23524669. DOI: 10.1016/j.esd.2016.04.001. URL: <http://dx.doi.org/10.1016/j.esd.2016.04.001>.
- [8] Joel Millward-Hopkins et al. “Providing decent living with minimum energy: A global scenario”. In: *Global Environmental Change* 65.August (2020), p. 102168. ISSN: 09593780.

DOI: 10.1016/j.gloenvcha.2020.102168. URL: <https://doi.org/10.1016/j.gloenvcha.2020.102168>.

- [9] V. Masson-Delmotte et al. *Global Warming of 1.5C. An IPCC Special Report on the impacts of global warming of 1.5C above pre-industrial levels and related global greenhouse gas emission pathways, in the context of strengthening the global response to the threat of climate change*, tech. rep. IPCC, 2018.
- [10] Alinka Lépine-Szily and Pierre Descouvemont. “Nuclear astrophysics: Nucleosynthesis in the Universe”. In: *International Journal of Astrobiology* 11.4 (2012), pp. 243–250. ISSN: 14735504. DOI: 10.1017/S1473550412000158.
- [11] Alak Ray. “Massive stars as thermonuclear reactors and their explosions following core collapse”. In: *Principles and Perspectives in Cosmochemistry*. Ed. by Aruna Goswami and B Eswar Reddy. Berlin, Heidelberg: Springer Berlin Heidelberg, 2010, pp. 209–275. ISBN: 978-3-642-10352-0.
- [12] Kikuchi M and Lackner K. *Fusion Physics*. 2012, p. 22. ISBN: 9789201304100.
- [13] Todd Harrison Rider. “Fundamental Limitations on Plasma Fusion Systems Not in Thermodynamic Equilibrium”. PhD thesis. MIT, 1995.
- [14] S. V. Putvinski, D. D. Ryutov, and P. N. Yushmanov. “Fusion reactivity of the pB11 plasma revisited”. In: *Nuclear Fusion* 59.7 (2019), ab1a60. ISSN: 17414326. DOI: 10.1088/1741-4326/ab1a60. URL: <https://doi.org/10.1088/1741-4326/ab1a60>.
- [15] Marco Raugei and Enrica Leccisi. “A comprehensive assessment of the energy performance of the full range of electricity generation technologies deployed in the United Kingdom”. In: *Energy Policy* 90 (2016), pp. 46–59. ISSN: 0301-4215. DOI: 10.1016/j.enpol.2015.12.011. URL: <http://dx.doi.org/10.1016/j.enpol.2015.12.011>.
- [16] Scott W. White and Gerald L. Kulcinski. “Birth to death analysis of the energy payback ratio and CO2 gas emission rates from coal, fission, wind, and DT-fusion electrical power plants”. In: *Fusion Engineering and Design* 48.3 (2000), pp. 473–481. ISSN: 09203796. DOI: 10.1016/S0920-3796(00)00158-7.
- [17] Jesse D Jenkins, Max Luke, and Samuel Thornstrom. “Getting to Zero Carbon Emissions in the Electric Power Sector”. In: *Joule* 2.12 (2018), pp. 2498–2510. ISSN: 2542-4351. DOI: 10.1016/j.joule.2018.11.013. URL: <https://doi.org/10.1016/j.joule.2018.11.013>.

- [18] Nestor A Sepulveda et al. “The Role of Firm Low-Carbon Electricity Resources in Deep Decarbonization of Power Generation”. In: *Joule* 2.11 (2018), pp. 2403–2420. ISSN: 2542-4351. DOI: 10.1016/j.joule.2018.08.006. URL: <https://doi.org/10.1016/j.joule.2018.08.006>.
- [19] Michael Child et al. “Flexible electricity generation , grid exchange and storage for the transition to a 100 % renewable energy system in Europe”. In: *Renewable Energy* 139 (2019), pp. 80–101. ISSN: 0960-1481. DOI: 10.1016/j.renene.2019.02.077. URL: <https://doi.org/10.1016/j.renene.2019.02.077>.
- [20] William Zappa et al. “Is a 100 % renewable European power system feasible by 2050 ?” In: *Applied Energy* 233-234.July 2018 (2019), pp. 1027–1050. ISSN: 0306-2619. DOI: 10.1016/j.apenergy.2018.08.109. URL: <https://doi.org/10.1016/j.apenergy.2018.08.109>.
- [21] D Fasel and M Q Tran. “Availability of lithium in the context of future D – T fusion reactors”. In: *Fusion Engineering and Design* 79 (2005), pp. 1163–1168. DOI: 10.1016/j.fusengdes.2005.06.345.
- [22] Brian Jaksula. *Mineral Commodity Summaries: Lithium*. Tech. rep. U.S. Geological Survey, 2020. URL: <https://pubs.usgs.gov/periodicals/mcs2020/mcs2020-lithium.pdf>.
- [23] *Uranium 2003: Resources, Production and Demand*. Tech. rep. OECD Nuclear Energy Agency, 2004. URL: <http://www.oecd-nea.org/ndd/pubs/2004/5291-uranium-2003.pdf>.
- [24] Ugo Bardi, Dipartimento Chimica, and Università Firenze. “Extracting Minerals from Seawater: An Energy Analysis”. In: *Sustainability* 2 (2010), pp. 980–992. DOI: 10.3390/su2040980.
- [25] Robert W Conn et al. *Report of the DOE panel on low activation materials for fusion applications*. Tech. rep. DoE Office of Fusion Energy, 1983. DOI: 10.2172/7092294.
- [26] *Radioactive Wastes in the UK : UK Radioactive Waste Inventory Report*. Tech. rep. Nuclear Decommissioning Authority, 2017. URL: <https://ukinventory.nda.gov.uk/wp-content/uploads/sites/18/2014/01/2016UKRWMI-UK-Radioactive-waste-inventory-report.pdf>.

- [27] M J Gorley. “Critical Assessment 12 : Prospects for reduced activation steel for fusion plant”. In: *Materials Science and Technology* 31.8 (2015), pp. 975–980. DOI: 10.1179/1743284714Y.0000000732.
- [28] Ermile Gaganidze et al. “Development of EUROFER97 database and material property handbook”. In: *Fusion Engineering and Design* 135.July (2018), pp. 9–14. ISSN: 0920-3796. DOI: 10.1016/j.fusengdes.2018.06.027. URL: <https://doi.org/10.1016/j.fusengdes.2018.06.027>.
- [29] G Federici et al. “European DEMO design strategy and consequences for materials”. In: *Nuclear Fusion* 57.092002 (2017).
- [30] Robert W Conn et al. “Lower Activation Materials and Magnetic Fusion Reactors”. In: *Nuclear Technology - Fusion* 5.3 (1984), pp. 291–310. DOI: 10.13182/FST84-A23106. URL: <https://doi.org/10.13182/FST84-A23106>.
- [31] M R Gilbert et al. “Waste implications from minor impurities in European DEMO materials”. In: *Nuclear Fusion* 59.076015 (2019).
- [32] G W Bailey, M R Gilbert, and O Vilkhivskaya. “Waste Classification Assessment of Nuclear Steels for Fusion Power Applications”. In: *PHYSOR 2020: Transition to a Scalable Nuclear Future* (2020).
- [33] G.W. Bailey, O.V. Vilkhivskaya, and M.R. Gilbert. “Waste expectations of fusion steels under current waste repository criteria”. In: *Nuclear Fusion* 61.3 (2021), p. 036010. ISSN: 0029-5515. DOI: 10.1088/1741-4326/abc933.
- [34] Robert J Goldston and Alexander Glaser. *Safeguard Requirements for Fusion Power Plants*. Tech. rep. 2012.
- [35] J Reid et al. “Comparison of waste due to irradiated steels in the ESFR and DEMO”. In: *PHYSOR 2020: Transition to a Scalable Nuclear Future* (2020).
- [36] Youji Someya et al. “Management Strategy for Radioactive Waste in the Fusion DEMO Reactor”. In: *Fusion Science and Technology* 68.2 (2015), pp. 423–427. DOI: 10.13182/FST15-101.
- [37] R. A. Mulder, Y. G. Melese, and N. J. Lopes Cardozo. “Plant efficiency: a sensitivity analysis of the capacity factor for fusion power plants with high recirculated power”. In: *Nuclear Fusion* (2021). URL: <https://iopscience.iop.org/article/10.1088/1741-4326/abe68b/pdf>.

- [38] G. R. Tynan and A. Abdulla. “How might controlled fusion fit into the emerging low-carbon energy system of the mid-twenty-first century?” In: *Philosophical Transactions of the Royal Society A: Mathematical, Physical and Engineering Sciences* 378.2184 (2020), p. 20200009. ISSN: 1364-503X. DOI: 10.1098/rsta.2020.0009.
- [39] Jeffrey Freidberg. *Research Needs for Fusion-Fission Hybrid Systems: Report of the Research Needs Workshop (ReNeW) Gaithersburg, Maryland Sept 30 – Oct 2, 2009*. Tech. rep. US Department of Energy, 2009.
- [40] Michael Southon and Susan Krumdieck. “Energy Return on Investment (Eroi) for Distributed Power Generation From Low-Temperature Heat Sources Using the Organic Rankine Cycle”. In: *35th New Zealand Geothermal Workshop: 2013 Proceedings*. November. Rotorua, 2013. URL: https://www.geothermal-energy.org/pdf/IGAsstandard/NZGW/2013/Southon_Final.pdf.
- [41] R. Mitalas and K. R. Sills. “On the Photon Diffusion Time Scale for the Sun”. In: *The Astrophysical Journal* 401 (1992), pp. 759–760.
- [42] Francis F Chen. *Introduction to plasma physics and controlled fusion*. Second. Vol. 53. Springer, 1984, p. 160. ISBN: 9788578110796. DOI: 10.1017/CB09781107415324.004. arXiv: arXiv:1011.1669v3.
- [43] V. D. Shafranov. “Plasma Equilibrium in a Magnetic Field”. In: *Reviews of Plasma Physics* 2 (1966), pp. 103–151.
- [44] Josefine Henriette and Elise Proll. “Trapped-particle instabilities in quasi-isodynamic stellarators”. PhD thesis. Eindhoven University of Technology, 2014.
- [45] Fulvio Militello. *Boundary plasma physics*. Springer Nature, 2021. ISBN: 0124788025. DOI: 10.1016/b978-0-12-478802-2.50020-8.
- [46] N J Lopes Cardozo, A G G Lange, and G J Kramer. “Fusion: Expensive and Taking Forever?” In: *Journal of Fusion Energy* 35.1 (2016), pp. 94–101. ISSN: 1572-9591. DOI: 10.1007/s10894-015-0012-7.
- [47] J P Freidberg, F J Mangiarotti, and J Minervini. “Designing a tokamak fusion reactor — How does plasma physics fit in ?” In: *Physics of Plasmas* 070901.22 (2015). DOI: 10.1063/1.4923266. URL: <http://dx.doi.org/10.1063/1.4923266>.
- [48] T Eich et al. “Scaling of the tokamak near the scrape-off layer H-mode power width and implications for ITER”. In: (2013). DOI: 10.1088/0029-5515/53/9/093031.

- [49] B. N. Sorbom et al. “ARC: A compact, high-field, fusion nuclear science facility and demonstration power plant with demountable magnets”. In: *Fusion Engineering and Design* 100 (2015), pp. 378–405. ISSN: 09203796. DOI: 10.1016/j.fusengdes.2015.07.008. arXiv: 1409.3540.
- [50] Francesco Romanelli et al. *EU-EFDA report: Fusion Electricity - A roadmap to the realisation of fusion energy*. 2012. ISBN: 978-3-00-040720-8. URL: <https://www.euro-fusion.org/wpcms/wp-content/uploads/2013/01/JG12.356-web.pdf>.
- [51] Y Feng. “Plasma Physics and Controlled Fusion Comparison between stellarator and tokamak divertor transport Comparison between stellarator and tokamak divertor”. In: (2011). DOI: 10.1088/0741-3335/53/2/024009.
- [52] Pavel Pereslavytsev et al. “Tritium breeding performance of a DEMO based on the Double Null divertor configuration”. In: *Fusion Engineering and Design* 136. September 2017 (2018), pp. 282–286. ISSN: 0920-3796. DOI: 10.1016/j.fusengdes.2018.02.009. URL: <https://doi.org/10.1016/j.fusengdes.2018.02.009>.
- [53] J. P. Gunn et al. “Surface heat loads on the ITER divertor vertical targets”. In: *Nuclear Fusion* 57.4 (2017). ISSN: 17414326. DOI: 10.1088/1741-4326/aa5e2a.
- [54] A. Loarte and P. J. Harbour. “Effect of the magnetic flux geometry of a poloidal divertor on the profiles and parameters at the target”. In: *Nuclear Fusion* 32.4 (1992), pp. 681–686. ISSN: 00295515. DOI: 10.1088/0029-5515/32/4/I13.
- [55] V. A. Soukhanovskii et al. “Advanced divertor configurations with large flux expansion”. In: *Journal of Nuclear Materials* 438.SUPPL (2013), pp. 6–11. ISSN: 00223115. DOI: 10.1016/j.jnucmat.2013.01.015. URL: <http://dx.doi.org/10.1016/j.jnucmat.2013.01.015>.
- [56] D. Moulton et al. “Using SOLPS to confirm the importance of total flux expansion in Super-X divertors”. In: *Plasma Physics and Controlled Fusion* 59.6 (2017). ISSN: 13616587. DOI: 10.1088/1361-6587/aa6b13.
- [57] E. Havlíčková et al. “Investigation of conventional and Super-X divertor configurations of MAST Upgrade using scrape-off layer plasma simulation”. In: *Plasma Physics and Controlled Fusion* 56.7 (2014). ISSN: 13616587. DOI: 10.1088/0741-3335/56/7/075008.

- [58] E Havlíčková et al. “SOLPS analysis of the MAST-U divertor with the effect of heating power and pumping on the access to detachment in the Super-x configuration”. In: *Plasma Physics and Controlled Fusion* 57.11 (2015), p. 115001. ISSN: 0741-3335. DOI: 10.1088/0741-3335/57/11/115001. URL: <http://iopscience.iop.org/0741-3335/57/11/115001><http://stacks.iop.org/0741-3335/57/i=11/a=115001?key=crossref.1189ca7b2936d4104038cb5efefc0dfb>.
- [59] C. Theiler et al. “Results from recent detachment experiments in alternative divertor configurations on TCV”. In: *Nuclear Fusion* 57.7 (2017). ISSN: 17414326. DOI: 10.1088/1741-4326/aa5fb7.
- [60] Jan Mlynář et al. *Focus On : JET*. Tech. rep. EDFA JET, 2007. URL: https://www.euro-fusion.org/wpcms/wp-content/uploads/2012/01/Focus_on.pdf.
- [61] S. I. Krasheninnikov and A. S. Kukushkin. “Physics of ultimate detachment of a tokamak divertor plasma”. In: *Journal of Plasma Physics* 83.5 (2017). ISSN: 14697807. DOI: 10.1017/S0022377817000654.
- [62] J. W. Connor et al. “Comparison of theoretical models for scrape-off layer widths with data from COMPASS-D, JET and Alcator C-Mod”. In: *Nuclear Fusion* 39.2 (1999), pp. 169–188. ISSN: 00295515. DOI: 10.1088/0029-5515/39/2/304.
- [63] D Bohm. *The characteristics of electrical discharges in magnetic fields*. Ed. by A Guthrie and R K Wakerling. New York: McGraw-Hill, 1949.
- [64] K. McCormick. “No Title”. In: *Controlled Fusion and Plasma Physics (Proceedings of 20th European Conference in Lisbon)*. Geneva: European Physical Society, 1993.
- [65] M.V. Umansky et al. “Modeling of particle and energy transport in the edge plasma of Alcator C-Mod”. In: *Physics of Plasmas* 6.7 (1999). ISSN: 1070664X. DOI: 10.1063/1.873051. URL: <http://dx.doi.org/10.1063/1.873051>.
- [66] B. LaBombard et al. “Cross-field plasma transport and main-chamber recycling in diverted plasmas on Alcator C-Mod”. In: *Nuclear Fusion* 40.12 (2000), pp. 2041–2060. ISSN: 00295515. DOI: 10.1088/0029-5515/40/12/308.
- [67] B Lipschultz et al. “Plasma Physics and Controlled Fusion Investigation of the origin of neutrals in the main chamber of Alcator C-Mod Investigation of the origin of neutrals in the main chamber of Alcator C-Mod”. In: *Plasma Physics and Controlled Fusion* 44 (2002), pp. 733–748.

- [68] P C Stangeby. *The Plasma Boundary of Magnetic Fusion Devices*. Vol. 43. 2. 2000, pp. 223–224. ISBN: 0750305592. DOI: 10.1088/0741-3335/43/2/702.
- [69] B. Lipschultz, D. Whyte, and B. LaBombard. “Comparison of particle transport in the scrape-off layer plasmas of Alcator C-Mod and DIII-D”. In: *Plasma Physics and Controlled Fusion* 47.10 (2005), pp. 1559–1578. ISSN: 07413335. DOI: 10.1088/0741-3335/47/10/001.
- [70] O E Garcia et al. “Turbulent transport in the TCV SOL”. In: *Journal of Nuclear Materials* 363-365.1-3 (2007), pp. 575–580. ISSN: 00223115. DOI: 10.1016/j.jnucmat.2006.12.063. URL: www.elsevier.com/locate/jnucmat.
- [71] V. Naulin. “Turbulent transport and the plasma edge”. In: *Journal of Nuclear Materials* 363-365.1-3 (2007), pp. 24–31. ISSN: 00223115. DOI: 10.1016/j.jnucmat.2006.12.058.
- [72] A. Yu Pigarov et al. “Tokamak edge plasma simulation including anomalous cross-field convective transport”. In: *Physics of Plasmas* 9.4 (2002), p. 1287. ISSN: 1070664X. DOI: 10.1063/1.1459059.
- [73] B. Ph Van Milligen et al. “On the applicability of Fick’s law to diffusion in inhomogeneous systems”. In: *European Journal of Physics* 26.5 (2005), pp. 913–925. ISSN: 01430807. DOI: 10.1088/0143-0807/26/5/023.
- [74] S. Baschetti et al. “A k-epsilon model for plasma anomalous transport in tokamaks: closure via the scaling of the global confinement”. In: *Nuclear Materials and Energy* 19.February (2019), pp. 200–204. ISSN: 23521791. DOI: 10.1016/j.nme.2019.02.032. URL: <https://doi.org/10.1016/j.nme.2019.02.032>.
- [75] Irving Langmuir. “Positive ion currents from the positive column of mercury arcs”. In: *Science* LVIII.1502 (1913), pp. 290–292.
- [76] H. M. Mott-Smith and Irving Langmuir. “The theory of collectors in gaseous discharges”. In: *Physical Review* 28.4 (1926), pp. 727–763. ISSN: 0031899X. DOI: 10.1103/PhysRev.28.727.
- [77] Y. Yang and G. F. Counsell. “Observations with a mid-plane reciprocating probe in MAST”. In: *Journal of Nuclear Materials* 313-316 (2003), pp. 734–737. ISSN: 00223115. DOI: 10.1016/S0022-3115(02)01574-X.

- [78] Guido Van Oost. “Advanced probe edge diagnostics for fusion devices”. In: *Fusion Science and Technology* 53.2T (2008), pp. 387–397. ISSN: 15361055. DOI: 10.13182/fst08-a1724.
- [79] V. I. Demidov, S. V. Ratynskaia, and K. Rypdal. “Electric probes for plasmas: The link between theory and instrument”. In: *Review of Scientific Instruments* 73.10 (2002), p. 3409. ISSN: 00346748. DOI: 10.1063/1.1505099.
- [80] D L Rudakov et al. “Fluctuation-driven transport in the DIII-D boundary”. In: *Plasma Physics and Controlled Fusion* 44 (2002), pp. 717–731. ISSN: 1098-6596. arXiv: arXiv:1011.1669v3.
- [81] S. J. Zweben and R. W. Gould. “Scaling of edge-plasma turbulence in the Caltech tokamak”. In: *Nuclear Fusion* 25.2 (1983), pp. 171–183. ISSN: 17414326. DOI: 10.1088/0029-5515/25/2/005.
- [82] George R. McKee et al. “Plasma Turbulence Imaging via Beam Emission Spectroscopy in the Core of the DIII-D Tokamak”. In: *Plasma and Fusion Research* 2.S1025 (2007). ISSN: 1880-6821. DOI: 10.1585/pfr.2.s1025.
- [83] Audun Theodorsen. “Statistical properties of intermittent fluctuations in the boundary of fusion plasmas”. PhD thesis. UIT, 2018. URL: https://mail-attachment.googleusercontent.com/attachment/u/0/?ui=2&ik=21a249e14b&view=att&th=16387f98ff43413b&attid=0.5&disp=inline&safe=1&zw&sadbat=ANGjdJ_pBMLBoLAY_imjZ0EJnhTG1ws0n8JIwASwivcGG_HoUTr_F4vDUjI02WwEz_4u3Xk6ppGr5tuI1902HfilA2z8
- [84] G Y Antar et al. “Universality of intermittent convective transport in the scrape-off layer of magnetically confined devices”. In: *Physics of Plasmas* 10.2 (2003), pp. 419–428. ISSN: 08631042. DOI: 10.1002/ctpp.200410031. URL: <http://dx.doi.org/10.1063/1.1536166><http://aip.scitation.org/toc/php/10/2>.
- [85] J. Leddy and B. Dudson. “Intrinsic suppression of turbulence in linear plasma devices”. In: *Plasma Physics and Controlled Fusion* 59.125011 (2017). arXiv: 1706.04550.
- [86] B. Ph Van Milligen et al. “Additional evidence for the universality of the probability distribution of turbulent fluctuations and fluxes in the scrape-off layer region of fusion plasmas”. In: *Physics of Plasmas* 12.5 (2005), pp. 1–7. ISSN: 1070664X. DOI: 10.1063/1.1884615.

- [87] G. S. Xu et al. “Blob/hole formation and zonal-flow generation in the edge plasma of the JET tokamak”. In: *Nuclear Fusion* 49.9 (2009). ISSN: 17414326. DOI: 10.1088/0029-5515/49/9/092002.
- [88] G S Xu et al. “Intermittent convective transport carried by propagating electromagnetic filamentary structures in nonuniformly magnetized plasma”. In: *Physics of Plasmas* 17.2 (2010). ISSN: 1070664X. DOI: 10.1063/1.3302535. URL: <http://dx.doi.org/10.1063/1.3302535><http://aip.scitation.org/toc/php/17/2>.
- [89] M. A. Pedrosa et al. “Empirical similarity of frequency spectra of the edge-plasma fluctuations in toroidal magnetic-confinement systems”. In: *Physical Review Letters* 82.18 (1999), pp. 3621–3624. ISSN: 10797114. DOI: 10.1103/PhysRevLett.82.3621.
- [90] B. A. Carreras et al. “Characterization of the frequency ranges of the plasma edge fluctuation spectra”. In: *Physics of Plasmas* 6.12 (1999), pp. 4615–4621. ISSN: 1070664X. DOI: 10.1063/1.873748.
- [91] O. E. Garcia et al. “Intermittent fluctuations in the Alcator C-Mod scrape-off layer for ohmic and high confinement mode plasmas”. In: *Physics of Plasmas* 25.5 (2018). ISSN: 10897674. DOI: 10.1063/1.5018709. arXiv: 1801.00612. URL: <http://dx.doi.org/10.1063/1.5018709>.
- [92] A. Theodorsen, O. E. Garcia, and M. Rypdal. “Statistical properties of a filtered Poisson process with additive random noise: Distributions, correlations and moment estimation”. In: *Physica Scripta* 92.5 (2017). ISSN: 14024896. DOI: 10.1088/1402-4896/aa694c.
- [93] R. Kube et al. “Intermittent electron density and temperature fluctuations and associated fluxes in the Alcator C-Mod scrape-off layer”. In: *Plasma Physics and Controlled Fusion* 60.6 (2018). ISSN: 13616587. DOI: 10.1088/1361-6587/aab726.
- [94] G. Decristoforo. “Numerical simulations and stochastic modelling of intermittent fluctuations in magnetized plasmas”. PhD thesis. UiT - The Arctic University of Norway, 2021.
- [95] S. O. Rice. “Mathematical Analysis of Random Noise”. In: *Bell System Technical Journal* 24.1 (1945), pp. 46–156. ISSN: 15387305. DOI: 10.1002/j.1538-7305.1945.tb00453.x.

- [96] S. J. Zweben et al. “Invited Review Article: Gas puff imaging diagnostics of edge plasma turbulence in magnetic fusion devices”. In: *Review of Scientific Instruments* 88.4 (2017). ISSN: 10897623. DOI: 10.1063/1.4981873. URL: <http://dx.doi.org/10.1063/1.4981873>.
- [97] Thomas Paul Middleton Farley. “Analysis of Plasma Filaments with Fast Visible Imaging in the Mega Ampère Spherical Tokamak”. PhD thesis. University of Liverpool, 2019. DOI: 10.17638/03066785. URL: <https://livrepository.liverpool.ac.uk/3066785/>.
- [98] S. J. Zweben and S. S. Medley. “Visible imaging of edge fluctuations in the TFTR tokamak”. In: *Physics of Fluids B* 1.10 (1989), pp. 2058–2065. ISSN: 08998221. DOI: 10.1063/1.859070.
- [99] S. J. Zweben et al. “High-speed imaging of edge turbulence in NSTX”. In: *Nuclear Fusion* 44.1 (2004), pp. 134–153. ISSN: 00295515. DOI: 10.1088/0029-5515/44/1/016.
- [100] R. J. Maqueda et al. “Gas puff imaging of edge turbulence (invited)”. In: *Review of Scientific Instruments* 74.3 II (2003), pp. 2020–2026. ISSN: 00346748. DOI: 10.1063/1.1535249.
- [101] G Fuchert et al. “Blob properties in L- and H-mode from gas-puff imaging in ASDEX upgrade”. In: *Plasma Physics and Controlled Fusion* 56.12 (2014), p. 125001. ISSN: 0741-3335. DOI: 10.1088/0741-3335/56/12/125001. URL: <http://iopscience.iop.org/0741-3335/56/12/125001>.
- [102] O. Grulke et al. “Experimental investigation of the parallel structure of fluctuations in the scrape-off layer of Alcator C-Mod”. In: *Nuclear Fusion* 54.4 (2014). ISSN: 17414326. DOI: 10.1088/0029-5515/54/4/043012.
- [103] S. J. Zweben et al. “Edge and SOL turbulence and blob variations over a large database in NSTX”. In: *Nuclear Fusion* 55.9 (2015). ISSN: 17414326. DOI: 10.1088/0029-5515/55/9/093035.
- [104] Benjamin D Dudson. “Edge turbulence in the Mega-Amp Spherical Tokamak”. In: (2007), p. 211.
- [105] N. R. Walkden et al. “Fluctuation characteristics of the TCV snowflake divertor measured with high speed visible imaging”. In: *Plasma Physics and Controlled Fusion* 60.11 (2018). ISSN: 13616587. DOI: 10.1088/1361-6587/aae005. arXiv: 1809.03206.

- [106] Jordan Cavalier et al. “Tomographic reconstruction of tokamak edge turbulence from single visible camera data and automatic turbulence structure tracking”. In: *Nuclear Fusion* 59.5 (2019). ISSN: 17414326. DOI: 10.1088/1741-4326/ab0d4c.
- [107] A. Kirk et al. “The spatial structure of type-I ELMs at the mid-plane in ASDEX Upgrade and a comparison with data from MAST”. In: *Plasma Physics and Controlled Fusion* 47.7 (2005), pp. 995–1013. ISSN: 07413335. DOI: 10.1088/0741-3335/47/7/003.
- [108] D. Irajii et al. “Fast visible imaging of turbulent plasma in TORPEX”. In: *Review of Scientific Instruments* 79.10 (2008). ISSN: 00346748. DOI: 10.1063/1.2953677.
- [109] N Ben Ayed et al. “Inter-ELM filaments and turbulent transport in the Mega-Amp Spherical Tokamak”. In: *Plasma Physics and Controlled Fusion* 51.3 (2009), p. 035016. ISSN: 0741-3335. DOI: 10.1088/0741-3335/51/3/035016. URL: <http://stacks.iop.org/0741-3335/51/i=3/a=035016?key=crossref.66f8505e41006d2aa60ebf7e6b9e9d37>.
- [110] D. H J Goodall. “High speed cine film studies of plasma behaviour and plasma surface interactions in tokamaks”. In: *Journal of Nuclear Materials* 111-112.C (1982), pp. 11–22. ISSN: 00223115. DOI: 10.1016/0022-3115(82)90174-X.
- [111] T. Farley et al. “Filament identification in wide-angle high speed imaging of the mega amp spherical tokamak”. In: *Review of Scientific Instruments* 90.9 (2019). ISSN: 10897623. DOI: 10.1063/1.5109470.
- [112] S. J. Zweben. “Search for coherent structure within tokamak plasma turbulence”. In: *Physics of Fluids* 28.3 (1985). URL: [http://w3.pppl.gov/~sim\\$szweben/Papers/ZwebenPF85.pdf](http://w3.pppl.gov/~sim$szweben/Papers/ZwebenPF85.pdf).
- [113] F. Militello et al. “Experimental and numerical characterization of the turbulence in the scrape-off layer of MAST”. In: *Plasma Physics and Controlled Fusion* 55.2 (2013), pp. 25005–12. ISSN: 07413335. DOI: 10.1088/0741-3335/55/2/025005. arXiv: arXiv:1305.5064v1. URL: <http://iopscience.iop.org/0741-3335/55/2/025005>.
- [114] J. A. Boedo et al. “Transport by intermittent convection in the boundary of the DIII-D tokamak”. In: *Physics of Plasmas* 8.11 (2001), pp. 4826–4833. ISSN: 1070664X. DOI: 10.1063/1.1406940.
- [115] D. A. D’Ippolito, J. R. Myra, and S. J. Zweben. “Convective transport by intermittent blob-filaments: Comparison of theory and experiment”. In: *Physics of Plasmas* 18.6 (2011). ISSN: 1070664X. DOI: 10.1063/1.3594609.

- [116] R Kube et al. “Blob sizes and velocities in the Alcator C-Mod scrape-off layer”. In: *Journal of Nuclear Materials* 438.SUPPL (2013), S505–S508. ISSN: 00223115. DOI: 10.1016/j.jnucmat.2013.01.104. URL: http://ac.els-cdn.com/S0022311513001128/1-s2.0-S0022311513001128-main.pdf?_tid=2c13acbc-7daf-11e7-b7af-00000aab0f27&acdnat=1502357877_e99ab2bd854555e4ec2c5a4529a85d00.
- [117] B D Dudson et al. “Experiments and simulation of edge turbulence and filaments in MAST”. In: *Plasma Phys. Control. Fusion* 50.50 (2008), pp. 124012–9. DOI: 10.1088/0741-3335/50/12/124012. URL: <http://iopscience.iop.org/0741-3335/50/12/124012>.
- [118] A Kirk et al. “L-mode filament characteristics on MAST as a function of plasma current measured using visible imaging”. In: *Plasma Phys. Control. Fusion* 58 (2016). URL: <http://iopscience.iop.org/0741-3335/58/8/085008>.
- [119] Y. Marandet et al. “Assessment of the effects of scrape-off layer fluctuations on first wall sputtering with the TOKAM-2D turbulence code”. In: *Plasma Physics and Controlled Fusion* 58.11 (2016). ISSN: 13616587. DOI: 10.1088/0741-3335/58/11/114001.
- [120] D. Carralero et al. “An experimental investigation of the high density transition of the scrape-off layer transport in ASDEX Upgrade”. In: *Nuclear Fusion* 54.12 (2014). ISSN: 17414326. DOI: 10.1088/0029-5515/54/12/123005. arXiv: 1407.3618.
- [121] N. Asakura et al. “SOL plasma profiles under radiative and detached divertor conditions in JT-60U”. In: *Journal of Nuclear Materials* 241-243 (1997), pp. 559–563. ISSN: 00223115. DOI: 10.1016/S0022-3115(96)00564-8.
- [122] B. LaBombard et al. “Particle transport in the scrape-off layer and its relationship to discharge density limit in Alcator C-Mod”. In: *Physics of Plasmas* 8.5 II (2001), pp. 2107–2117. ISSN: 1070664X. DOI: 10.1063/1.1352596.
- [123] B LaBombard et al. “Evidence for electromagnetic fluid drift turbulence controlling the edge plasma state in the Alcator C-Mod tokamak”. In: *Nuclear Fusion* 45.12 (2005), pp. 1658–1675. ISSN: 0029-5515. DOI: 10.1088/0029-5515/45/12/022. URL: <http://stacks.iop.org/0029-5515/45/i=12/a=022?key=crossref.6fa1c5447245f6e19d7a4f5ee9fb75ed>.
- [124] Martin Greenwald. “Density limits in toroidal plasmas”. In: *Plasma Physics and Controlled Fusion* 44.8 (2002). ISSN: 07413335. DOI: 10.1088/0741-3335/44/8/201.

- [125] J. R. Myra and D. A. D'Ippolito. "Scattering of radio frequency waves by blob-filaments". In: *Physics of Plasmas* 17.10 (2010). ISSN: 1070664X. DOI: 10.1063/1.3499670.
- [126] M. W. Brookman et al. "Resolving ECRH deposition broadening due to edge turbulence in DIII-D by heat deposition measurement". In: *arXiv* 53706 (2017), pp. 1–21. arXiv: 1710.03503. URL: <https://www.osti.gov/biblio/1481199>.
- [127] M. B. Thomas et al. "Resolving ECRH deposition broadening due to edge turbulence in DIII-D by 3D full-wave simulations". In: *arXiv* (2017), pp. 1–17. arXiv: 1710.03028. URL: <https://arxiv.org/pdf/1710.03028.pdf>.
- [128] R. Schneider et al. "Plasma edge physics with B2-Eirene". In: *Contributions to Plasma Physics* 46.1-2 (2006), pp. 3–191. ISSN: 08631042. DOI: 10.1002/ctpp.200610001.
- [129] S. Mijin et al. "Kinetic and fluid simulations of parallel electron transport during equilibria and transients in the scrape-off layer". In: *Plasma Physics and Controlled Fusion* 62.9 (2020). ISSN: 13616587. DOI: 10.1088/1361-6587/ab9b39.
- [130] J. T. Omotani and B. D. Dudson. "Non-local approach to kinetic effects on parallel transport in fluid models of the scrape-off layer". In: *Plasma Physics and Controlled Fusion* 55.5 (2013). ISSN: 07413335. DOI: 10.1088/0741-3335/55/5/055009.
- [131] D. M. Fan et al. "Self-consistent coupling of the three-dimensional fluid turbulence code TOKAM3X and the kinetic neutrals code EIRENE". In: *Contributions to Plasma Physics* 58.6-8 (2018), pp. 490–496. ISSN: 15213986. DOI: 10.1002/ctpp.201700216.
- [132] D. M. Fan et al. "Effect of turbulent fluctuations on neutral particles transport with the TOKAM3X-EIRENE turbulence code". In: *Nuclear Materials and Energy* 18. December 2018 (2019), pp. 105–110. ISSN: 23521791. DOI: 10.1016/j.nme.2018.12.011. URL: <https://doi.org/10.1016/j.nme.2018.12.011>.
- [133] Fabio Riva et al. "Three-dimensional plasma edge turbulence simulations of the Mega Ampere Spherical Tokamak and comparison with experimental measurements". In: *Plasma Physics and Controlled Fusion* 61 (2019).
- [134] B D Dudson et al. "The role of particle , energy and momentum losses in 1D simulations of divertor detachment". In: *Plasma Physics and Controlled Fusion* 61.065008 (2019).
- [135] Luke Easy. "Three Dimensional Simulations of Scrape-Off Layer Filaments". PhD thesis. University of York, 2016.

- [136] S I Krasheninnikov. “On scrape off layer plasma transport”. In: *Physics Letters, Section A: General, Atomic and Solid State Physics* 283.5-6 (2001), pp. 368–370. ISSN: 03759601. DOI: 10.1016/S0375-9601(01)00252-3. URL: www.elsevier.nl/locate/pla.
- [137] J T Omotani et al. “The effects of shape and amplitude on the velocity of scrape-off layer filaments”. In: *Plasma Physics and Controlled Fusion* 58.1 (2016), p. 014030. ISSN: 0741-3335. DOI: 10.1088/0741-3335/58/1/014030. arXiv: 1506.02814. URL: <http://stacks.iop.org/0741-3335/58/i=1/a=014030?key=crossref.fba35a3f1be9e2c8a363ad7e9b9fd8b0>.
- [138] S.I. Krasheninnikov, D. A. D’Ippolito, and J. R. Myra. “Recent theoretical progress in understanding coherent structures in edge and SOL turbulence”. In: *Journal of Plasma Physics* 74.05 (2008), pp. 679–717. ISSN: 0022-3778. DOI: 10.1017/S0022377807006940. URL: <http://www.lodestar.com/LRCreports/LRC-07-118.pdf>http://www.journals.cambridge.org/abstract_S0022377807006940.
- [139] O E Garcia, N H Bian, and W Fundamenski. “Radial interchange motions of plasma filaments”. In: *Physics of Plasmas* 13.8 (2006). ISSN: 1070664X. DOI: 10.1063/1.2336422. URL: <http://www.ccfе.ac.uk/assets/Documents/POPVOL13p082309.pdf>.
- [140] C Theiler et al. “Cross-field motion of plasma blobs in an open magnetic field line configuration”. In: *Physical Review Letters* 103.6 (2009). ISSN: 00319007. DOI: 10.1103/PhysRevLett.103.065001. URL: <https://infoscience.epfl.ch/record/143385/files/0806001.pdf>.
- [141] Justin R Angus, Sergei I Krasheninnikov, and Maxim V Umansky. “Effects of parallel electron dynamics on plasma blob transport”. In: *Physics of Plasmas* 19.8 (2012). ISSN: 1070664X. DOI: 10.1063/1.4747619. URL: <http://dx.doi.org/10.1063/1.4747619><http://aip.scitation.org/toc/php/19/8>.
- [142] R Kube and O E Garcia. “Velocity scaling for filament motion in scrape-off layer plasmas”. In: *Physics of Plasmas* 18.10 (2011), pp. 102314–60501. ISSN: 1070664X. DOI: 10.1063/1.3647553. URL: <http://dx.doi.org/10.1063/1.3647553><http://aip.scitation.org/toc/php/18/10>.
- [143] R. Kube, O. E. Garcia, and M. Wiesenberger. “Amplitude and size scaling for interchange motions of plasma filaments”. In: *Physics of Plasmas* 23.12 (2016). DOI: 10.1063/1.4971220. URL: <http://dx.doi.org/10.1063/1.4971220><http://aip.scitation.org/toc/php/23/12>.

- [144] L Easy et al. “Three dimensional simulations of plasma filaments in the scrape off layer: A comparison with models of reduced dimensionality”. In: *Physics of Plasmas* 21.12 (2014). ISSN: 10897674. DOI: 10.1063/1.4904207. arXiv: 1410.2137. URL: <http://dx.doi.org/10.1063/1.4904207>.
- [145] J R Myra et al. “Blob birth and transport in the tokamak edge plasma: Analysis of imaging data”. In: *Physics of Plasmas* 13.9 (2006). ISSN: 1070664X. DOI: 10.1063/1.2355668. URL: <http://dx.doi.org/10.1063/1.2355668><http://aip.scitation.org/toc/php/13/9>.
- [146] Robert Goldston and Paul Rutherford. *Introduction to Plasma Physics*. 1995. ISBN: 0750303255. DOI: 10.1201/9781439822074.
- [147] N. R. Walkden, B. D. Dudson, and G. Fishpool. “Characterization of 3D filament dynamics in a MAST SOL flux tube geometry”. In: *Plasma Physics and Controlled Fusion* 55.10 (2013). ISSN: 07413335. DOI: 10.1088/0741-3335/55/10/105005. arXiv: 1307.5234.
- [148] L Easy et al. “Investigation of the effect of resistivity on scrape off layer filaments using three-dimensional simulations”. In: *Physics of Plasmas* 23.1 (2016). ISSN: 10897674. DOI: 10.1063/1.4940330. arXiv: 1508.04085. URL: <http://dx.doi.org/10.1063/1.4940330>.
- [149] D. Carralero et al. “A study on the density shoulder formation in the SOL of H-mode plasmas”. In: *Nuclear Materials and Energy* 12 (2017), pp. 1189–1193. ISSN: 23521791. DOI: 10.1016/j.nme.2016.11.016.
- [150] N. R. Walkden et al. “Dynamics of 3D isolated thermal filaments”. In: *Plasma Physics and Controlled Fusion* 58 (2016). ISSN: 13616587. DOI: 10.1088/0741-3335/58/11/115010. arXiv: 1606.00582. URL: <http://arxiv.org/abs/1606.00582>.
- [151] D. Schworer et al. “Influence of plasma background on 3D scrape-off layer filaments”. In: *Plasma Physics and Controlled Fusion* 61.025008 (2018).
- [152] S. I. Krasheninnikov and A. I. Smolyakov. “On neutral wind and blob motion in linear devices”. In: *Physics of Plasmas* 10.7 (2003), pp. 3020–3021. ISSN: 1070664X. DOI: 10.1063/1.1579692.
- [153] F. Militello et al. “On the interaction of scrape off layer filaments”. In: *Plasma Physics and Controlled Fusion* 59.12 (2017). ISSN: 13616587. DOI: 10.1088/1361-6587/aa9252.

- [154] P Manz et al. “Origin and turbulence spreading of plasma blobs”. In: *Physics of Plasmas* 22.2 (2015). ISSN: 10897674. DOI: 10.1063/1.4908272. URL: <http://dx.doi.org/10.1063/1.4908272>.
- [155] A. A. Schekochihin, E. G. Highcock, and S. C. Cowley. “Subcritical fluctuations and suppression of turbulence in differentially rotating gyrokinetic plasmas”. In: *Plasma Physics and Controlled Fusion* 54.5 (2012). ISSN: 07413335. DOI: 10.1088/0741-3335/54/5/055011.
- [156] Alessandro Casati. “A quasi-linear gyrokinetic transport model for tokamak plasmas”. PhD thesis. Université de Provence (Aix-Marseille I), France, 2012. arXiv: 1204.3254. URL: <http://arxiv.org/abs/1204.3254>.
- [157] Fryderyk Wilczynski. “Convective motions in the scrape-off layer of magnetically confined plasmas”. PhD thesis. University of Leeds, 2019.
- [158] M. Berning and K. H. Spatschek. “Bifurcations and transport barriers in the resistive-g paradigm”. In: *Physical Review E* 62.1 B (2000), pp. 1162–1174. ISSN: 1063651X. DOI: 10.1103/PhysRevE.62.1162.
- [159] O. E. Garcia et al. “Two-dimensional convection and interchange motions in fluids and magnetized plasmas”. In: *Physica Scripta T* T122 (2006), pp. 104–124. ISSN: 02811847. DOI: 10.1088/0031-8949/2006/T122/014.
- [160] F. Wilczynski et al. “Stability of scrape-off layer plasma: A modified Rayleigh-Bénard problem”. In: *Physics of Plasmas* 26.2 (2019). ISSN: 10897674. DOI: 10.1063/1.5064765. arXiv: 1810.05111.
- [161] W Fundamenski et al. “Dissipative processes in interchange driven scrape-off layer turbulence”. In: *Nuclear Fusion* 47.5 (2007), pp. 417–433. ISSN: 00295515. DOI: 10.1088/0029-5515/47/5/006. URL: <http://iopscience.iop.org/article/10.1088/0029-5515/47/5/006/pdf>.
- [162] F. Wilczynski and D. W. Hughes. “Stability of two-layer miscible convection”. In: *Physical Review Fluids* 4.10 (2019).
- [163] Frank M Richter and Carl E Johnson. “Layered Mantle”. In: *Journal of Geophysical Research* 79.11 (1974), pp. 1197–1197. DOI: 10.1007/978-1-4614-3134-3_100674.
- [164] Fryderyk Wilczynski et al. “Onset of interchange instability in a coupled core – SOL plasma”. In: *Physics of Plasmas* 27.7 (2020), p. 072508. ISSN: 1070-664X. DOI: 10.1063/5.0010114. URL: <http://aip.scitation.org/doi/10.1063/5.0010114>.

- [165] Bruce D Scott. “Three-dimensional computation of drift Alfvén turbulence”. In: *Plasma Physics and Controlled Fusion* 39 (1997), pp. 1635–1668.
- [166] Bruce D Scott. “Tokamak edge turbulence: background theory and computation”. In: *Plasma Phys. Control. Fusion* 49 (2007), pp. 25–41. URL: <http://iopscience.iop.org/0741-3335/49/7/S02>.
- [167] F Nespoli et al. “Blob properties in full-turbulence simulations of the TCV scrape-off layer”. In: (2017).
- [168] C. S. Chang and S. Ku. “Spontaneous rotation sources in a quiescent tokamak edge plasma”. In: *Physics of Plasmas* 15.6 (2008). ISSN: 1070664X. DOI: 10.1063/1.2937116.
- [169] R. M. Churchill et al. “Pedestal and edge electrostatic turbulence characteristics from an XGC1 gyrokinetic simulation”. In: *Plasma Physics and Controlled Fusion* 59.10 (2017). ISSN: 13616587. DOI: 10.1088/1361-6587/aa7c03.
- [170] T T Ribeiro and B Scott. “Tokamak turbulence computations on closed and open magnetic flux surfaces”. In: *Plasma Physics and Controlled Fusion* 47.10 (2005), pp. 1657–1679. ISSN: 0741-3335. DOI: 10.1088/0741-3335/47/10/005. URL: <http://stacks.iop.org/0741-3335/47/i=10/a=005?key=crossref.d1821244b67cd0fa03e5d4b4c6faf0fe>.
- [171] T T Ribeiro and B Scott. “Gyrofluid turbulence studies of the effect of the poloidal position of an axisymmetric Debye sheath”. In: *Plasma Physics and Controlled Fusion* 50.5 (2008), p. 055007. ISSN: 0741-3335. DOI: 10.1088/0741-3335/50/5/055007. URL: <http://stacks.iop.org/0741-3335/50/i=5/a=055007?key=crossref.5d8343d1dc332ae2d0e85bba2c0a6e6f>.
- [172] F D Halpern et al. “The GBS code for tokamak scrape-off layer simulations”. In: *Journal of Computational Physics* 315 (2016), pp. 388–408. ISSN: 0021-9991. DOI: 10.1016/j.jcp.2016.03.040. URL: <http://dx.doi.org/10.1016/j.jcp.2016.03.040>.
- [173] B. N. Rogers and Paolo Ricci. “Low-frequency turbulence in a linear magnetized plasma”. In: *Physical Review Letters* 104.22 (2010), pp. 4–7. ISSN: 00319007. DOI: 10.1103/PhysRevLett.104.225002.
- [174] I. Furno et al. “Experimental observation of the blob-generation mechanism from interchange waves in a plasma”. In: *Physical Review Letters* 100.5 (2008), pp. 8–11. ISSN: 00319007. DOI: 10.1103/PhysRevLett.100.055004.

- [175] F. D. Halpern et al. “Comparison of 3D flux-driven scrape-off layer turbulence simulations with gas-puff imaging of Alcator C-Mod inner-wall limited discharges”. In: *Plasma Physics and Controlled Fusion* 57.5 (2015). ISSN: 13616587. DOI: 10.1088/0741-3335/57/5/054005.
- [176] P Tamain et al. “The TOKAM3X code for edge turbulence fluid simulations of tokamak plasmas in versatile magnetic geometries”. In: *Journal of Computational Physics* 321 (2016), pp. 606–623. ISSN: 0021-9991. DOI: 10.1016/j.jcp.2016.05.038. URL: <http://dx.doi.org/10.1016/j.jcp.2016.05.038>.
- [177] Y Sarazin and Ph Ghendrih. “Intermittent particle transport in two-dimensional edge turbulence”. In: *Physics of Plasmas* 5.12 (1998), pp. 4214–4228. ISSN: 1070664X. DOI: 10.1063/1.873157. URL: <http://aip.scitation.org/toc/php/5/12>.
- [178] Davide Galassi and Paolo Ricci. “Numerical modelling of transport and turbulence in tokamak edge plasma with divertor configuration”. PhD thesis. 2017.
- [179] F Militello et al. “Simulations of edge and scrape off layer turbulence in mega ampere spherical tokamak plasmas”. In: *Plasma Phys. Control. Fusion* 54.54 (2012), pp. 95011–10. DOI: 10.1088/0741-3335/54/9/095011. URL: <http://iopscience.iop.org/0741-3335/54/9/095011>.
- [180] Bruce D Scott. “Low Frequency Fluid Drift Turbulence in Magnetised Plasmas”. PhD thesis. Max-Planck-Institut für Plasmaphysik, 2000.
- [181] F D Halpern et al. “Theory of the scrape-off layer width in inner-wall limited tokamak plasmas”. In: *Nuclear Fusion* 54.043003 (2014). DOI: 10.1088/0029-5515/54/4/043003.
- [182] S. I. Braginskii. “Transport Processes In A Plasma”. In: *Reviews of Plasma Physics* (1965).
- [183] V M Zhdanov. “Transport Processes in Multicomponent Plasma”. In: *Plasma Physics and Controlled Fusion* 44.10 (2002), p. 2283. DOI: 10.1088/0741-3335/44/10/701. URL: <https://doi.org/10.1088/0741-3335/44/10/701>.
- [184] A. Poulsen et al. “Collisional multispecies drift fluid model”. In: *Physics of Plasmas* 27.3 (2020). ISSN: 10897674. DOI: 10.1063/1.5140522.
- [185] R O Dendy. *Plasma Physics: An Introductory Course*. Cambridge University Press. ISBN: 9780521484527.

- [186] Andrei N Simakov and Peter J Catto. “Drift-ordered fluid equations for field-aligned modes in low- β collisional plasma with equilibrium pressure pedestals”. In: *Physics of Plasmas* 10.101 (2003). DOI: 10.1063/1.1623492. URL: <http://dx.doi.org/10.1063/1.1623492><http://aip.scitation.org/toc/php/10/12>.
- [187] R. D. Hazeltine and J. D. Meiss. *Plasma confinement*. Courier Corporation, 2003.
- [188] S Ahmed. “Effects of ion temperature on Scrape-off layer filaments”. PhD thesis. University of Bath, 2020.
- [189] J Madsen et al. “Collisional transport across the magnetic field in drift-fluid models”. In: *Physics of Plasmas* 23.3 (2016). ISSN: 10897674. DOI: 10.1063/1.4943199. arXiv: 1512.07425. URL: <http://dx.doi.org/10.1063/1.4943199><http://aip.scitation.org/toc/php/23/3>.
- [190] Peter C Stangeby and Others. *The plasma boundary of magnetic fusion devices*. Vol. 224. Institute of Physics Publishing Bristol, 2000.
- [191] A. Geraldini, F. I. Parra, and F. Militello. “Gyrokinetic treatment of a grazing angle magnetic presheath”. In: *Plasma Physics and Controlled Fusion* 59.2 (2017). ISSN: 13616587. DOI: 10.1088/1361-6587/59/2/025015.
- [192] J R Myra et al. “Reduced model simulations of the scrape-off-layer heat-flux width and comparison with experiment”. In: *Physics of Plasmas* 18.1 (2011). ISSN: 1070664X. DOI: 10.1063/1.3526676. URL: <https://doi.org/10.1063/1.3526676><http://aip.scitation.org/toc/php/18/1>.
- [193] B D Dudson et al. “BOUT++: A framework for parallel plasma fluid simulations”. In: *Computer Physics Communications* 180.9 (2009), pp. 1467–1480. ISSN: 00104655. DOI: 10.1016/j.cpc.2009.03.008. arXiv: 0810.5757. URL: www.elsevier.com/locate/cpc.
- [194] M V Umansky et al. “Status and verification of edge plasma turbulence code BOUT”. In: *Computer Physics Communications* 180.6 (2009), pp. 887–903. ISSN: 00104655. DOI: 10.1016/j.cpc.2008.12.012. URL: www.elsevier.com/locate/cpc.
- [195] B. D. Dudson et al. “BOUT++: Recent and current developments”. In: *Journal of Plasma Physics* 81.01 (2014). ISSN: 0022-3778. DOI: 10.1017/S0022377814000816. arXiv: 1405.7905. URL: http://www.journals.cambridge.org/abstract_S0022377814000816.

- [196] B. D. Dudson et al. “Verification of BOUT++ by the method of manufactured solutions”. In: *Physics of Plasmas* 23.6 (2016). ISSN: 10897674. DOI: 10.1063/1.4953429. arXiv: 1602.06747. URL: <http://dx.doi.org/10.1063/1.4953429><http://aip.scitation.org/toc/php/23/6>.
- [197] B. D. Dudson. *BOUT++ Documentation*. 2019. URL: bout-dev.readthedocs.io/.
- [198] A Arakawa. “Computational design for long term integration of the equations of motion: Two-dimensional incompressible flow. Part 1”. In: *J. Comput. Phys* 1.1 (1966), pp. 19–143.
- [199] J Leddy, B Dudson, and H Willett. “Simulation of the interaction between plasma turbulence and neutrals in linear devices”. In: *Nuclear Materials and Energy* 12 (2017), pp. 994–998. ISSN: 23521791. DOI: 10.1016/j.nme.2016.09.020. URL: www.elsevier.com/locate/nme.
- [200] Peter Hill, Brendan Shanahan, and Ben Dudson. “Dirichlet boundary conditions for arbitrary-shaped boundaries in stellarator-like magnetic fields for the Flux-Coordinate Independent method”. In: *Computer Physics Communications* 213 (2017), pp. 9–18. ISSN: 0010-4655. DOI: 10.1016/j.cpc.2016.11.004. URL: <http://dx.doi.org/10.1016/j.cpc.2016.11.004>.
- [201] I Romadanov, Y Raitses, and A Smolyakov. “Hall thruster operation with externally driven breathing mode oscillations”. In: (2018).
- [202] Benjamin D Dudson and Jarrod Leddy. “Hermes : global plasma edge fluid turbulence simulations”. In: *Plasma Physics and Controlled Fusion* 59 (2017).
- [203] M.V. Umansky, B.I. Cohen, and J.R. Myra. “Implementation of plasma turbulence model for tokamak scrape- off layer and divertor”. In: *DPP19 Meeting of The American Physical Society*. 2019.
- [204] Andreas Stegmeir et al. “GRILLIX : a 3D turbulence code based on the flux-coordinate independent approach”. In: *Plasma Physics and Controlled Fusion* 60 (2018).
- [205] Jeppe Olsen et al. “Temperature dynamics and velocity scaling laws for interchange driven , warm ion plasma filaments”. In: (2016). DOI: 10.1088/0741-3335/58/4/044011.

- [206] F Militello et al. “Multi-code analysis of scrape-off layer filament dynamics in MAST”. In: *Plasma Physics and Controlled Fusion* 58.10 (2016), p. 105002. ISSN: 0741-3335. DOI: 10.1088/0741-3335/58/10/105002. URL: <https://infoscience.epfl.ch/record/221011/files/Militello2016.pdf><http://stacks.iop.org/0741-3335/58/i=10/a=105002?key=crossref.c1ba900da67b8f4f9726fbdcbce2ea76b>.
- [207] D Schwörer et al. “Influence of plasma background including neutrals on scrape-off layer filaments using 3D simulations”. In: *Nuclear Materials and Energy* 12 (2017), pp. 825–830. ISSN: 23521791. DOI: 10.1016/j.nme.2017.02.016. URL: <https://pinboard.ukaea.uk/wp-content/uploads/papers/1516002530-49970/filament17.pdf>.
- [208] George D Byrne et al. “PVODE, an ODE solver for parallel computers”. In: *International Journal of High-Performance Computing Applications* 13.4 (1999), pp. 354–365. DOI: 10.1177/109434209901300405.
- [209] Llewellyn Hilleth Thomas. “Elliptic problems in linear difference equations over a network”. In: *Watson Sci. Comput. Lab. Rept., Columbia University, New York* 1 (1949).
- [210] J R Angus and S I Krasheninnikov. “Inviscid evolution of large amplitude filaments in a uniform gravity field”. In: *Physics of Plasmas* 21.11 (2014). ISSN: 10897674. DOI: 10.1063/1.4901237. URL: <http://dx.doi.org/10.1063/1.4901237><http://aip.scitation.org/toc/php/21/11>.
- [211] Guido Van Rossum and Fred L. Drake. *Python 3 Reference Manual*. CreateSpace, 2009. ISBN: 1441412697.
- [212] Stephan Hoyer and Joseph J Hamman. “xarray : N-D labeled Arrays and Datasets in Python”. In: *Journal of Open Research Software* (2017), pp. 1–6.
- [213] Travis Oliphant. *NumPy: A guide to NumPy*. USA: Trelgol Publishing. URL: <http://www.numpy.org/>.
- [214] Charles R. Harris et al. “Array programming with NumPy”. In: *Nature* 585.7825 (2020), pp. 357–362. ISSN: 14764687. DOI: 10.1038/s41586-020-2649-2. arXiv: 2006.10256. URL: <http://dx.doi.org/10.1038/s41586-020-2649-2>.
- [215] Dask Development Team. *Dask: Library for dynamic task scheduling*. 2016. URL: <https://dask.org>.

- [216] S. A. Brown et al. “Software for Portable Scientific Data Management”. In: *Computers in Physics* 7.3 (2016), pp. 304–308.
- [217] Matthew Rocklin. “Dask : Parallel Computation with Blocked algorithms and Task Scheduling”. In: *Proceedings of the 14th python in science conference*. 2015, pp. 126–132.
- [218] Eric Jones et al. *SciPy: Open source scientific tools for Python*. URL: <http://www.scipy.org/>.
- [219] Thomas Kluyver et al. “Jupyter Notebooks – a publishing format for reproducible computational workflows”. In: *Positioning and Power in Academic Publishing: Players, Agents and Agendas*. Ed. by F Loizides and B Schmidt. IOS Press. 2016, pp. 87–90.
- [220] J R Myra et al. “Turbulent transport and the scrape-off-layer width”. In: *Journal of Nuclear Materials*. Vol. 415. 2011, S605–S608. ISBN: 0022-3115. DOI: 10.1016/j.jnucmat.2010.10.030. URL: https://nstx.pppl.gov/DragNDrop/Publications_Presentations/Publications/2011Papers/2011_locked/Myra_JNM.pdf.
- [221] Nirmal Bisai et al. “Formation of a density blob and its dynamics in the edge and the scrape-off layer of a tokamak plasma”. In: *Physics of Plasmas* 12.10 (2005), pp. 1–6. ISSN: 1070664X. DOI: 10.1063/1.2083791. URL: <http://dx.doi.org/10.1063/1.1942427><http://aip.scitation.org/toc/php/12/7>.
- [222] F Militello and W Fundamenski. “Multi-machine comparison of drift fluid dimensionless parameters”. In: *Plasma Physics and Controlled Fusion* 53.9 (2011), p. 095002. ISSN: 0741-3335. DOI: 10.1088/0741-3335/53/9/095002. URL: <http://stacks.iop.org/0741-3335/53/i=9/a=095002?key=crossref.d9f3bff51ee8c3a2f11699f8c3423544>.
- [223] Ph Ghendrih et al. “Transition to supersonic flows in the edge plasma”. In: *Plasma Physics and Controlled Fusion* 53.5 (2011). ISSN: 13616587. DOI: 10.1088/0741-3335/53/5/054019.
- [224] Jonas Peter Maria Boschung. *Structure function analysis of turbulent flows*. 2017, p. 269. ISBN: 978-3-8440-5449-1. URL: <http://publications.rwth-aachen.de/record/697733>.
- [225] G. Gogoberidze, S. Perri, and V. Carbone. “The yaglom law in the expanding solar wind”. In: *Astrophysical Journal* 769.2 (2013), pp. 1–14. ISSN: 15384357. DOI: 10.1088/0004-637X/769/2/111. arXiv: 1304.4505.

- [226] Guido Boffetta and Robert E Ecke. “Two-Dimensional Turbulence”. In: *Annu. Rev. Fluid Mech* 44 (2012), pp. 427–51. DOI: 10.1146/annurev-fluid-120710-101240. URL: www.annualreviews.org.
- [227] M Barnes, F I Parra, and A A Schekochihin. “Critically balanced ion temperature gradient turbulence in fusion plasmas”. In: *Physical Review Letters* 107.11 (2011). ISSN: 00319007. DOI: 10.1103/PhysRevLett.107.115003. arXiv: 1104.4514. URL: <https://journals.aps.org/prl/pdf/10.1103/PhysRevLett.107.115003>.
- [228] David Goluskin et al. “Convectively driven shear and decreased heat flux”. In: *Journal of Fluid Mechanics* 759.6 (2014), pp. 360–385. ISSN: 14697645. DOI: 10.1017/jfm.2014.577. arXiv: 1408.4802.
- [229] Olivier Mesnard and Lorena A. Barba. “Reproducible and Replicable Computational Fluid Dynamics: It’s Harder Than You Think”. In: *Computing in Science and Engineering* 19.4 (2017), pp. 44–55. ISSN: 15219615. DOI: 10.1109/MCSE.2017.3151254.
- [230] D A Russell, J R Myra, and D. A. D’Ippolito. “Saturation mechanisms for edge turbulence”. In: *Physics of Plasmas* 16.12 (2009). ISSN: 1070664X. DOI: 10.1063/1.3270051. URL: <https://doi.org/10.1063/1.3270051><http://aip.scitation.org/toc/php/16/12>.
- [231] Akira Hasegawa and Masahiro Wakatani. “Plasma Edge Turbulence”. In: *Physical Review Letters* 50.9 (1983), pp. 682–686. URL: <https://journals.aps.org/prl/pdf/10.1103/PhysRevLett.50.682>.
- [232] Akira Hasegawa and Masahiro Wakatani. “Self-Organisation of Electrostatic Turbulence in a Cylindrical Plasma”. In: *Physical Review Letters* 59.14 (1987), pp. 1581–1584. URL: <https://journals.aps.org/prl/pdf/10.1103/PhysRevLett.59.1581>.
- [233] Odd Erik Garcia et al. “Confinement and bursty transport in a flux-driven convection model with sheared flows Confinement and bursty transport in a flux-driven”. In: *Plasma Physics and Controlled Fusion* May (2003). DOI: 10.1088/0741-3335/45/6/306.

